Aachener Verfahrenstechnik Series
AVT.CVT – Chemical Process Engineering
Volume 60 (2025)

Wibke Victoria Zängler

Electrochemical Hydrogen Compression toward Operation in Hydrogen Distribution Systems

Electrochemical Hydrogen Compression toward Operation in Hydrogen Distribution Systems

Elektrochemische Wasserstoffkompression für die Anwendung im Wasserstoffverteilsystem

Von der Fakultät für Maschinenwesen
der Rheinisch-Westfälischen Technischen Hochschule Aachen
zur Erlangung des akademischen Grades
einer Doktorin der Ingenieurwissenschaften
genehmigte Dissertation
vorgelegt von

Wibke Victoria Zängler

Berichter/in:
Univ.-Prof. Dr.-Ing. Matthias Wessling
Prof. Brian Seger, PhD

Tag der mündlichen Prüfung: 18.11.2025

Diese Dissertation ist auf den Internetseiten der Universitätsbibliothek online verfügbar.

Published Content

Parts of this dissertation have been published. Reproduced with permission from:

Wibke Zängler, Mojtaba Mohseni, Robert Keller, Matthias Wessling.
A tubular hydrogen compressor
International journal of hydrogen energy, 2024
DOI: 10.1016/j.ijhydene.2024.03.355

Wibke Zängler, Nick Semrau, Matthias Wessling, Robert Keller.
Effect of natural gas impurities on electrochemical hydrogen compression and strategies for mitigation
International journal of hydrogen energy, 2025
DOI: 10.1016/j.ijhydene.2025.150980

Artificial Intelligence (AI) Statement

This thesis has been partially rewritten using an artificial intelligence (AI) model to improve readability. All ideas, considerations, and content are original and created by the author. Therefore, AI systems are not concerned with intellectual property. The AI usage rules stipulated by the Faculty of Mechanical Engineering of RWTH Aachen University on July 29, 2025, have been fully satisfied.

Impressum

Titel:	Electrochemical Hydrogen Compression toward Operation in Hydrogen Distribution Systems Elektrochemische Wasserstoffkompression für die Anwendung im Wasserstoffverteilsystem
Autor:	Wibke Victoria Zängler
Reihe:	Aachener Verfahrenstechnik Series AVT.CVT - Chemical Process Engineering Volume: 60 (2025)
Herausgeber:	Aachener Verfahrenstechnik Forckenbeckstraße 51 52074 Aachen Tel.: +49 (0)241 8095470 Fax.: +49 (0)241 8092252 E-Mail: secretary.cvt@avt.rwth-aachen.de http://www.avt.rwth-aachen.de/AVT
Volltext verfügbar:	10.18154/RWTH-2025-10510

Universitätsbibliothek
RWTH Aachen University
Templergraben 61
52062 Aachen
http://www.ub.rwth-aachen.de

Danksagung

Fünf intensive Jahre voller Forschung, Neugier und Wachstum in einem tollen Team gehen mit dem Abschluss meiner Promotion zu Ende. Ich bin dankbar für alle, die mich auf diesem Weg begleitet haben - ohne die Beträge, Ideen und Unterstützung von euch hätte ich diesen Meilenstein nicht erreichen können.

Danke, Prof. Matthias Wessling, für die wissenschaftliche Betreuung meiner Promotion. Deine Begeisterung für Forschung steckt an. Danke für die Umgebung aus Vertrauen, Vision und Freiheit, die mich stark als Wissenschaftlerin geprägt hat. A big thank you to Prof. Brian Seger for hosting my stay at the DTU and being my second examiner.

Allen Kolleg:innen der CVT gilt ein großer Dank - Ihr formt ein inspirierendes Team, in dem es Spaß macht zu arbeiten. Ihr habt durch Kollaboration und wissenschaftlichen wie privaten Austausch erheblich zum Entstehen meiner Dissertation beigetragen. Besonderer Dank gilt meinem Gruppenleiter Robert als Sparring-Partner für meine Pläne und Ideen und deinen Beitrag bei deren Umsetzung. Mojtaba, du hast mich als Masterarbeitsbetreuer endgültig für die Wissenschaft begeistert und auch nach der Masterarbeit konnte ich mich immer an dich wenden - danke dir. Jens und Daniel, meine Buddies, danke, dass ihr mir während meiner Promotion für alle meine Fragen zur Seite standet. Ich danke Susanne für die Lehrstuhlorganisation, der Buchhaltung, Karin, Heike und Sandra für die Unterstützung bei der Analytik und Zusammenarbeit im Labor, Caro und der Werkstatt für die Zellbauteile und Roman für die Unterstützung bei der Messtechnik.

Ang, Felipe, Nelson, Paul W., Nick und Wiebke, danke für die tolle Zeit im Büro und euer offenes Ohr. Danke an die 'Endstation-DWI' für die lustigen, erholsamen Mittagspausen und das leckere Essen in den Kochwochen. Liebe Mucos, mit euch konnte ich Erfolge sowie Herausforderungen teilen. Danke für eure Perspektiven, die konstante Unterstützung und das Feiern der kleinen wie großen Erfolge. Carla, Flo, Lukas und Tobi, vielen Dank für euren wertvollen Input zu meinem Vortrag und der Dissertation, aber auch weit darüber hinaus.

Ich danke dem Zukunftscluster Wasserstoff und den Projektpartner:innen im Projekt HyInnoSep für den Austausch und die erfolgreiche Zusammenarbeit.

Insbesondere danke ich allen Studierenden, die im Team-EHC mit mir zusammen geforscht haben. Ihr habt einen großen Beitrag zu meiner Dissertation geleistet und ich habe viel von euch und mit euch gelernt: Alexander Jachertz, Lars Rammelkamp, Philipp Scheurenberg, Maurice Feulbach, Stefanos Keloglou, Malte Wehner, David Baaken, Marcel Schmengler, Richard Steinberger, Nicolas Mulandi, Lara Lagner, Yannick Rau, Maria Arias Valcarcel, Henri Pelzer, Alexander Bauer, Xianbin Qiu, Sebastian Bektesi, Andrey Kirsanov, Lena Riechers, Nick Semrau, Zeina Nasr und Daniel Onyeche.

Von Herzen danke ich meiner Familie, Mama, Papa, Erwin, Jojo, Lukas, Marci, Sophia und meinen engen Freunden. Danke für eure bedingungslose Unterstützung und euer Vertrauen in mich und meinen Weg. Daniel, ich danke dir für deine Zuversicht und deine Unterstützung, die du mir jeden Tag schenkst.

Suchen heißt: ein Ziel haben.
Finden aber heißt: frei sein, offen stehen, kein Ziel haben.

- Hermann Hesse, Siddartha

Abstract

Hydrogen will be a key component of a zero-emission energy system, enhancing resilience and aiding in decarbonizing hard-to-abate sectors. For mid-term hydrogen distribution and storage, blending hydrogen into the natural gas grid presents a viable option that necessitates decentralized compression and separation technologies, as hydrogen must be compressed to achieve competitive volumetric energy density. Existing technologies, such as mechanical compression and pressure swing adsorption, are not well suited for distributed hydrogen compression and separation and often entail high footprints and capital costs. Electrochemical hydrogen compression is an evolving technology combining separation and compression, delivering high hydrogen purity and operational flexibility. This thesis aims to advance electrochemical hydrogen compression applicability in natural gas mixtures by increasing process robustness against impurities and reducing costs through innovative reactor design.

Low- and high-temperature electrochemical hydrogen compressor (EHC) systems are compared in this work, assessing their performance and poisoning tolerance in the presence of single impurities (CO_2, CO, NH_3, H_2S) at natural gas concentrations. In the low-temperature EHC, detrimental performance reductions due to impurities were observed. With impurity/hydrogen mixtures, the high-temperature EHC demonstrated stable operation, minimal potential increase, and higher product gas purity compared to the low-temperature EHC. However, diluting the H_2S/ hydrogen feed with methane resulted in severe potential oscillations. Several mitigation strategies were implemented to address H_2S poisoning in the high-temperature EHC, with repetitive cyclic voltammetry proving the most effective and efficient. Furthermore, an innovative tubular reactor design was developed alongside a 2D numerical model. This work established a proof-of-concept for the tubular EHC design. The modeling results indicated the process competitiveness of EHC technology compared to state-of-the-art separation and compression methods, highlighting its potential for integration into future hydrogen distribution systems.

This research demonstrates the capability of high-temperature EHCs to simultaneously compress and separate hydrogen from natural gas mixtures containing critical impurities. By developing innovative reactor designs and demonstrating effective mitigation strategies for poisoning effects, this work advances EHC technology, paving the way for its integration into hydrogen distribution systems.

Zusammenfassung

Wasserstoff wird eine Schlüsselkomponente eines emissionsfreien Energiesystems sein, die die Systemresilienz erhöht und die Dekarbonisierung von „Hard-to-abate“-Sektoren ermöglicht. Für die mittelfristige Wasserstoffverteilung stellt die Einspeisung von Wasserstoff in das Erdgasnetz eine praktikable Option dar. Diese benötigt jedoch dezentrale Wasserstoffabscheidetechnologien und Verdichtungstechnologien, um eine wettbewerbsfähige volumetrische Energiedichte von Wasserstoff zu erreichen. Die bestehenden Technologien, mechanische Kompression und Druckwechseladsorption, sind für die dezentrale Wasserstoffkompression und -abtrennung durch hohen Platzbedarf und Kapitalkosten, nicht gut geeignet. Elektrochemische Wasserstoffkompression ist eine aufstrebende Technologie, die Trennung und Verdichtung kombiniert, sowie hohe Wasserstoffreinheit und betriebliche Flexibilität erzielt. Diese Arbeit zielt darauf ab, die Anwendbarkeit der elektrochemischen Wasserstoffkompression in Erdgasgemischen zu verbessern, indem die Prozessrobustheit gegenüber Verunreinigungen erhöht und die Kosten durch ein innovatives Reaktordesign gesenkt werden.

In dieser Arbeit werden nieder- und hochtemperatur elektrochemische Wasserstoffkompressoren (EHC) hinsichtlich ihrer Leistung und Vergiftungstoleranz in Gegenwart einzelner Verunreinigungen (CO_2, CO, NH_3, H_2S) verglichen. Im niedrigtemperatur -EHC wurde eine starke Leistungsminderung durch die Dosierung der Verunreinigungen beobachtet. Der hochtemperatur-EHC konnte mit Verunreinungsbeimischung im Wasserstofffeed, unter einem minimalen Potentialanstieg, stabil betrieben werden. Die Verdünnung des H_2S/Wasserstoff Feedgases mit Methan führte zu starken Potentialoszillationen. Folglich wurden Strategien zur Eindämmung der Vergiftung durch H_2S im hochtemperatur-EHC entwickelt und getestet, wobei sich die wiederholte zyklische Voltammetrie als die effektivste und effizienteste erwies. Darüber hinaus wurde ein innovatives röhrenförmiges Reaktordesign und ein numerisches 2D Modell des Reaktors entwickelt. Es wurde ein Proof-of-concept für das röhrenförmige EHC-Design erbracht. Die Modellierungsergebnisse zeigten die Wettbewerbsfähigkeit der EHC-Technologie im Vergleich zu etablierten Trenn- und Kompressionsmethoden und unterstrichen ihr Potenzial für die Anwendung in Trenn- und Kompressionsaufgaben.

Diese Forschungsarbeit demonstriert die Kombination von Wasserstoffverdichtung und -abtrennung aus Erdgasmischungen in einem hochtemperatur-EHC. Durch die Entwicklung innovativer Reaktorkonzepte und die Demonstration wirksamer Strategien zur Eindämmung von Vergiftungseffekten steigert diese Arbeit die Anwendbarkeit der EHC-Technologie in Wasserstoffverteilungssystemen.

Contents

1 Introduction and Scope

Transitioning to a zero-emission energy system mandates transformation in sectors with high green house gas (GHG) emissions. Electricity generation and industrial processes are responsible for $>$65 % of the global greenhouse gas emissions and, thus, should be targeted in decarbonization action [Lamb2021; Hert2018]. Transitioning to renewable energy and electrifying industry is the central strategy to mitigate GHG emissions. However, achieving complete decarbonization in hard-to-abate sectors, such as industry and high-temperature heat applications, presents challenges when relying solely on electrification [Sahr2024]. Consequently, converting electrical energy into carbon-free chemical energy carriers should be implemented to enable the decarbonization of hard-to-abate sectors, while also dampening the volatility of renewable energy and increasing energy system resilience [Ange2025]. Among carbon-free carriers, green hydrogen is seen as a central part of a decarbonized energy system due to its versatility in use, compatibility with existing infrastructure, ability to produce high-grade heat, and ease of production via water electrolysis [Sahr2024]. Hydrogen is already a widely used commodity, serving as a feedstock in various industrial applications, including refineries, as well as the production of ammonia and methanol. To reach competitiveness with other energy carriers and storage options, hydrogen needs to be compressed to at least 350 bar, at the cost of about 10 % of the energy content of hydrogen [Fran2024]. Consequently, optimizing hydrogen compression is targeted in research and development.

Hydrogen must be distributed after compression to be available at the respective site. Delivery via truck is the most economical method for transporting small amounts of hydrogen. Once the hydrogen demand expands, transport via a hydrogen pipeline will become more favorable; however, investment and time are needed to establish the network [Demi2018]. As a midterm solution and to enable long-term hydrogen distribution to remote locations, several EU countries, including Germany, aim to enable hydrogen blending into the natural gas grid by 2030 [Mela2013]. Additionally, green hydrogen blending would have an immediate positive effect on GHG emissions from natural gas appliances [Maha2022]. Separation and compression technology is necessary to extract hydrogen from the natural gas grid or biogas facilities. Currently, there are limited technologies available for decentralized separation and compression of hydrogen from gas mixtures, such as natural gas, that achieve high purities necessary for most applications [Rhan2020].

Electrochemical hydrogen compression is a promising technology providing high recovery rates and hydrogen purity in a single step while maintaining high efficiency, even in small-scale operations [Nord2019; Mrus2024]. Moreover, electrochemical hydrogen compressors (EHCs) integrate both hydrogen compression and separation into a single operational unit, which serves as a significant advantage for applications involving impure hydrogen or gas mixtures, such as blended natural gas [Durm2021]. Electrochemical hydrogen compression is a non-mechanical compression technology that compresses hydrogen without moving parts, lowering maintenance needs. The compression principle of an EHC is electrochemical, yielding higher theoretical compression efficiencies than mechanical ones [Kee2019]. However, several challenges still hinder the successful implementation of EHCs in industrial applications. Key challenges include minimizing energy demand (cell potential), enhancing process robustness against gas impurities commonly found in feedstock gases, and reducing costs associated with the electrochemical cell stack [Zou2020; Piva2024].

To address the challenges associated with EHCs, this thesis examines operational process design and reactor design. Through experimental in-

vestigation guided by the following research questions, we aim to enhance the EHC performance in terms of efficiency and stability under realistic operating conditions.

Main research question: How to increase the robustness and efficiency of EHC?

Following an approach focused on process and reactor design presented in Figure 1.1, this thesis advances the understanding of EHC operation in natural gas and process robustness and presents an innovative reactor design for cost reduction. Chapter 2 provides an overview of hydrogen compression and separation technologies. Additionally, the working principle of an EHC is presented, along with an overview of the state-of-the-art literature on the topic. The sub-questions of each chapter, aiding to answer the main question of the thesis, are elaborated below.

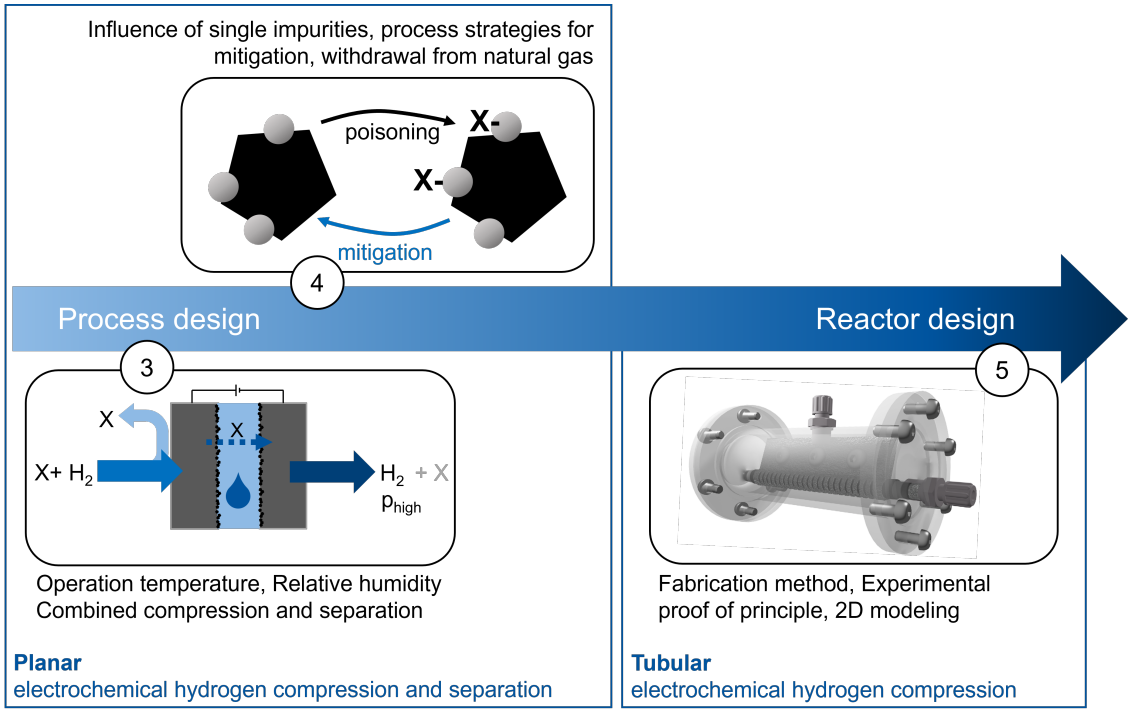

Figure 1.1: Structure of the chapters presented in this thesis.

Sub-question 1: How do low- and high-temperature EHCs compare regarding hydrogen compression and separation performance?

To facilitate future critical technology assessments, different types of EHCs are compared in terms of polarization behavior, as well as separation and compression performance. Achieving hydrogen purities of at least 99.999 % is essential to meet the standards required for most applications. Therefore, Chapter 3 investigates the purity levels attainable with both low- and high-temperature EHCs. Operations conducted near the limiting current are also examined to maximize the hydrogen recovery rate, providing insights into optimizing the EHC performance for practical applications.

Sub-question 2: What is the influence of trace impurities present in the natural gas grid on EHCs and how to mitigate them?

For the effective operation of EHCs in withdrawing hydrogen from natural gas or other gas mixtures, these systems must maintain functionality in the presence of various impurities typically found in natural gas. Natural gas often contains trace amounts of contaminants such as carbon dioxide (CO_2), carbon monoxide (CO), hydrogen sulfide (H_2S), ammonia (NH_3), and other hydrocarbons. These impurities can significantly affect the performance and longevity of EHCs by interfering with the electrochemical reactions necessary for efficient hydrogen separation and compression. In Chapter 4 the influence of single trace impurities on EHC performance under various process conditions are examined. Additionally, mitigation strategies for reducing the impact of these contaminants are explored to enhance operational stability and efficiency.

Sub-question 3: Can a tubular EHC be built and operated?

Reducing the cost of electrochemical cell stacks is crucial for enhancing the economic feasibility of EHCs. As bipolar plates account for approximately 51 % of the total stack cost, designing novel electrochemical cell geometries can facilitate future reductions in capital cost [Inte2020]. Chapter 5 explores the production procedure and experimental proof of principle in hydrogen compression of a tubular EHC. A 2D model of the tubular and planar EHC was developed to investigate electrochemical cell design parameters, such as porosity, and to compare technology competitiveness with state-of-the-art designs. The tubular EHC design addresses cost concerns and provides additional benefits, such as improved reactor sealing, optimized flow conditions, and enhanced pressure distribution within the membrane electrode assembly.

Previous Publications in Student Theses

This thesis includes contributions of the following student theses written under the supervision of Wibke Zängler:

- Alexander Jachertz, 2021, Bachelor's thesis, Production of a tubular membrane electrode assembly for usage in electrochemical hydrogen compression
- Richard Steinberger, 2022, Master's thesis, Production and characterization of a tubular electrochemical hydrogen compressor
- Lara Lagner, Yannick Rau, 2022, Project thesis, Contacting of a tubular electrochemical hydrogen compressor
- Maria Laura Arias Valcarcel, 2023, Bachelor's thesis, Optimization of a tubular electrochemical hydrogen compressor focusing on contacting methods.
- Stefanos Keloglou, 2023, Bachelor's thesis, Modelling of a planar and tubular electrochemical hydrogen compressor in Matlab
- Nick Semrau, 2024, Master's thesis, Investigation of Catalyst Poisoning and Performance Optimization in High-Temperature Electrochemical Hydrogen Compression Using Polybenzimidazole Membranes for the Purification of Hydrogen from the Natural Gas Grid
- Zeina Nasr, 2024, Bachelor's thesis, Simultaneous compression and separation of hydrogen from natural gas-hydrogen mixtures using high-temperature electrochemical hydrogen compression

2 Fundamentals and State of the Art

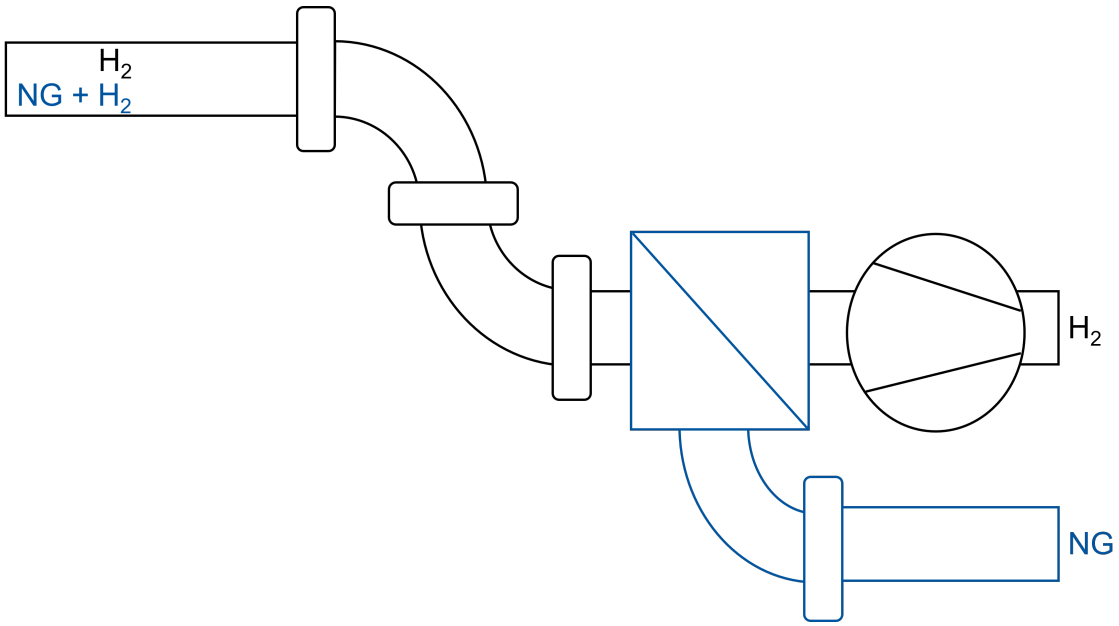

2

2.1 Hydrogen compression

Due to the very low volumetric energy density of hydrogen, compression is an essential unit operation in the envisioned hydrogen economy [Abe2019; Pesc2020]. Hydrogen compression technology is categorized according to its compression principle into mechanical and non-mechanical compressors [Fran2024]. Mechanical compressors, which are state-of-the-art and most widely used in hydrogen applications, function as positive volume displacement devices. The confined volume, in which hydrogen is contained, is reduced, leading to an increase in pressure according to ideal gas law. Various mechanical hydrogen compressor designs are available. The most commonly used are reciprocating piston compressors, diaphragm compressors, and linear compressors [Sdan2019a]. The disadvantages of mechanical compressors include moving parts, high investment and maintenance costs, contamination, and noise [Zou2020]. Among the non-mechanical compressors are cryogenic compressors, combining liquefaction and compression, metal hydride compressors, adsorption compressors, and electrochemical hydrogen compressors [Ayku2023].

2.2 Hydrogen separation

To date, hydrogen is mostly produced by steam methane or coal reforming, needing gas separation to gain hydrogen in the necessary purity for industrial applications such as hydrogenation. The most widespread technology for hydrogen purification is pressure swing adsorption (PSA) due to its techno-economic feasibility for large-scale hydrogen separation [Nord2021; Lube2022]. Other technologies employed for hydrogen separation are cryogenic, pressure-driven membranes, metal hydrides, and electrochemical hydrogen compression [Ayku2023].

In PSA, the impurities are removed by preferential adsorption of the impurities to the adsorbent bed. PSA can deliver high purities ($>$99.99 %) at moderate recoveries (typically 75 %). The PSA is operated as a cyclic process, with multiple columns to enable continuous operation. Figure 2.1

illustrates a two-column PSA. One simplified cycle of an adsorption column can be structured into four main steps: Pressurization of the column, adsorption of the impurities on the adsorbent, depressurization of the column, and desorption at low pressures. A detailed description of the cycle for hydrogen purification can be found in the following manuscript [Relv2018].

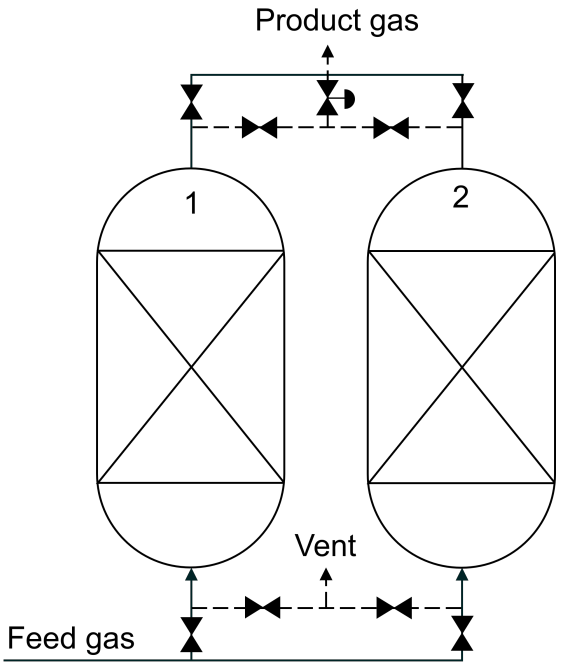

Figure 2.1: Flow sheet of a two-column pressure swing adsorption system.

In cryogenic hydrogen separation, hydrogen is separated due to volatility difference by decreasing the temperature of the gas mixture [Ayku2023]. Cryogenic hydrogen purification has high OPEX due to low operating temperatures and compression. It is mainly operated at large scale and can deliver moderate purity 90 to 99 % [Aasa2021]. Pressure-driven membrane processes with dense polymeric membranes work based on the permeability difference of the components in the gas mixture (Comp. Eqn. 2.6). They can achieve moderate purity, ranging from 95 to 98 %, and are applicable in small to medium-sized facilities. However, a pressure difference across the membrane is necessary as a driving force. Consequently, interstage compressors are needed [Amin2023]. Alternatively, metallic membranes, mostly made from palladium alloys, can deliver high purities $>$99.9 % but suffer from high CAPEX due to the noble metal membrane's high material

cost [Lube2022].

For the separation of low-concentration hydrogen, such as in hydrogen withdrawal from natural gas, hybrid processes gained scientific interest as they combine the merits of different separation technologies [Liem2017; Nord2021]. Linde and Evonik, for example, have developed a combined membrane and PSA process to separate hydrogen from natural gas, achieving a hydrogen purity of 6.0 [Purr2021].

However, the traditional technologies described earlier require at least two separate unit operations to compress and separate hydrogen from gas mixtures, resulting in increased equipment needs and a larger footprint. For future process intensification in distributed hydrogen applications, it is essential to integrate the functions of compression and separation into a single system. Furthermore, electrifying the separation process is desirable to support the energy transition.

2.3 Electrochemical Hydrogen Compression

Electrochemical hydrogen compressors (EHCs) emerge as a promising alternative by simultaneously addressing compression and purification within one compact system and are currently under investigation and development for applications in hydrogen withdrawal from gas mixtures [Chhe2024]. A timeline of the most critical developments in electrochemical hydrogen compression and separation is presented in Figures 2.2 to 2.4.

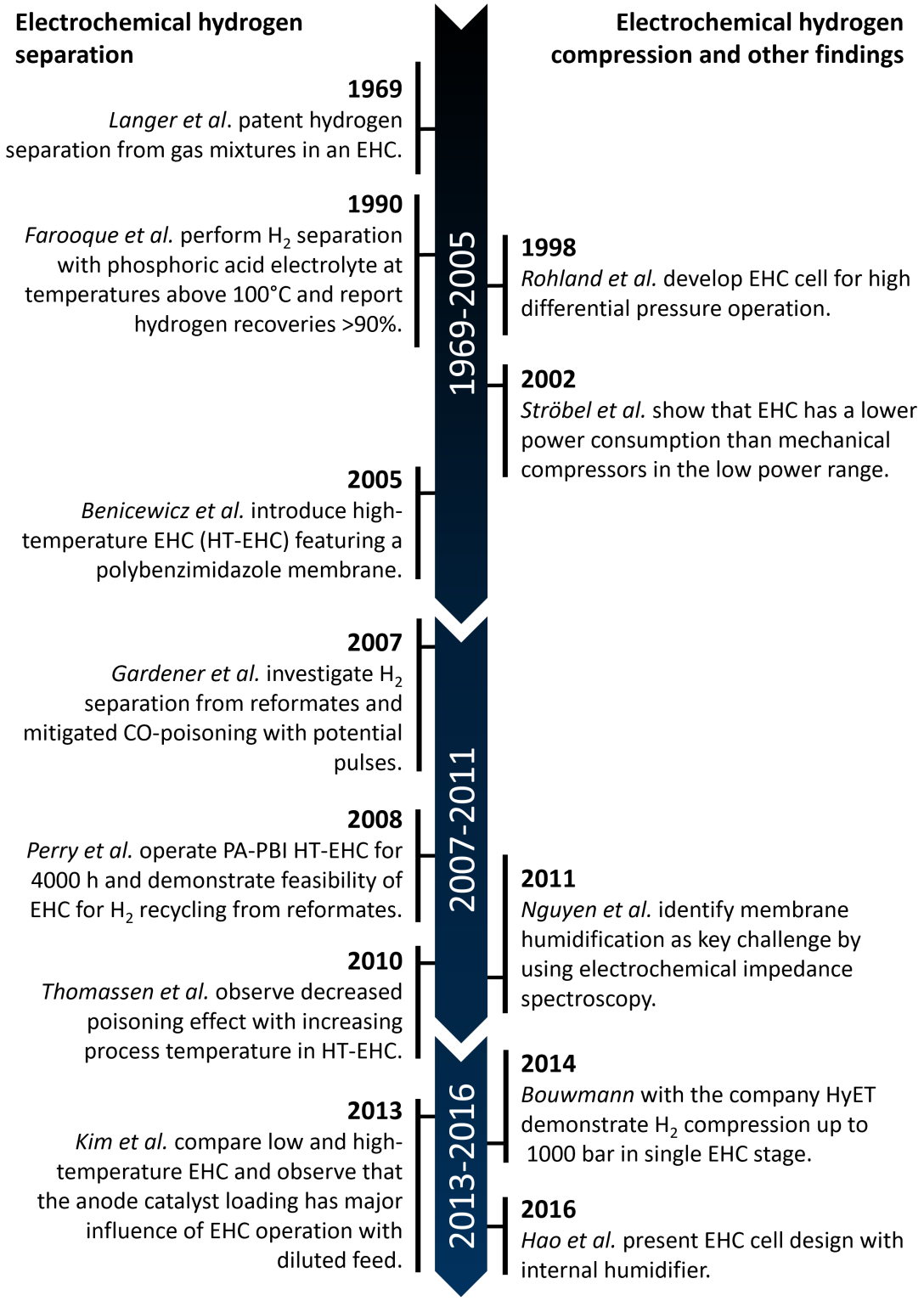

Figure 2.2: Findings and development in electrochemical hydrogen separation (left) and electrochemical hydrogen compression (right).

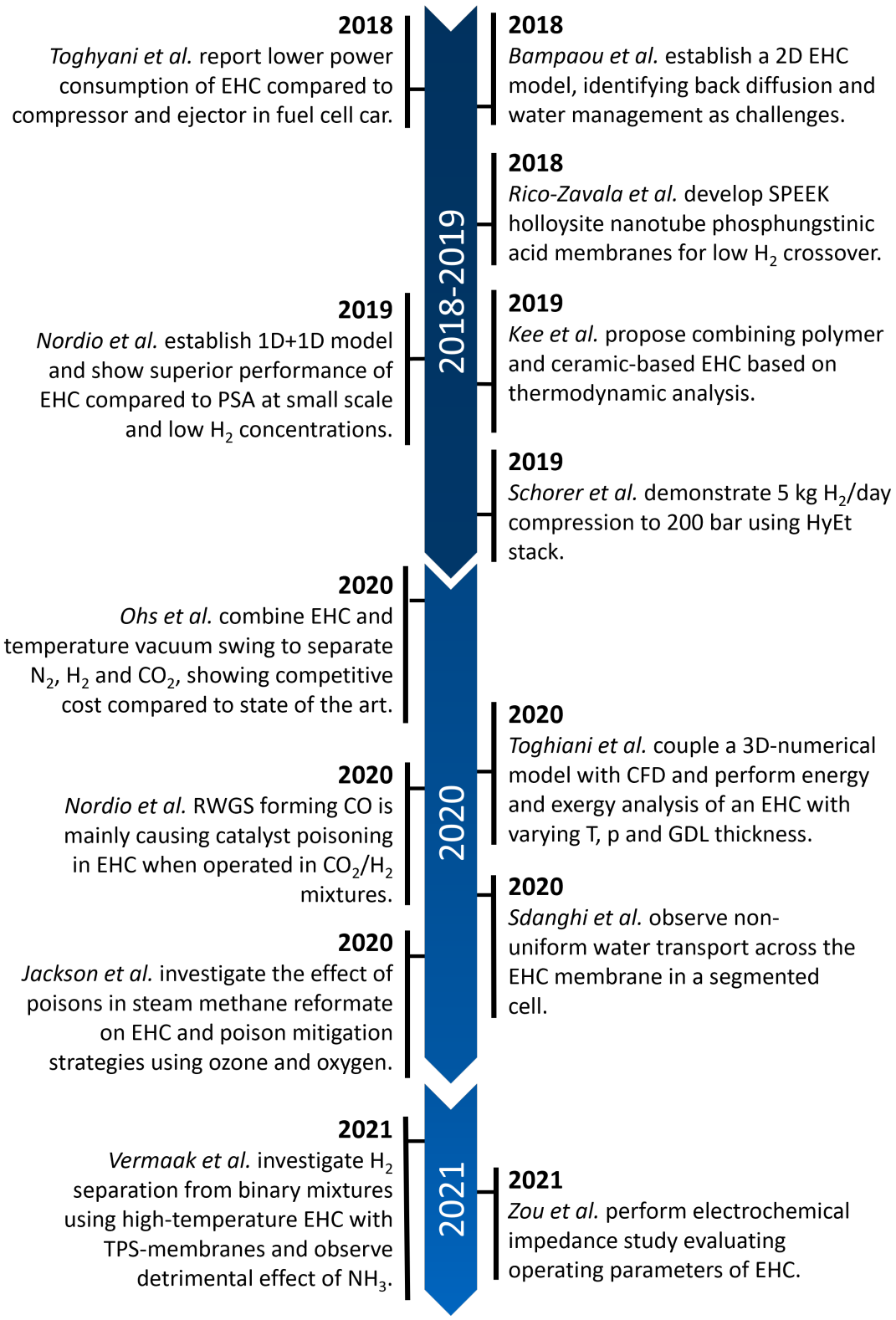

Figure 2.3: Findings and development in electrochemical hydrogen separation (left) and electrochemical hydrogen compression (right).

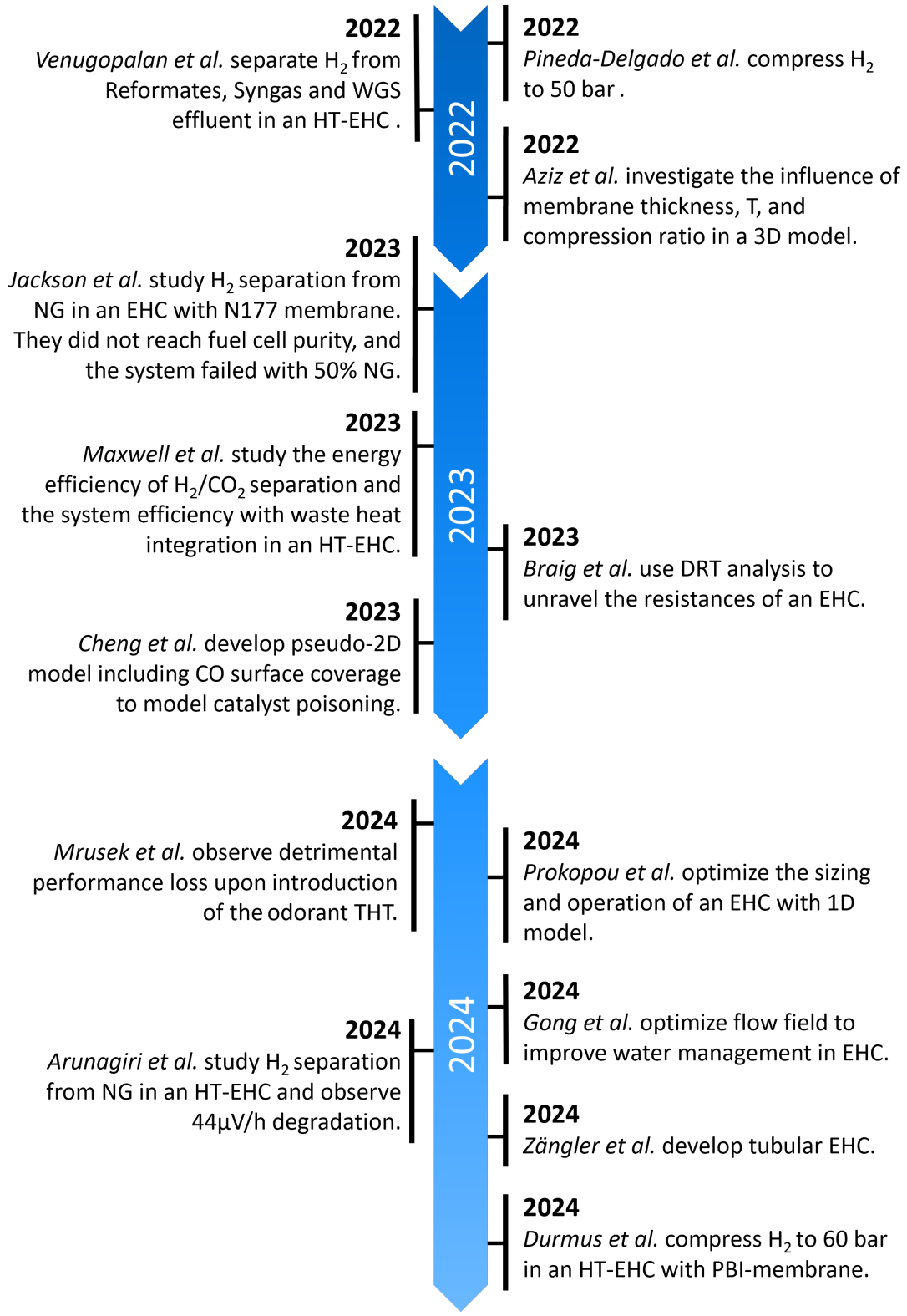

Figure 2.4: Findings and development in electrochemical hydrogen separation (left) and electrochemical hydrogen compression (right).

Figure 2.5 illustrates the working principle of an EHC. On the EHC's anode, hydrogen from a pure feed or a gas mixture is selectively oxidized (hydrogen oxidation reaction (HOR), Eqn. 2.1). Impurities X in the feed are retained by the proton exchange membrane, enabling hydrogen separation. The formed protons migrate towards the cathode governed by the electrical driving force applied to the system. On the cathode, the protons are reduced, and hydrogen at a higher partial pressure evolves (hydrogen evolution reaction (HER), Eqn. 2.2) [Lang1969; Mage1970].

$$H_2 \longrightarrow 2\,H^+ + 2\,e^- \tag{2.1}$$

$$2\,H^+ + 2\,e^- \longrightarrow H_2 \tag{2.2}$$

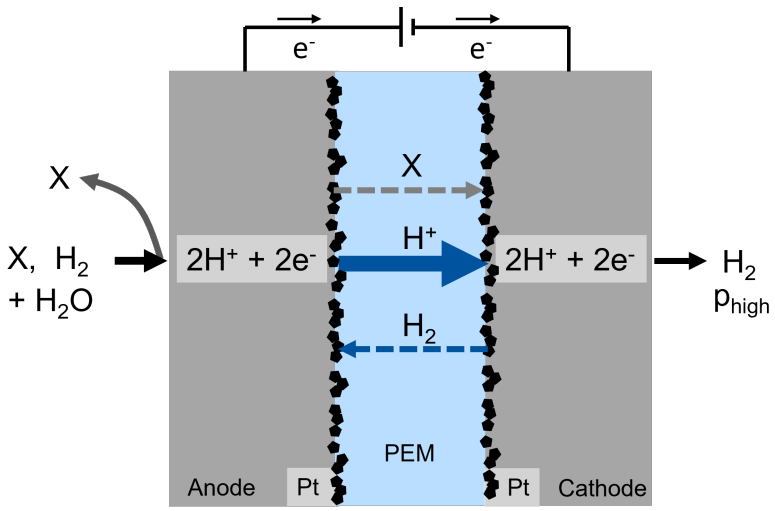

Figure 2.5: Working principle of electrochemical hydrogen compression.

The increase in hydrogen partial pressure from the anode (p_a) to the cathode side (p_c) is governed by the Nernst potential E_N (Eqn. 2.3) with R the ideal gas constant, T the process temperature, z = 2 the number of electrons transferred in the reaction and F the Faraday constant. For the EHC, the Nernst equation simplifies as the thermodynamic equilibrium potential

(E_0) of the HOR and HER are 0 V vs. SHE [Zou2020].

$$E_N = E_0 + \frac{RT}{zF} \ln \frac{a_c}{a_a} = \frac{RT}{2F} \ln \frac{p_{H_2,c}}{p_{H_2,a}} \tag{2.3}$$

The Nernst potential is the thermodynamic minimum potential required to achieve a desired compression ratio. However, additional losses, namely the activation overpotential (E_η), the potential caused by ohmic losses in the cell (E_{ohm}) and by mass transport ($E_{MassTransport}$), need to be considered in terms of cell potential [Zosk2007; Chou2020].

$$E_{cell} = E_N + E_\eta + E_{ohm} + E_{MassTransport} \tag{2.4}$$

The molar amount of hydrogen pressurized ($\dot{n}$) or purified in the cell depending on the cell's current is determined by Faraday's law (Eqn. 2.5), with the current flowing in the EHC (I), z number of electrons transferred in the reaction (for EHC: $z = 2$) and F the Faraday constant ($F = 98\,485\,\mathrm{C\,mol^{-1}}$)

$$\dot{n} = \frac{I}{2F} \tag{2.5}$$

However, partial pressure gradient driven back diffusion of hydrogen from the cathode to the anode compartment occurs, reducing the output of the EHC. The diffusion through non-porous polymeric membranes, as molar flux $\dot{n}''$, can be described by the solution-diffusion model, with the diffusion coefficient D_i, the molar concentration c_i and the membrane thickness δ [Wijm1995].

$$\dot{n}'' = D_i \cdot \frac{c_{i,feed} - c_{i,product}}{\delta} \tag{2.6}$$

By assuming a Henry relation and ideal gas behavior, the concentration is linearly dependent on the partial pressure p_i, and equation 2.6 can be

simplified to

$$\dot{n}'' = \frac{D_i \cdot S_i}{\delta} \cdot (x_i \cdot p_{feed} - y_i \cdot p_{product}) \tag{2.7}$$

The product of the diffusion and Henry coefficient (S_i) is described as the permeability (P_i) of a material.

$$P_i = D_i \cdot S_i \tag{2.8}$$

In the case of electrochemical hydrogen separation, the molar flux of impurities to the cathode can also be described by equation 2.7. The back diffusion molar hydrogen flow is derived by multiplying the flux with the membrane area (A_{mem}).

$$\dot{n}_{back} = A_{mem} \cdot \frac{D_{H_2} \cdot S_{H_2}}{\delta} \cdot (x_{H_2} \cdot p_{feed} - y_{H_2} \cdot p_{product}) \tag{2.9}$$

With the definition of back diffusion, the effective hydrogen molar flow to the cathode can be expressed as the sum of the molar flow from Faraday's law ($\dot{n}$) and the molar flow of back diffused hydrogen ($\dot{n}_{back}$) [Pine2022b].

$$\dot{n}_{eff} = \dot{n} + \dot{n}_{back} \tag{2.10}$$

In contrast to conventional mechanical compressors, which work isentropic at best, the limiting thermodynamic case for EHCs is isothermal compression. Isothermal compression thermodynamically needs less compression work to achieve the same compression ratios, consequently EHCs can achieve higher theoretical compression efficiency, qualitatively displayed in Figure 2.6 [Kee2019]. The general definition of specific work (w) for compression, assuming the idealization of reversible heat transfer, is

$$w = \Delta h - T\Delta s \tag{2.11}$$

For isothermal compression, describing EHC, where $\Delta h = 0$, the following definition of specific compression work can be derived by assuming the ideal gas law $pV = nRT$, with the system pressure p, volume V, the molar mass n, the ideal gas constant R (8.314 J mol^{-1} K^{-1}) and temperature T [Kee2019].

$$w = RT \ln \frac{p_{out}}{p_{in}} \tag{2.12}$$

For determining the thermodynamic ideal work of compressing hydrogen in an EHC under isothermal conditions, the effective molar amount of hydrogen transported through the EHC, which is calculated as the product of the effective molar flow and compression time t ($n_{eff} = \dot{n}_{eff} t$), is used.

$$W_{isothem,ideal} = n_{eff} \cdot RT \ln \frac{p_c}{p_a} \tag{2.13}$$

However, the back diffusion of hydrogen compromises compression efficiency, and the actual work W_{actual} of an EHC is calculated based on the cell voltage of the EHC and total charge [Pine2022b].

$$W_{actual} = E_{cell} \cdot 2Fn \tag{2.14}$$

The specific work of isentropic compression in mechanical compressors, where $\Delta s = 0$ can be described by [Kee2019]

$$w = \Delta h = \int V(s,p)\, dp \tag{2.15}$$

In practice, several compression stages and interstage cooling are necessary in mechanical compressors, resulting in polytropic operation. Consequently, a polytropic compression process describes mechanical compression with the polytropic index n=1.36 [Taha2022; Fran2024; Suer2017]. For example, Franco et al. [Fran2024] analyze optimized multi-stage mechanical compression of hydrogen regarding compression work and state 11 MJ/kg compression work for compression to 35 MPa, which is equivalent

to 1.4 times the isothermal compression work required.

$$w_{pol} = \frac{n}{n-1} \cdot RT_1 \left[\left(\frac{p_2}{p_1} \right)^{\frac{n-1}{n}} - 1 \right] \tag{2.16}$$

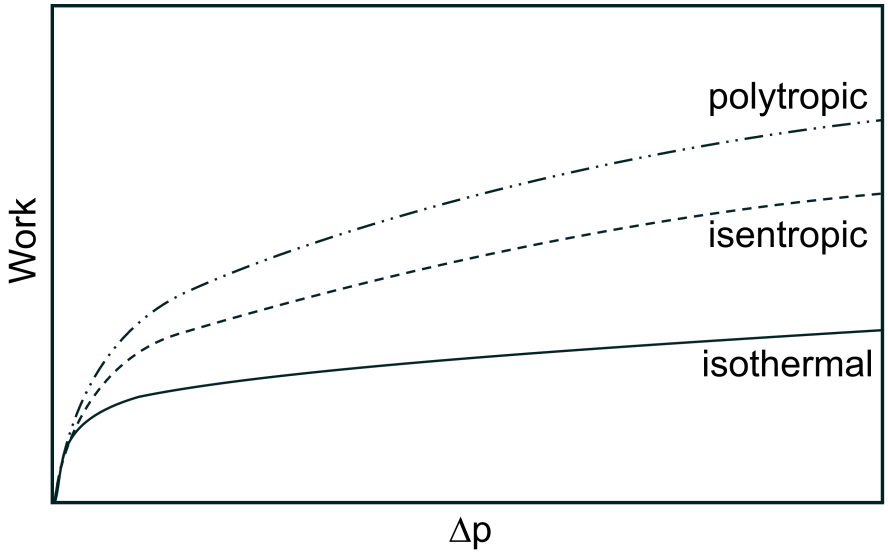

Figure 2.6: Qualitative comparison of work for compression with rising pressure difference when compressing isothermal, isentropic and polytropic.

Table 2.1 compares key performance indices of mechanical and electrochemical compression. The energy demand for electrochemical compression is slightly higher than that for mechanical compression, resulting in higher operational costs. However, EHCs offer higher availability, meaning the share of time the device can be operated, lower capital cost, and combined compression and separation [Sdan2019a; Fran2024; Bouw2014; Chhe2024; Prok2025]. To reach economic feasibility of EHCs a lifetime of 15-20 years, and high current densities $>2\,\mathrm{A\,cm^{-2}}$ need to be achieved while maintaining a low cell voltage $<0.5\,\mathrm{V}$ and a pressure difference of 50 to 70 bar [Trég2020; Piva2024]. The remaining challenges hindering the merit of EHCs are reaching low cell voltages and, thus, operational costs, lowering the proton exchange membrane gas permeability and process robustness against feed gas impurities [Trég2020; Zou2020].

Table 2.1: Comparison of hydrogen compression from 1 atm to 350 bar using mechanical or electrochemical compressors.

	Mechanical Compressor	**Electrochemical Compressor**
Energy demand	2.7 - 11	3 - 15
[kWh/kg_{H2}]	[Fran2024]	[Bouw2014; Chhe2024; Prok2025]
Availability	70 - 90	>99
[%]	[US D2015]	[HyET]
Capital Cost	400 - 2300	150 - 1500
€/kg_{H2}	[HyET; Chhe2024]	[HyET; Chhe2024]

2.3.1 Electrochemical hydrogen compressor configurations

The EHC stack's functional unit is the membrane electrode assembly (MEA). As shown in Figure 2.5, EHC MEAs are built in a zero-gap configuration, meaning no gap exists between the electrodes, catalyst layers, and the proton exchange membrane (PEM). MEAs can be fabricated by assembling anode and cathode gas diffusion electrodes with a proton exchange membrane. EHC gas diffusion electrodes primarily consist of carbon-based woven or non-woven materials, comprising a microporous layer and a catalyst coating. Alternatively, catalyst-coated membranes, in which the catalyst is directly applied onto the PEM, can be sandwiched between gas diffusion layers. Adjacent to the MEA, bipolar plates are placed for current supply and gas distribution through gas flow fields. Cell fixtures, including gaskets and end plates secured with bolts, are also required to assemble an EHC [Verm2021b; Durm2021; Zou2021].

EHCs are categorized by operating temperature and the respective ion exchange material used to separate the electrodes. An overview of the EHC types is shown in Figure 2.7. Low-temperature EHCs operating between 30 to 90 °C are mainly built with PFAS-based proton exchange mem-

branes. The most commonly used membrane is Nafion™. The operation of the low-temperature EHC is limited to temperatures below 90 °C as the proton transfer of Nafion™ relies on water, and at higher temperatures, the membrane dries out, significantly decreasing the membrane proton conductivity [Nguy2011; Jack2023]. High-temperature EHCs with acid-doped hydrocarbon membranes can be operated between 120 to 200 °C. Additionally, they can be operated in anhydrous conditions. The higher operating temperature increases the process's robustness against impurities in the feed gas of the EHC [Perr2008; Rico2018; Maxw2023]. Solid oxide EHCs, in contrast to low and high-temperature EHCs, work with ceramic proton conductors. Their operating temperature lies between 300 to 1000 °C. Due to their high operating temperature, the energy demand is high compared to the EHCs based on polymeric membranes; however, their operation is robust against feed impurities [Kee2019].

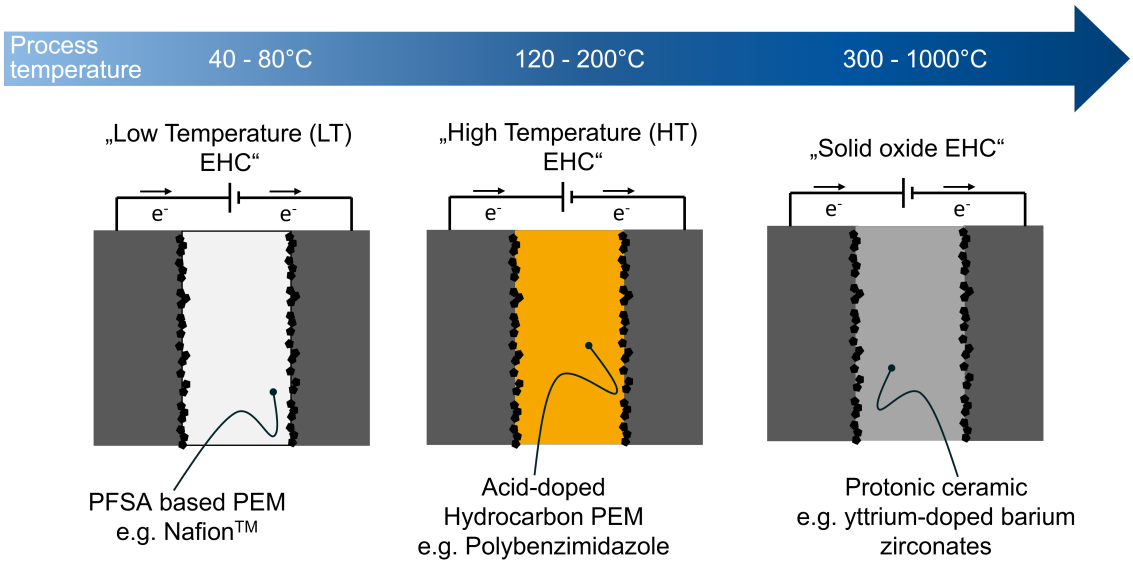

Figure 2.7: Overview of EHC types divided by operating temperature and respective proton exchange materials.

EHC electrocatalysis

Noble metal catalysts are predominantly employed in EHC, with platinum and its alloys being the most widely used due to high catalytic activity for the HOR and HER. Alloys with less noble metals (Pd, Ir, Ru) are proposed

to increase HER activity and decrease CO poisoning [Bal2023; Ayku2022; Wu2012]. Additionally, there is growing interest in non-precious metal catalysts and carbon-based materials doped with heteroatoms for HOR and HER [Trég2020; Lu2016]. Recently, Chhetri et al. [Chhe2024] demonstrated EHC operation with a platinum group metal free molybdenum oxide aerogel.

The HOR and HER either follow the Tafel-Volmer or the Heyrovsky-Volmer mechanism. During the Tafel reaction, hydrogen adsorbs dissociatively to Pt without electron transfer (Eqn. 2.17), while during the Heyrovsky reaction, one hydrogen atom adsorbs with simultaneous release of a proton and electron (Eqn. 2.18). H_{ads} denotes an adsorbed hydrogen atom and $Pt\cdot$ is a free adsorption site of the catalyst. During the Volmer reaction (Eqn. 2.19), the adsorbed hydrogen atom is discharged, and a proton and electron are released [Lu2016].

$$\textit{Tafel} : H_2 + 2\,Pt\cdot \longrightarrow 2\,Pt{-}H_{ads} \tag{2.17}$$

$$\textit{Herovsky} : H_2 + Pt\cdot \longrightarrow Pt{-}H_{ads} + H^+ + e^- \tag{2.18}$$

$$\textit{Volmer} : Pt{-}H_{ads} \longrightarrow H^+ + e^- + Pt\cdot \tag{2.19}$$

2.3.2 Proton transfer in ion exchange membranes for EHC

Proton conduction in PEMs is facilitated by three primary mechanisms: the Grotthuss, vehicular, and surface conduction [Agmo1995; Kreu1982]. The Grotthuss mechanism describes a sequential hopping of protons through a network of hydrogen-bonded molecules. More recent studies described the Grotthuss mechanism involving periodic isomerizations between Eigen

($H_9O_4^+$) and Zundel ($H_5O_2^+$) complexes. The proton conduction is triggered by hydrogen-bond cleavage and formation in the second solvation shell, facilitating incoherent proton hopping [Agmo1995]. The vehicular transport mechanism involves the diffusion of protons that are solvated by water molecules (acting as carriers) within the membrane's ionic domains, where increased hydration enhances proton conductivity [Kreu1982; Nase2012]. In contrast, the surface mechanism pertains to the transfer of protons between neighboring functional groups [Ludu2011]. However, the precise pathways and interactions that facilitate proton transport in PEMs remain a subject of ongoing debate within the scientific community.

Perfluorosulfonic acid (PFSA)-based membranes

The most widely used perfluor sulfonic acid (PFSA)-based ion exchange membrane is Nafion™, which comprises a hydrophobic polytetrafluoroethylene (PTFE) backbone and hydrophilic sulfonated side chains [Sava2014]. PFSA-based membranes exhibit a two-phase structure, where water is dispersed within a generally amorphous polymeric phase, resulting in clear phase separation between water pools and the perfluorinated matrix in swollen membranes [Gebe1997; Eike2001]. The structure of PFSA-based membranes at different humidification states is illustrated in Figure 2.8. This distinct phase separation is crucial for membrane functionality, as water solvates the polymeric acid side chains, thereby promoting proton mobility primarily through structural diffusion (i.e. Grotthuss) rather than vehicular motion. Water is critical for the formation of hydrated protons (Eigen ($H_9O_4^+$) and Zundel ($H_5O_2^+$)) and the mobility of protons in PFSA-based membranes [Feng2011; Padd2005]. Overall, proton conductance in ion exchange membranes is predominantly governed by bulk transport processes, including the Grotthuss and vehicular mechanisms, which are influenced by the dynamics of hydrogen bonding [Ludu2011]. However, the hydration requirements limit the operational temperature, restricting effective performance below the boiling point of water [Padd2005].

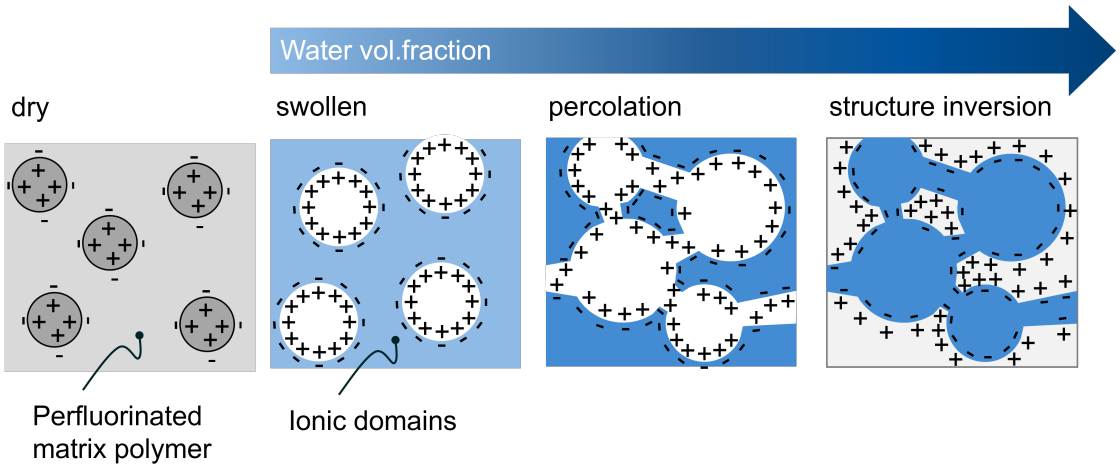

Figure 2.8: Morphology change of perfluorosulfonic acid membranes with increasing water content, adapted from [Gebe2000].

Polybenzimidazole-based membranes

In contrast to PFSA-based membranes, acid-doped polybenzimidazole (PBI) membranes can operate under anhydrous conditions, enabling operation at temperatures above 100 °C and reducing humidification complexity [Esco2020]. An overview of different PBI chemistries is given in [Seel2009]. Most research is focused on para-PBI, meta-PBI and AB-PBI. As the proton conductivity of pristine PBI is low, acid-doping of the polymer is employed to enhance proton conductivity [Esco2020]. Different strong acids have been studied and compared as doping agents for PBI [Esco2020; Bouc1999]. H_3PO_4 is the most commonly used and studied doping agent due to its high proton conductivity and low vapor pressure [Ma2004]. During doping, the basic PBI forms an ion pair with H_3PO_4 by accepting a proton. This interaction establishes a hydrogen bond based network between H_3PO_4 molecules and benzimidazole groups, favoring proton conduction. The number of acid molecules per repeating unit of PBI is the acid doping level. In dry PBI with high doping levels, proton hopping along acid-acid chains as displayed in Figure 2.9 is the prevalent conduction mechanism [Quar2012; Bouc1999]. Additionally, proton hopping between the N-H site to phosphoric acid anions and proton conduction via vehicle mechanism occurs but has little impact on proton conductivity [Ma2004].

Although H_3PO_4-doped PBI has good proton conductivity in anhydrous conditions, the conductivity can be increased with the introduction of water in highly doped membranes. The conductivity increases due to faster proton conduction mechanisms along H_3PO_4-anion-$H_2PO_4^-$ (Fig. 2.9) and H_3PO_4 - H_2O (Fig. 2.10) chains [Melc2017b]. However, even in anhydrous (dry) conditions, aqueous species exist in H_3PO_4-doped PBI, as they are found in H_3PO_4.

H_3PO_4-doped PBI can be generally prepared by casting the polymer in NaOH/ethanol or N,N-dimethylacetamide (DMAc) solution and subsequent acid immersion or direct casting of a PBI and H_3PO_4 in a solvent (e.g. trifluoroacetic acid). H_3PO_4-doped PBI membrane production via direct casting of PBI and H_3PO_4, also called PPA (polyphosphoric acid; sol-gel) process achieves higher doping levels and consequently, higher conductivities [Perr2014]. Commercial p-PBI membranes (BASF) produced by the PPA process exhibit a high degree of acid doping of up to 40 mol PA/repeating unit PBI [Xiao2005].

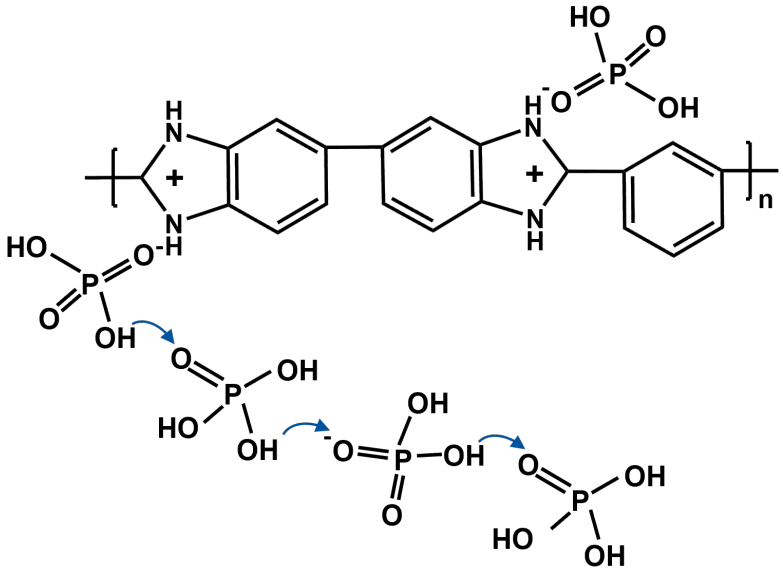

Figure 2.9: Proton transfer in H_3PO_4-doped meta-PBI along acid-acid.

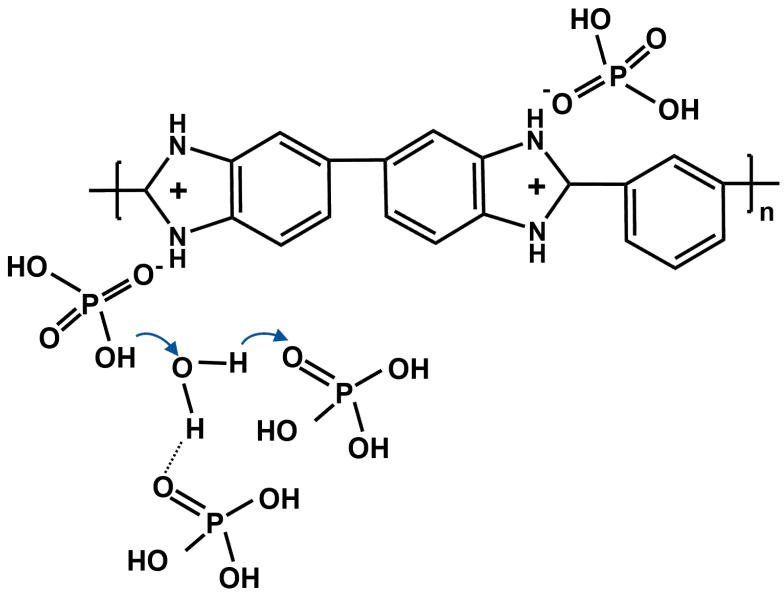

Figure 2.10: Proton transfer in H_3PO_4-doped meta-PBI along acid-H_2O.

2.3.3 Electroanalytics in EHC

For experimental investigation of electrochemical cells or reactions, the bulk properties of the components, electrode potentials, properties of interfaces between different phases (electrodes, catalyst, PEM), and characteristics (kinetics, mechanism) of the electrochemical reactions are of interest [Bago2005]. To deconvolute these aspects, electrochemical and non-electrochemical methods are employed. The following subsections will focus on the electrochemical analytics used throughout this thesis.

Electrochemical impedance spectroscopy

In electrochemical impedance spectroscopy (EIS), the sinusoidal response of an electrochemical system in equilibrium or steady state toward system perturbations by applying a sinusoidal signal with varying frequency is monitored [Bago2005]. EIS is used to analyze and discriminate electrical, electrochemical, and physical phenomena in the EHC. The various processes in the electrochemical cell exhibit different time constants, representing the time behavior of each process. EIS can be used to deconvolute these phenomena with different time constants as it is based on the frequency

regime [Laza2023]. Electrochemical impedance data is typically presented in Nyquist plots, as shown in Figure 2.12 presenting the negative imaginary $-Im(Z)$ over the real part of the impedance $Re(Z)$ at different frequencies. Semicircles represent processes with different time constants [Vivi2021]. The processes in the electrochemical system can be simulated by equivalent circuits consisting of passive and distributed elements (e.g. resistors, capacitors, constant phase elements) [Yuan2010].

The most common representation of an electrochemical system, including faradaic reactions, is the Randles circuit, presented in Figure 2.11 [Bard2001]. The overall current flows through the ohmic resistance (R_{ohm}) and is then divided between the capacitive current for charging and discharging of the electric double layer and the faradaic current. The faradaic process can be represented by a series of the charge transfer resistance R_{ct}, related to the kinetics and the Warburg impedance Z_w, describing the mass transport of the redox species in a semi-infinite linear diffusion boundary. Figure 2.12 (B) shows the Nyquist plot of a Randles cell. However, many electrochemical systems cannot be described using the Randles cell with a semi-infinite linear diffusion boundary but rather a finite boundary diffusion. Depending on the permeability of the boundary for the diffusing species, either a transmissive boundary (Figure 2.12 A) with a constant concentration profile or a reflective boundary (Figure 2.12 C) for which the flux of redox species is zero, is used [Laza2023].

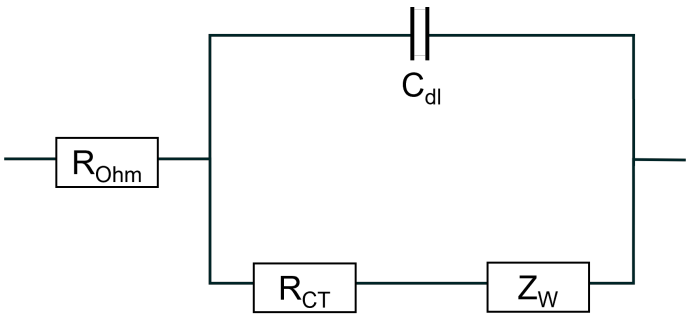

Figure 2.11: Randles equivalent circuit, with the ohmic resistance R_{ohm}, the charge transfer resistance R_{ct}, the mass transfer resistance R_m, the double layer capacitance C_{dl} and the Warburg impedance Z_w.

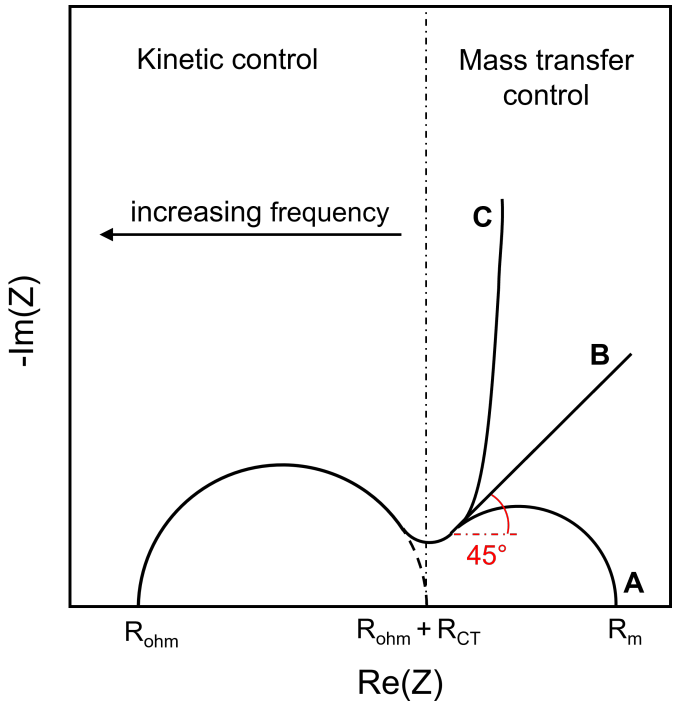

Figure 2.12: Schematic Nyquist plots showcasing different mass transport regimes.

In the field of electrochemical hydrogen compression, EIS was used to optimize the electrode microstructure, water management [Nguy2011], and operating conditions [Zou2021]. Additionally, a distribution of relaxation times (DRT) study of a high-temperature EHC was conducted, deconvoluting the different phenomena in the impedance response of the EHC [Brai2023]. Braig et al. [Brai2023] attributed the first semicircle to a combination of proton transfer in the GDE, the HER, and HOR. However, the time constants of the processes are too similar to be distinguished in the Nyquist plot.

Cyclic voltammetry

Cyclic voltammetry (CV) is a linear scan technique, during which the potential is cycled between the lower and upper switching potential with a linear scan rate, and the current response is recorded [Bard2001]. For EHCs, CV is mainly used to assess the electrocatalytic properties of catalyst materials employed in EHC systems [Ayku2022; Bal2023]. The catalytic perfor-

mance is characterized via analysis of catalyst degradation, catalyst activity and the electrochemically active surface area (ECSA) of Pt catalyst by hydrogen underpotential deposition. Additionally, ECSA analysis is used to quantify catalyst poisoning effects when operating EHCs with feed gas impurities [Wu2012]. Hydrogen underpotential deposition involves the controlled adsorption of hydrogen onto Pt electrodes at potentials more positive than those required for hydrogen evolution. Assuming only atomic H adsorbs onto the catalyst surface through the Volmer reaction while occupying exactly one active site per atom, the ECSA can be calculated from the observed charge transfer at low potentials corrected for double layer charging and charge density corresponding to a monolayer of adsorbed hydrogen [Luka2016]. Figure 2.13 shows an exemplary cyclic voltammogram of hydrogen underpotential deposition. The region for charge determination, between 0.04 and 0.4 V, is marked.

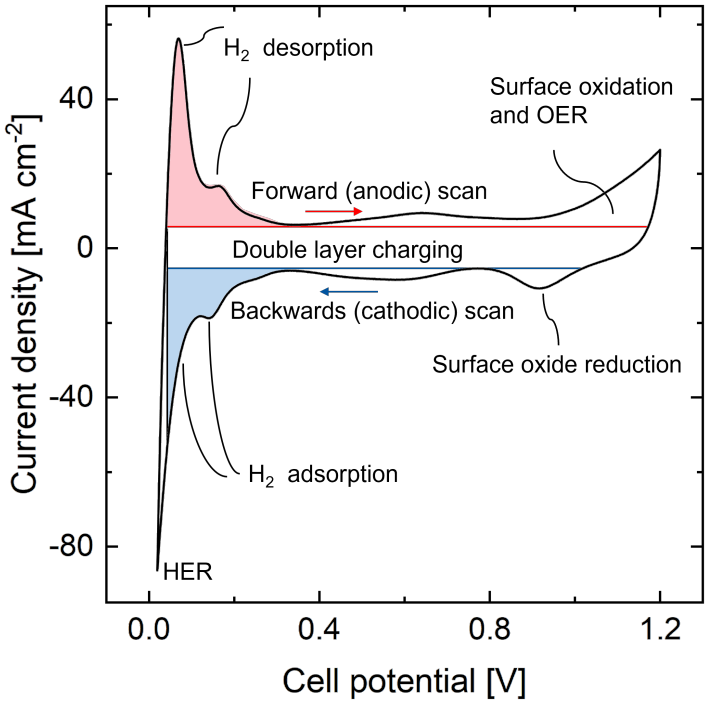

Figure 2.13: Cyclic voltammogram for the determination of the electrochemically active surface area via hydrogen underpotential deposition.

2

3

Performance comparison of low- and high-temperature electrochemical hydrogen compressors

Parts of this chapter have been published as:
Wibke Zängler, Nick Semrau, Matthias Wessling, Robert Keller
Effect of natural gas impurities on electrochemical hydrogen compression and strategies for mitigation, International Journal of Hydrogen Energy, 2025
DOI: 10.1016/j.ijhydene.2025.150980

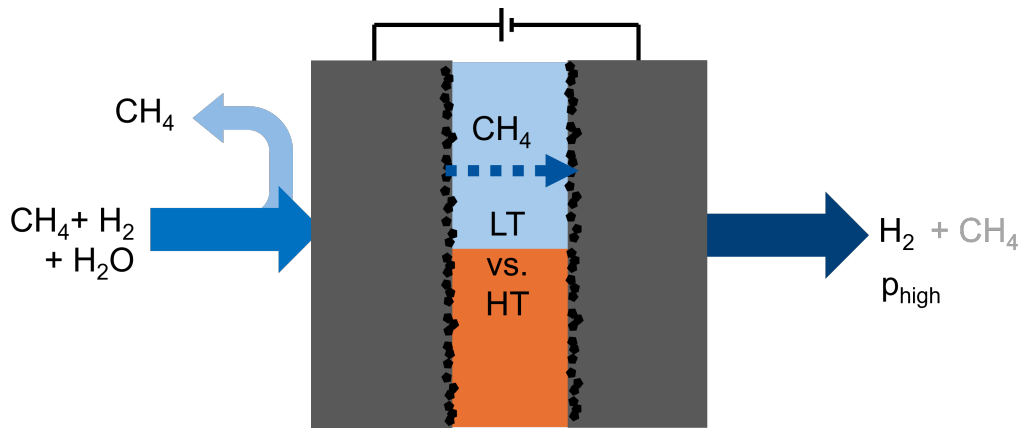

3.1 Introduction

Perfluor sulfonic acid (PFSA)-based electrochemical hydrogen compressors (EHCs) are the most widely researched, but their performance relies on the high relative humidity in the feed gas to maintain the proton conductivity of the membrane (Ch. 2.3.2). This entails the limitation of the process temperature to below 90 °C and complex water management at high relative humidities. Recently, acid-doped polybenzimidazole (PBI)-based EHCs gained increasing interest due to higher operating temperatures enabling operation with feed-impurities and their ability to operate under anhydrous conditions.

Kee et al. [Kee2019] compared polymer- and ceramic-based EHCs efficiency based on thermodynamic analysis. The ceramic-based EHC, operating at temperatures $>$300 °C, could be operated with steam reformates, while polymeric EHCs required pure feed streams. However, the efficiency of the ceramic EHC was lower than the polymeric EHCs because of the power for heating. Aykut et al. [Ayku2024] compared PFSA and PBI-EHC polarization behavior and compression time. They observed lower cell potentials and faster compression at the same cell voltage for the PFSA-EHC. However, they did not provide data on the power requirements of the respective EHCs, leaving the research question regarding the compression efficiency of the different devices open.

Overall, little research has been performed comparing the different types of EHC, thus enabling a comparison of the economic feasibility. For PFSA-based EHCs, water management has been thoroughly investigated; however, for PBI membranes, this aspect remains underexplored on cell level [Pine2022a]. The mechanisms of proton conduction in phosphoric acid-doped PBI membranes are influenced by the degree of acid-doping, operating temperature, and water content within the membrane [Ma2004; Melc2017a]. For use in electrochemical applications, only highly doped PBI membranes are suitable due to the achieved conductivity.

Ma et al. [Ma2004] investigated the impact of water on the performance of high-temperature proton exchange membrane (PEM) fuel cells with a PBI

membrane. They proposed different proton transport mechanisms depending on doping level and water content. Additionally, they state that the proton transfer in acid-doped PBI with water is faster, leading to higher proton conductivities of the same. However, it is important to note that water evolves as a product during fuel cell operation, leading to different humidity conditions compared to EHCs. Perry et al. [Perr2008] investigated the long-term behavior of an HT-EHC when alternating between 0 and 3 % relative humidity. They observed a logarithmic decrease in cell potential of about 15 mV at 200 mAcm^{-2} and 160 °C when they increased the relative humidity and an abrupt increase of cell potential once the humidification was discontinued. Maxwell et al. [Maxw2023] compared the performance of an HT-EHC with 0 and 1.65 % relative humidity and also observed a decrease of 20 mV at 200 mAcm^{-2} and 120 °C.

Despite these insights, there remains a gap in understanding the effects of humidity on high-temperature EHC systems, especially introducing very low relative humidities. For acid-doped PBI membranes, a trade-off exists between acid leaching at high relative humidities, which decreases conductivity over time, and increased conductivity when humidity is introduced into the feed gas [Xu2024]. Consequently, the water supply must be carefully optimized to ensure optimal operation of HT-EHC with acid-doped PBI membranes. Although the conductivity of acid-doped PBI membranes has been a subject of research, there is little exploration within the context of EHC, especially at low relative humidity.

This chapter begins with a thorough comparison of the operational characteristics of PFSA-based and phosphoric acid-doped PBI-based EHCs. This comparison facilitates an analysis of the feasibility of these technologies for practical applications. Thereafter, the effect of dosing low relative humidity on the performance of HT-EHC is evaluated.

3.2 Materials and Methods

30 % hydrogen peroxide was purchased from Sigma-Aldrich Chemie GmbH (GER), and 2.5 mol L^{-1} sulfuric acid was purchased from VWR International (USA). All chemicals were used as received. Ultra-pure water was used with a conductivity of less than 0.05 mS cm^{-1} (Milli-Q® (Merck KGaA, GER)). Nafion™117 was supplied from DuPont de Nemours (USA) with a dry thickness of 180 µm. Gas diffusion electrodes with 0.5 mg cm^{-2} Pt loading on Sigracet 29BC (SGL Carbon SE, GER) carbon paper with a (thickness: 270 µm) and BASF Celtec-P1200W MEA (BASF SE, GER) MEAs with 1 mg cm^{-2} Pt loading on one and 0.7 mg cm^{-2} Pt loading on the other electrode with an active area of 25 cm^2 were acquired from Quintech (GER). The electrode with the 0.7 mg cm^{-2} Pt loading was used as the anode in this study.

3.2.1 Activation protocol for Nafion 117 membranes

To activate the Nafion™117 membranes, the samples are cleaned in H_2O an ultrasonic bath for 20 min to remove any coarse particles. They are then immersed in 3 % H_2O_2 for 1 h at 80 °C to oxidize any organic impurities, followed by 1 h in H_2O to remove residual H_2O_2, oxidation products and hydrate the membrane, and then 1 h in 0.5 mol L^{-1} sulfuric acid to fully protonate all sulfonic acid groups. The membranes are thoroughly rinsed with H_2O between each step. Until further usage, the membranes are stored in H_2O at room temperature.

3.2.2 Low-temperature MEA Preparation

After activation, excess water was removed from the membranes by blow drying. Two 5 x 5 cm GDEs Sigracet 29BC (SGL Carbon SE, GER) were placed on both sides of the membrane, and the assembly was sandwiched between a 1 mm thick PTFE flat sheet and aluminum foil to prevent imprinting during hot pressing. This stack was hot pressed at 130 °C for 2 min and then at room temperature for 1 min with 20 bar hydraulic pressure in a Poly-

stat 300 S2 (Servitec Maschinenbau GmbH, GER) press. The Nafion™ - MEAs were stored at room temperature at 100 % RH until further use.

3.2.3 Test Cell

A Flex-E-Cell (FXC Engineering GmbH, GER) was used as the EHC. Figure 3.1 depicts the cell assembly without backplates and bolts used in the electrochemical experiments. The bipolar plates had a parallel flow channel design with an active area of 25 cm^2. Both the inlet at the top and the outlet at the bottom were equipped with flow dividers to uniformly distribute the gas. For the Nafion™-MEAs, the bipolar plates were made of gold-plated stainless steel (SS), and PBI-MEAs used titanium bipolar plates. The contact pressure was adjusted using Fujifilm Prescale LLW-LW Pressure Indicator Film (FUJIFILM Europe GmbH, GER) pressure indicator film to approximately 2 MPa. The four bolts of the cell were tightened with a torque wrench to 20 N m.

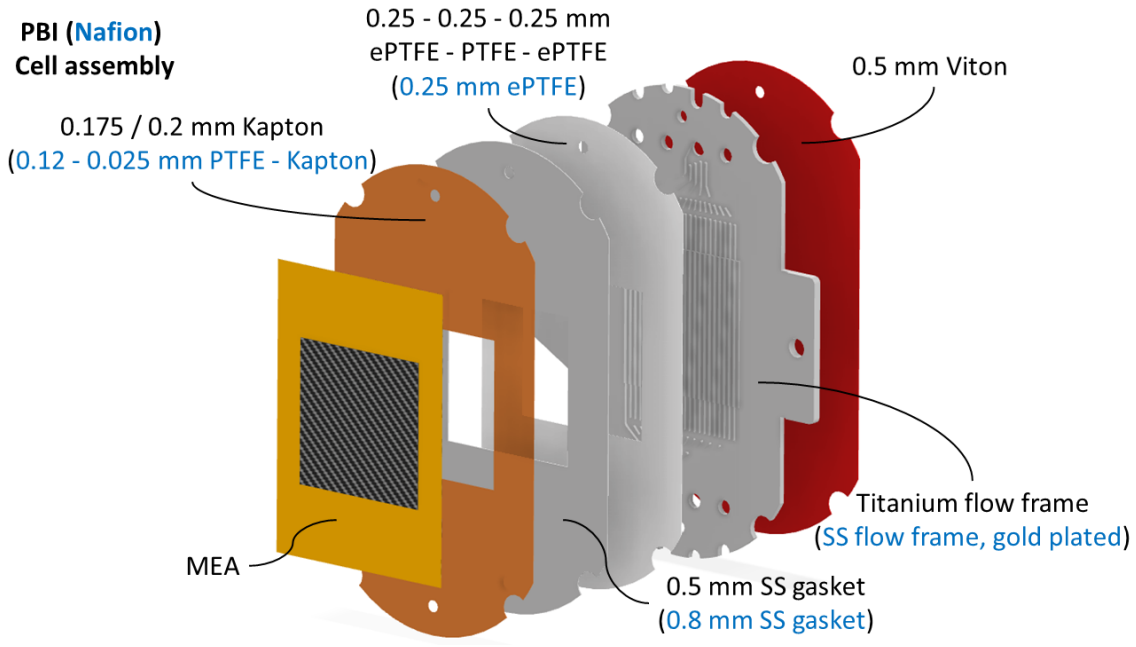

Figure 3.1: Cell assemblies which are used for the electrochemical experiments in the Flex-E-Cell. Differences between the Nafion™MEA assembly and the PBI assembly are highlighted in blue.

3.2.4 Experimental setup

Figure 3.2 shows the flow sheet of the experimental setup used for the electrochemical experiments. Mass flow controllers (Series 35 831MLW, Analyt-MTC, GER) regulated the volumetric flow of all gases supplied to the EHC. The hydrogen supply stochiometry in the manuscript is described by λ, which is defined by the quotient of the supplied amount of H_2 and the theoretical necessary supply of H_2.

$$\lambda = \dot{n}_{\mathrm{H2,in}} / \dot{n}_{\mathrm{H2,theor}} \tag{3.1}$$

The back pressure on the cathode side was regulated by a check spring-loaded back pressure regulator (Swagelok, USA) if required and monitored via a pressure transducer (A-10, WIKA, GER). Gas flowed either through a controlled evaporation mixer (CEM) (CEM Evaporator W-102A, Bronkhorst High-Tech B.V., NL)), a humidification bath, or bypassed the humidifiers to purge the anode and cathode compartments. The humidifier bath was used for humidities below the operation range of the CEM. The humidity, when using the humidification bath, was regulated by mixing the gas exiting the humidifier with dry gas. The CEM, capillaries between CEM and EHC, and the EHC were heated electrically. The capillaries were heated by an HS 450 °C wire heating system and the cell by a 400 W custom-made two plate heating system (HORST GmbH, GER) and controlled by a HT MC11 (HORST GmbH, GER) temperature controller. All heated parts were insulated. Data was collected with echem-Workstation and software (ZUMOlab GmbH, GER).

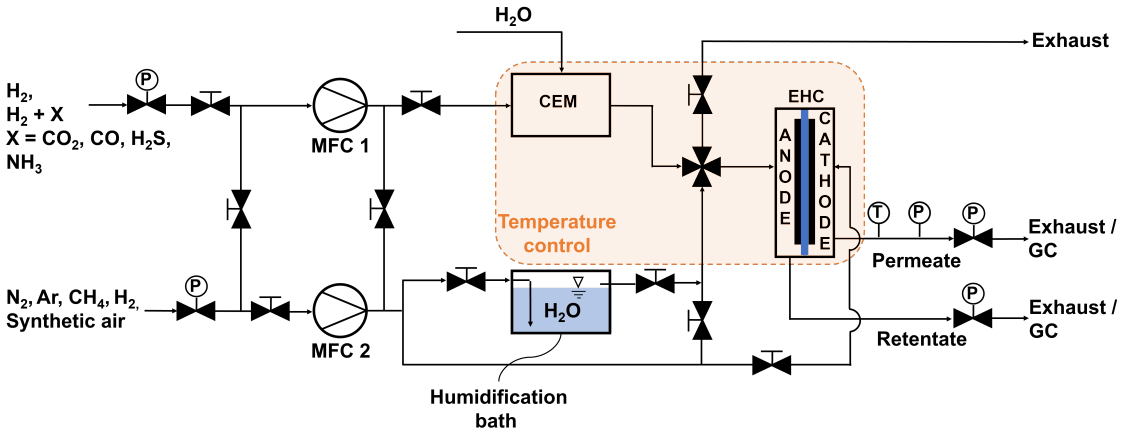

Figure 3.2: Experimental setup for the experiments in Chapter 3 and 4.

3.2.5 Electrochemical experiments and analytics

The electrochemical experiments were performed using a VSP potentiostat with a 20 A VMP3B-20 booster (BioLogic, USA) controlled by the EC-Lab (BioLogic, USA) software. The cell was connected by 4 mm diameter banana plug connectors attached to each bipolar plate in a two-electrode configuration. For experiments above 70 °C, an additional set of high-temperature banana plugs was inserted between the booster and cell. Depending on the current density, these plugs add an additional ohmic resistance of 0.5 to 1 mΩ, which was not corrected in the data analysis. Each MEA was preconditioned when used for the first time according to the protocol in Table 3.1. The protocol for the benchmark characterization is given in Table 3.2.

The current steps for the benchmark characterization were set to 0.25 A and 15 %, 30 %, 45 %, 60 %, 70 %, 80 %, and 90 % of the limiting current. If the current reaches 20 A, 20 A was set instead of 90 % of the current limit, and the steps were adjusted accordingly. Unless otherwise stated, EIS measurements were performed in a frequency range of 100 kHz to 1 mHz with 8 points per decade and an amplitude of 40 % of the DC current or cell potential while taking the average of three measurements per frequency. Electrochemical impedance spectra measurements were conducted at 50 mV and 0.1 A cm^{-2}, respectively.

Table 3.1: Experimental characterization protocol for newly installed MEAs. Nafion-MEAs were preconditioned at 70 °C and 75 % relative humidity. Celtec-MEAs were preconditioned at 145 °C and 0 % relative humidity. CV: Cyclic voltammetry; OCV: Open circuit voltage; CA: Chronoamperometry; LSV: Linear sweep voltammetry; PEIS: potentiostatic electrochemical impedance spectroscopy; CP: Chronopotentiometry.

Index	Technique	Settings	Duration
1	OCV		30 s
2	CA	10 mV	10 min
3	CA	50 mV	10 min
4	PEIS		
5	CA	100 mV	10 min
6	OCV		5 min
7	LSV	2 mV s^{-1}	
8	CA	End of LSV	1 min
9	OCV		5 min
10	LSV	2 mV s^{-1}	
11	CA	End of LSV	1 min
13	OCV		5 min
14	LSV	2 mV s^{-1}	
15	CA	End of LSV	1 min
16	OCV		5 min
17	CA	10 mV	5 min
18	CA	50 mV	5 min
19	PEIS		
20	CA	100 mV	5 min
(21)	(CP)	(10 A)	(at least 2 h)

Table 3.2: Experimental protocol for the electrochemical characterization of the MEAs. OCV: Open circuit voltage; CA: Chronoamperometry; LSV: Linear sweep voltammetry; PEIS: potentiostatic electrochemical impedance spectroscopy; CP: Chronopotentiometry; PC: Polarization curve.

Index	Group	Technique	Settings	Duration
1	Prerun	OCV		30 s
2	Prerun	CA 0	50 mV	15 to 45 min
3	Prerun	LSV	2 mV s^{-1}	
4	Prerun	CA 1	50 mV	15 min
5	Prerun	PEIS 1		
6	Step 1 (PC1)	OCV		30 s
7	Step 1 (PC1)	CP 1-1	0.25 A	5 min
8	Step 1 (PC1)	CP 1-2	15 % of I_{limit}	10 min
9	Step 1 (PC1)	CP 1-3	30 % of I_{limit}	10 min
10	Step 1 (PC1)	CP 1-4	45 % of I_{limit}	10 min
11	Step 1 (PC1)	CP 1-5	60 % of I_{limit}	10 min
12	Step 1 (PC1)	CP 1-6	70 % of I_{limit}	10 min
13	Step 1 (PC1)	CP 1-7	80 % of I_{limit}	10 min
14	Step 1 (PC1)	CP 1-8	90 % of I_{limit}	10 min
15	Recovery 1	OCV		30 s
16	Recovery 1	CA 2	50 mV	15 min
17	Recovery 1	PEIS 2		
18	Step 2 (PC2)	OCV		30 s
22	Step 2 (PC2)	CP 2-1	0.25 A	5 min
23	Step 2 (PC2)	CP 2-2	15 % of I_{limit}	10 min
24	Step 2 (PC2)	CP 2-3	30 % of I_{limit}	10 min
25	Step 2 (PC2)	CP 2-4	45 % of I_{limit}	10 min
26	Step 2 (PC2)	CP 2-5	60 % of I_{limit}	10 min
27	Step 2 (PC2)	CP 2-6	70 % of I_{limit}	10 min
28	Step 2 (PC2)	CP 2-7	80 % of I_{limit}	10 min
29	Step 2 (PC2)	CP 2-8	90 % of I_{limit}	10 min
30	Recovery 2	OCV		
31	Recovery 2	CA 3	50 mV	15 min
32	Recovery 2	PEIS 3		

In the LSV measurements, the potential is swept at 2 mV s^{-1} to a maximum potential of 500 to 750 mV starting from 0 V against the reference electrode. Gas compositions were obtained by gas chromatography with an Agilent 8860 GC System (Agilent Technologies, Inc, USA). The carrier gas was helium at a flow rate of 5.7 mL min^{-1}. The fuel gas stream was composed of 350 mL min^{-1} synthetic air and 35 mL min^{-1} H_2. A molecular sieve column 5A 80/100 mesh (Agilent Technologies, USA), a Haysep Q Micro column HysepQ 80/100 mesh (Agilent Technologies, USA), and a PoraBOND Q column (Agilent Technologies, USA) were installed as separation columns.

3.2.6 Efficiency

The energy efficiency of the EHC was calculated by dividing the output energy as the energy content of the product gas minus the energy consumed by the EHC by the energy content of the H_2 input and energy for heating ($\dot{Q}_{Heat}$) assuming the availability of waste heat [Maxw2023]. The energy content of H_2 was calculated using the higher heating value (HHV). The electric power (P_{el}) of the heating unit is given in Table 3.3.

$$\eta_{E,Energy} = \frac{\dot{n}_{H2} \cdot HHV_{H2} - E_{cell} \cdot j \cdot A}{\dot{n}_{H2} \cdot HHV_{H2} + \dot{Q}_{Heat}} \tag{3.2}$$

The energy required for heating, assuming a waste heat source, was calculated based on the electrical heating power measured in the test stand [Maxw2023].

$$\dot{Q}_{Heat} = P_{el} \cdot (1 - T_U / T_{EHC}) \tag{3.3}$$

Assuming 100 % faradaic efficiency and neglecting λ and $\dot{Q}_{Heat}$ the generalized ideal definition of the voltage efficiency is derived as in Equation 3.4, where 1.483 V results from the division of HHV_{H2} by $2F$:

$$\eta_{E,Voltage,ideal} = 1 - \frac{E_{cell}}{1.483[V]} \tag{3.4}$$

Table 3.3: Total electrical power consumption of the heating plates of the EHC.

Operating temperature in °C	P_{el} in W
70	11.2
120	31.2
160	53.4

3.3 Results

3.3.1 Benchmark characterization

A low-temperature EHC with Nafion 117-MEA (Nafion-EHC) and a high-temperature EHC with Celtec-P1200W MEA (Celtec-EHC) were characterized with pure H_2 to establish a benchmark for the poisoning investigations in Chapter 4. The current density of the Nafion-EHC at 50 mV in Figure 3.3 (a) rises with increasing temperature from 20 to 70 °C while the high-frequency resistance (HFR) decreases. The achieved current is in good agreement with literature using the same membrane [Grig2011; Bori2023]. For the Celtec-EHC with dry feed gas (Fig. 3.3 (a)), the current density increases from almost zero at 20 °C, with increasing slope until 120 °C, where it reaches similar values to the Nafion-EHC and no significant increase in current is observed when increasing the temperature further 120 °C. The HFR of the Celtec-EHC decreases steeply until 70 °C. This behavior is also reported by the manufacturer data. When increasing the feed gas relative humidity, the achieved current density rises by 90 mA cm^{-2}.

The dry Celtec and Nafion-EHC show a linear iV-relation until 600 mA cm^{-2}, with similar performance, as shown in Figure 3.3 (b). At current densities above 600 mA cm^{-2}, the Nafion-EHC shows non-linear behavior, which is more pronounced when iR-corrected and could be attributed to water mass transport limitations leading to drying [Pine2022a]. The humidified Celtec-EHC achieved an about 30 % lower cell potential than in dry operation, and a linear iV-relation is observed for the investigated current range. This improvement in cell potential can be attributed to an increased proton conductivity of the PEM, caused by phosphoric acid dissociation induced by the water [Melc2017a]. Additionally, the increased humidity improved the stability of the operation of the MEA, presumably by suppressing the hydrolysis of phosphoric acid at high temperatures [Ma2004]. In the dry operation of the Celtec-EHC at constant current, shown in Figure 3.4, a potential increase over time was observed, which was more pronounced at increased temperatures. For the Celtec-EHC, the iR-corrected polarization curves at 0 % and 10 % RH is close to 0 mV, indicating mostly iR-losses in

the cell.

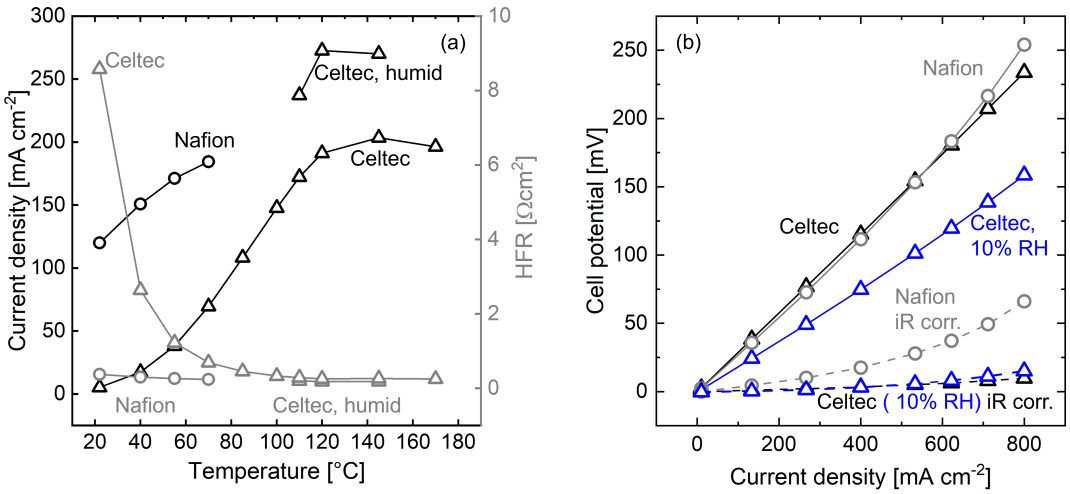

Figure 3.3: (a) Average current density at 50 mV (black) and high-frequency resistance (HFR, grey) of EHC with Nafion™117 at 100 % RH (circles) and CELTEC MEA dry and CELTEC MEA humid with 2.4 g h^{-1} water in the 200 mL min^{-1} feed gas (Triangles); (b) Polarization curve from current steps of EHC with Nafion™117 (circles, grey) at 100 % RH and 70 °C and Celtec MEA at 0 % (black) and 10 % (blue) RH and 120 °C.

3.3.2 Impact of relative humidity on PBI-EHC

An increase in potential over time was observed during the dry operation of the Celtec-EHC in the benchmark experiments and in Figure 3.4 (a), while a stabilized cell potential was observed when H_2O was added to the feed gas. However, excessive H_2O supply to the cell can lead to acid leaching, leading to MEA-degradation by reduced membrane conductivity. Additionally, low relative humidity is beneficial for the process simplicity and, thus, reduces process cost. At 120 °C the potential increase rate was 1 µV s^{-1} for the last 30 min before the switch to humidified conditions, after 2 h. At 160 °C the increase rate was 2 to 3 µV s^{-1} (Fig. 3.4 (a)). The increase in cell potential can be explained by dimerisation of H_3PO_4 leading to pyrophosphoric acid formation during dry operation at about 130 °C or above, reducing the membrane conductivity due to the lower conductivity of pyrophosphoric acid [Ma2004].

In addition to the stabilization, the cell potential decreased upon the intro-

duction of H_2O to the feed gas (Fig. 3.4 (a)). The decrease in cell potential can be explained by faster proton transport in highly H_3PO_4-doped PBI-membranes with H_2O leading to an increased conductivity [Ma2004] (Ch. 2.3.2). Additionally, at increased relative humidity less H_3PO_4 dehydration will occur mitigating conductivity losses due to H_3PO_4 dimerization. After the switch to a humidified feed gas, the cell potential stabilizes after 30 min for 0.67 % relative humidity and after approximately 90 min for the lower relative humidities. With increasing relative humidity, the cell potential Perry et al. [Perr2008] also observed a decrease in cell potential when switching from 0 to 3 % relative humidity.

In Figure 3.4 (b), an exponential decrease in cell potential with increasing relative humidity can be observed. The potential decreases by 30 % when increasing the relative humidity of the feed from 0 to 0.67 % at 120 °C, while the potential drops by 6 % when increasing the relative humidity from 0.67 to 3 %. Consequently, introducing very low relative humidities significantly improve the cell performance, while increasing the relative humidity of the feed to above 1 % yields slight improvement.

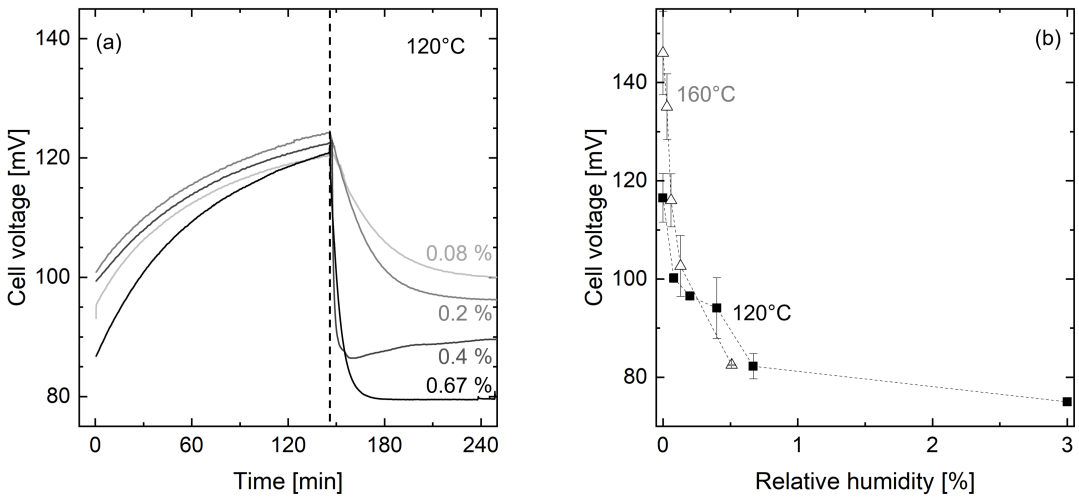

Figure 3.4: (a) Cell potential over time of a Celtec-EHC at 400 mA cm^{-2}, until 145 min: 0 % RH, after 145 min: change to displayed relative humidity, 120 °C, between the experiments the cell was flushed with dry Ar for min. 12 h; (b) Cell voltage at 400 mA cm^{-2} over relative humidity of the hydrogen feed gas.

The polarization behavior, shown in Figure 3.5, is linear at all humidities at 120 °C and a decrease in cell potential with increasing relative humidity was

measured. The HFR of the impedance spectra, shown in Figure 3.6 (a), also decreases with increasing relative humidity, confirming that the decrease in cell potential with increasing relative humidity (Fig. 3.4) can be attributed to an increased membrane conductivity. At 160 °C, a non linear increase of the cell potential at current densities above 400 mAcm^{-2} was observed. According to Arrhenius law, a decrease in cell potential would be expected at increased operating temperatures due to a decrease in membrane conductivity [Ma2004]. However, at current densities above 400 mAcm^{-2} higher cell potentials were measured at 160 °C compared to 120 °C. The HFR (Fig. 3.6 (b)) during dry operation is about 0.1 Ω cm^2 higher at 160 °C, which justifies a 80 mV increase in cell potential at 800 mAcm^{-2}.

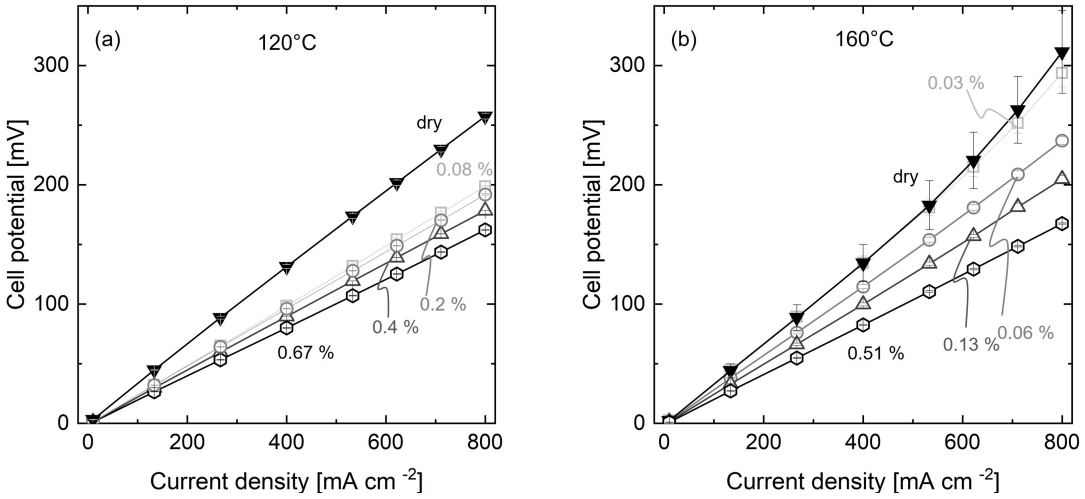

Figure 3.5: Polarization curves of a Celtec-EHC at (a) 120 °C and (b) 160 °C at varied relative humidities displayed in percent.

The increased cell potential may be caused by reinforced H_3PO_4 dehydration at higher temperatures, leading to decreased membrane conductivity counteracting the conductivity increase by temperature. Additionally, the ion transport at the catalyst/membrane interface might be disrupted because H_3PO_4 is also used as an ionomer in the catalyst layer of the Celtec-MEA. The impedance spectra at 160 °C (Fig. 3.6 (b)) shows increased charge transfer resistances compared to 120 °C, especially at very low relative humidities, supporting the previous hypothesis and causing the non-linear polarization behavior [Male2009].

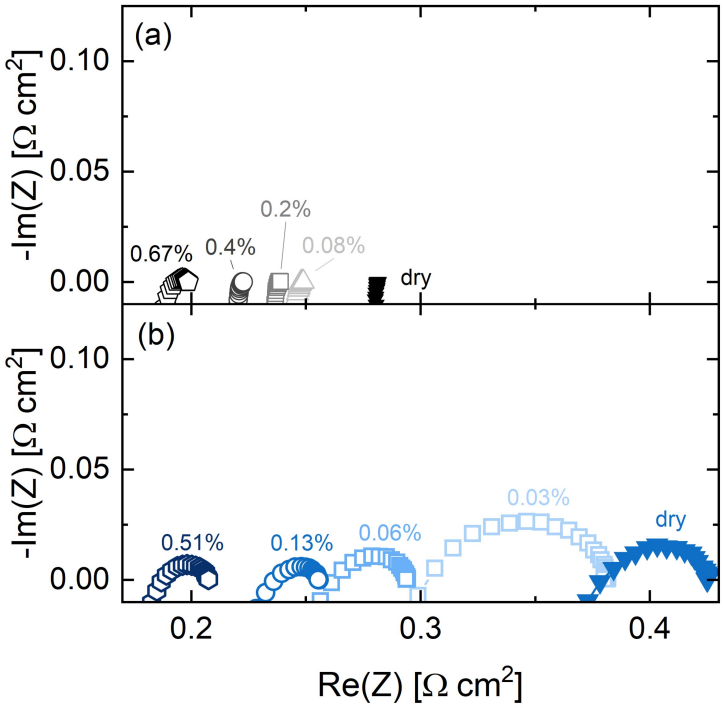

Figure 3.6: Electrochemical impedance spectra (a) 120 °C and (b) 160 °C at varied relative humidities displayed in percent.

3.3.3 Hydrogen compression and purification

Compression of pure H_2 was investigated up to a cathode pressure of 6 bar, as shown in Figure 3.7. The graph displays the cell potential, the iR-corrected cell potential, and the compression efficiency, which is calculated by dividing the Nernst potential by the measured potential at various cathode pressures. As expected from the Nernst equation, the cell potential increases logarithmically with increasing cathode pressure. The compression efficiency of the Celtec-EHC was generally higher compared to the Nafion-EHC. At a cathode pressure of 6 bar, the compression efficiency was slightly above 40 % for the Celtec and 30 % for the Nafion-EHC. The higher compression efficiency of the Celtec-EHC can be attributed to the lower cell potentials achieved.

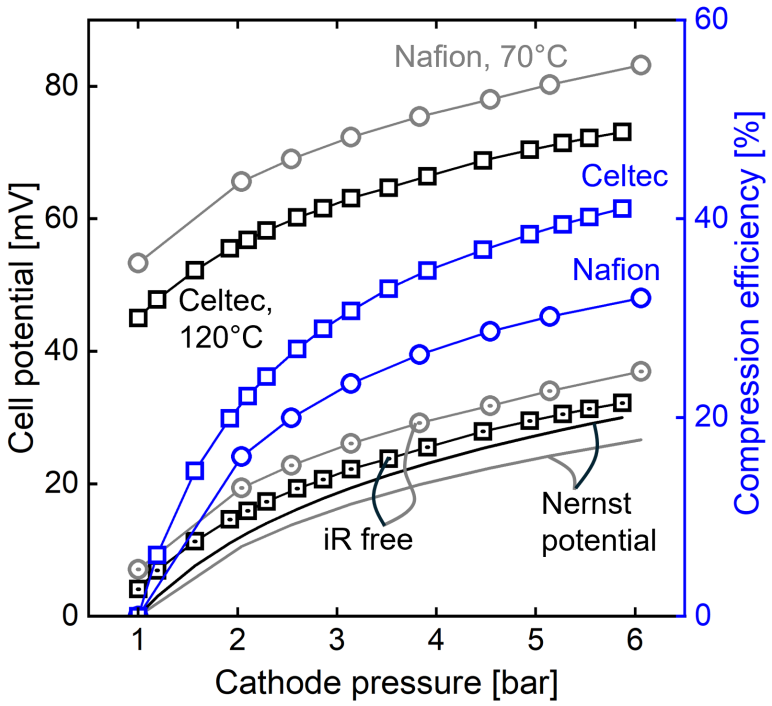

Figure 3.7: Cell potential and compression efficiency at different cathode pressures.

The purification of H_2 from 50/50 and 80/20 CH_4/H_2 mixtures was investigated. The CH_4 content in the product gas, shown in Figure 3.8, is higher with increasing CH_4 feed content and decreasing current density. With higher CH_4 share in the feed, the partial pressure difference and thus the driving force for CH_4 gas permeation increases, leading to a higher diffusion rate. While this phenomenon is independent of current density, H_2 evolution naturally is not. Thus, high current densities favor high purities. The CH_4 content in the product gas is one order of magnitude higher for the Nafion-EHC, indicating a higher gas permeability of the Nafion™membrane. For example, the H_2 permeability is one order of magnitude larger for Nafion™117 with $5 \cdot 10^{-11}$molcm^{-1}s^{-1}bar^{-1} at 70 °C [Scha2015] than for H_3PO_4-doped PBI with $7.7 \cdot 10^{-12}$molcm^{-1}s^{-1}bar^{-1} at 160 °C [Chen2022]. When increasing the operating temperature of the Celtec-EHC from 120 to 160 °C, the CH_4 content increases, which can be explained by increased gas permeability at higher temperatures due to increased diffusivity [He2006].

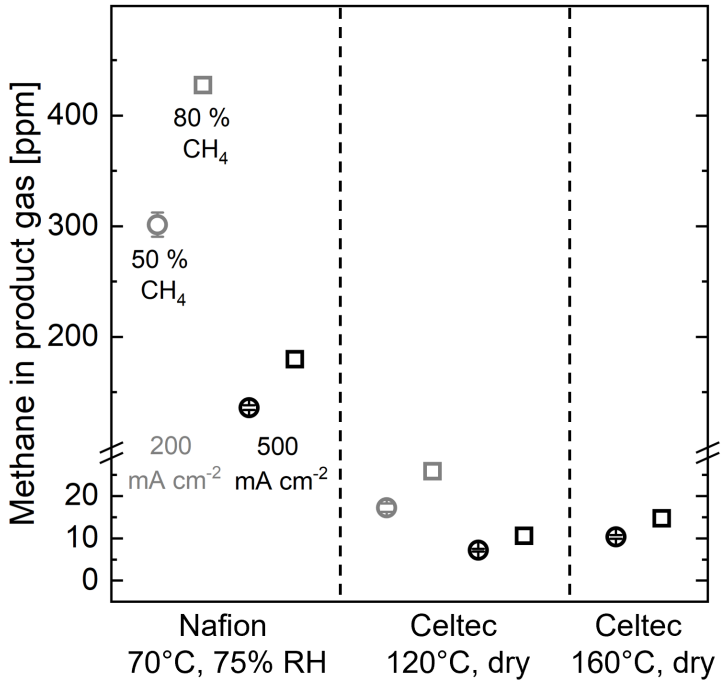

Figure 3.8: Purity of H_2 when separated from H_2/CH_4 mixtures.

Linear sweep analysis was performed with both EHCs to elucidate mass transfer effects and determine optimum operation conditions, when operating with gas mixtures. As a reference, a linear sweep voltammogramm with pure H_2 and a minimum λ of 1.32 at 800 mAcm^{-2} is displayed (Fig. 3.9, blue line). At current densities toward 0 mAcm^{-2}, an increase in cell potential with lower H_2-share in the feed according to the Nernst potential is apparent. For both H_2/CH_4 mixtures the cell potential increases exponentially, when approaching the respective maximum current density due to mass transport limitations leading to fuel starvation of the catalyst. The exponential increase is more pronounced for the Nafion-EHC, which might be due to additional mass transfer resistances posed by the ionomer, the higher water activity and/or slower diffusion at lower temperatures. At 60 mL min^{-1} H_2 flow rate, the theoretical maximum current density, corresponding to a hydrogen recovery of 100 %, was achieved by both EHC-configurations. However, the voltage efficency for the Nafion-EHC is lower due to the higher cell potential. At 150 mL min^{-1} H_2 flow rate 95 % and 91 % recovery were achieved with the Nafion-EHC for 50/50 and 20/80 H_2/CH_4, respectively.

In the Celtec-EHC, 100 % and 96 % recovery were achieved for 50/50 and 20/80 H_2/CH_4, respectively. The lower recoveries at higher H_2 flow rates may be attributed to lower residency times leading to bulk diffusion limitation of H_2. The higher theoretical maximum current density will additionally lead to more concentration polarization resulting in diffusing limitation and consequently an increase in cell potential due to H_2 starvation of the catalyst. The highest energy efficiency for 60 mL min^{-1} H_2 feed was achieved at λ = 1.1 and 1.8 for the Nafion-EHC and λ = 1 and 1.03 for the Celtec-EHC with 50/50 and 20/80 H_2/CH_4 feed composition, respectively. At 150 mL min^{-1} the highest efficiency was achieved at λ = 1.96 and 1.98 for the Nafion-EHC and λ = 1.18 and 1.3 for the Celtec-EHC with 50/50 and 20/80 H_2/CH_4 feed composition, respectively. Overall, in the Celtec-EHC higher recoveries can be achieved and lower optimal λ were identified. The voltage efficiency of the Celtec-EHC is higher compared to the Nafion-EHC due to the lower cell potentials. However, the energy efficiency of the Celtec-EHC is lower, due to the higher power demand for heating at 120 °C.

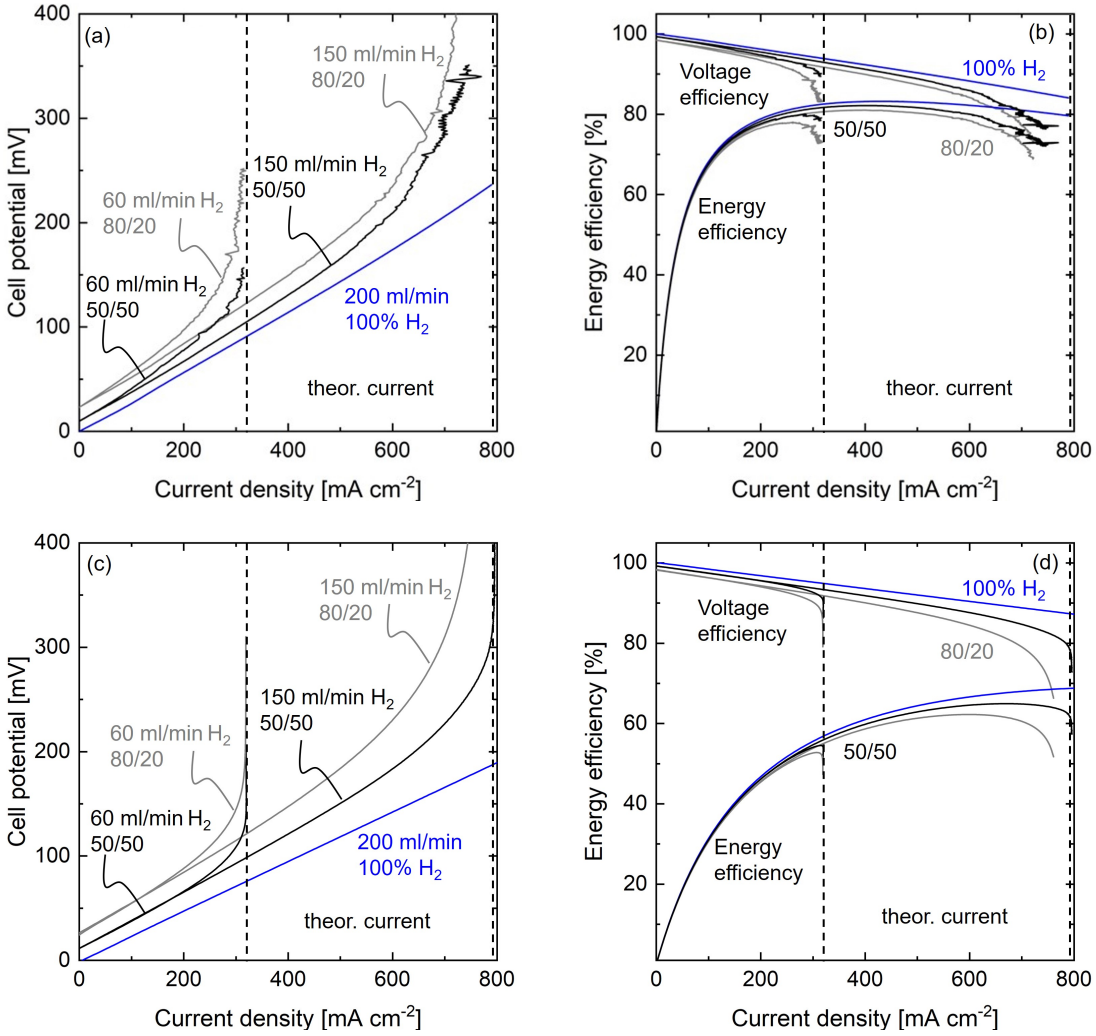

Figure 3.9: (a) Mean value of three linear sweep voltammogramms of a Nafion-EHC at 70 °C and 100 % RH, blue: pure hydrogen at 200 mL min^{-1}, grey: binary mixture of 80 % methane and 20 % hydrogen with 60 mL min^{-1} and 150 mL min^{-1} hydrogen flow rate, black: binary mixture of 50 % methane and 50 % hydrogen with 60 mL min^{-1} and 150 mL min^{-1} hydrogen flow rate, dashed line indicates the theoretical maximal current density at the respective flow rate, (b) Corresponding voltage efficiency and energy efficiency, (c) Mean value of three linear sweep voltammogramms of a Celtec-EHC at 120 °C and 0 % RH, blue: pure hydrogen at 200 mL min^{-1}, grey: binary mixture of 80 % methane and 20 % hydrogen with 60 mL min^{-1} and 150 mL min^{-1} hydrogen flow rate, black: binary mixture of 50 % methane and 50 % hydrogen with 60 mL min^{-1} and 150 mL min^{-1} hydrogen flow rate, dashed line indicates the theoretical maximal current density at the respective flow rate (d) Corresponding voltage efficiency and energy efficiency.

3.4 Conclusion

In this study, we provided a comparison of PFSA- and PBI based EHC operation parameter, polarization behavior and compression and separation efficiency. Additionally, the impact of relative humidity on PBI-based EHCs performance was discussed.

The performance of the PFSA-EHC at 70 °C and 75 % relative humidity, and the PBI-EHC at 120 °C in dry conditions was found to be comparable. However, the analysis revealed that for the PBI-EHC, internal resistance (iR) losses were primarily responsible for performance limitations, while the PFSA-EHC exhibited non-linear polarization behavior indicative of mass transport limitations. Notably, an increase in relative humidity resulted in a significant decrease in cell potential for the PBI-EHC. During dry operation of the PBI-EHC an increase in cell potential (1 to 3 $\mu V\,s^{-1}$) was observed, which was more pronounced at elevated temperatures. The increase in cell potential is attributed to phosphoric acid dehydration, leading to a reduced membrane conductivity and, thus, an increase in cell potential. Increasing the relative humidity if the PBI-EHC feed from dry conditions to very low levels ($<$0.7 %) results in a 30 % decrease in cell potential. A further increase in humidity to 3 % yields only a modest 6 % in cell potential, suggesting a diminishing return effect at higher humidity levels. While these findings emphasize the need for careful humidity management to optimize PBI-EHC performance, it is crucial to explore the influence of varying humidity on acid leaching in future studies.

Compression to 6 bar was achieved for both EHCs, with the PFSA-EHC demonstrating a compression efficiency of 30 %, while the PBI-EHC achieved a higher efficiency of 40 %. The increased compression efficiency of the PBI-EHC can be attributed to its lower cell potential. However, it is important to note that hydrogen was only compressed to 6 bar in this study. Future research should focus on evaluating higher compression ratios to better understand the effects of back permeation and to investigate the mechanical stability of the PBI-EHC under increased operational pressures.

When separating H_2 from H_2/CH_4 mixtures, the PFSA-EHC did not meet

fuel cell grade requirements. In contrast, CH_4 concentrations below 30 ppm were achieved with the PBI-EHC, depending on the current density and mixture composition.

In summary, the comparison of PFSA- and PBI-based electrochemical hydrogen compressors enables a critical evaluation of the process feasibility. The findings related to humidification and product gas purity provide insights into the necessary balance-of-plant components in a hydrogen compression system, thus paving the way for a comparative techno-economic assessment of these technologies.

4

Impact of Natural Gas Impurities and Effective Mitigation Strategies in Electrochemical Hydrogen Compression

Parts of this chapter have been published as:
Wibke Zängler, Nick Semrau, Matthias Wessling, Robert Keller
Effect of natural gas impurities on electrochemical hydrogen compression and strategies for mitigation, International Journal of Hydrogen Energy, 2025
DOI: 10.1016/j.ijhydene.2025.150980

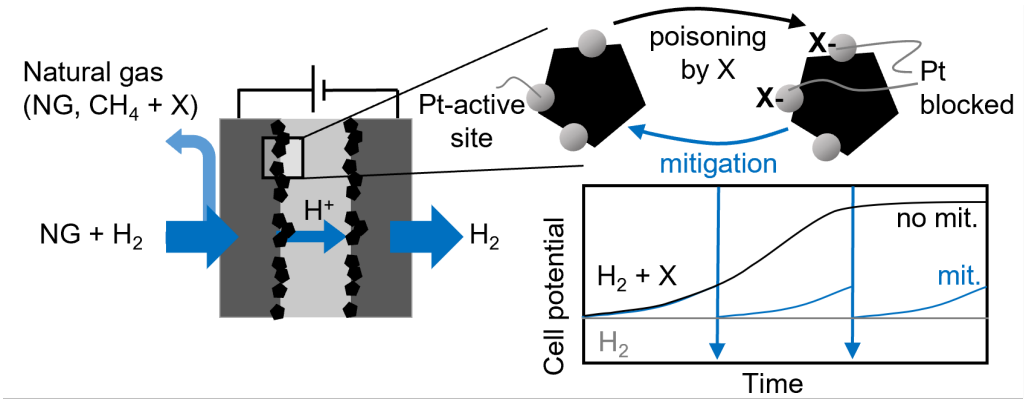

4.1 Introduction

Until 2030, several EU countries want to leverage H_2 admixing to the natural gas grid for H_2 distribution as an interim step for decarbonization [Pawe2020; Kane2022]. Distributing H_2 via blending into the existing natural gas grid could reduce the cost of transportation in the mid-term future and facilitate H_2 supply to remote locations [Maha2022]. Moreover, it would enable H_2 injection into the natural gas during off-peak hours. At the point of use, separation and compression technology is needed for local withdrawal of H_2. State-of-the-art technologies for H_2 separation are pressure-driven membranes for moderate purity combined with pressure swing adsorption (PSA) for high purities above 98 %. In PSA, multiple adsorption columns packed with adsorbent are employed [Relv2018]. PSA units are usually operated on a large scale and are economically less attractive for small-scale H_2 separation [Nord2021]. The size of the PSA plant increases with lower H_2 concentrations in the feed gas stream [Mela2013]. Moreover, H_2 recovery rates for small-scale PSA are low ($<$75 %) [Relv2018], and additional compression capacity is needed. A promising technology, especially for distributed H_2 withdrawal, is electrochemical hydrogen compression.

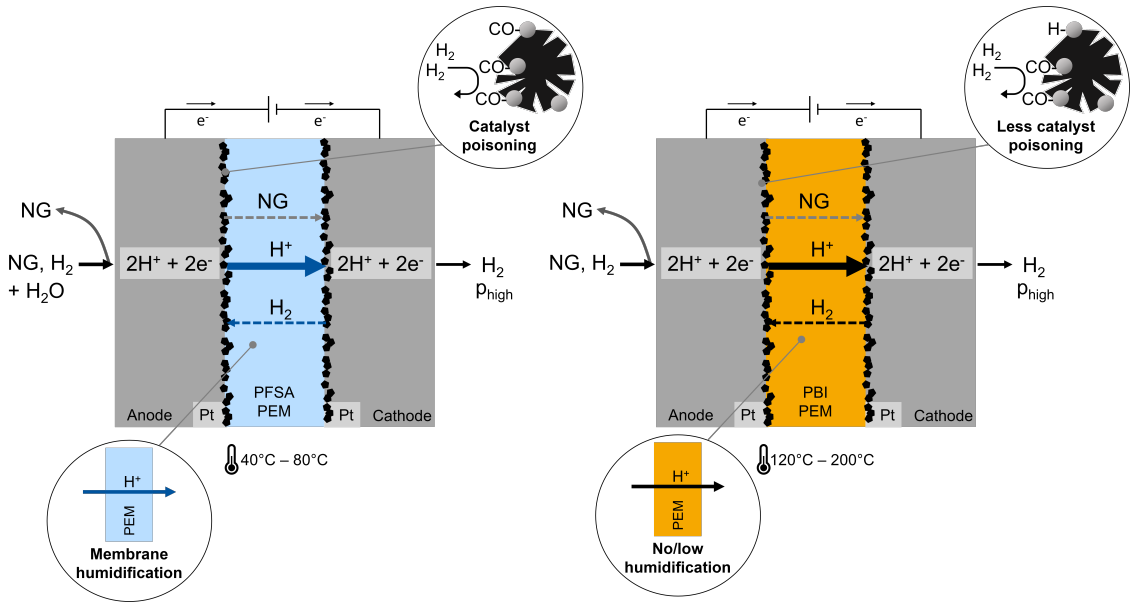

Figure 4.1: Challenges in low- and high-temperature electrochemical hydrogen compression.

EHC offers high recovery rates and H_2 purity in a single step while maintaining high efficiency, also in small-scale operation [Nord2019; Mrus2024]. Additionally, EHC combines H_2 compression and separation in one unit operation, being a key advantage for application with impure H_2 or gas mixtures such as blended natural gas [Durm2021].

The main challenges for implementing the EHC in the natural gas grid are proper humidification of the mostly perfluorinated sulfonic acid (PFSA)-based proton exchange membranes (PEMs), high product gas purity, and stable performance even with detrimental gas impurities in the natural gas [Zou2020]. When applied in gas mixtures containing catalyst poisons, poisoning, especially of the anode catalyst, reduces the EHC's performance. Natural gas mainly consists of methane, propane, butane, carbon dioxide, and oxygen. Additionally, the trace impurities H_2S, CO, COS, mercaptan, silicon compounds, amines, and NH_3 are present, which are among the more critical species for the EHC [Trég2020].

Table 4.1: Upper limits of contaminants investigated in this study in the German natural gas grid according to DVGW e.V. technical rule G 260 [DVGW2021].

Species	Unit	Limit
CO_2	vol%	4
CO	ppm	100
H_2S	ppm	3.5
NH_3	ppm	14

CO competes with H_2 adsorption and blocks active sites of the platinum catalyst [Vald2020]. Adsorption of CO on Pt:

$$Pt\cdot + CO \longrightarrow Pt{-}CO \tag{4.1}$$

Nordio et al. [Nord2020] demonstrated that catalyst inhibition from CO_2 is mainly due to reverse water gas shift reaction (Eqn. 4.2) forming CO. Additionally, CO_2 permeating through the membrane can be electrochemically

reduced at the cathode of the EHC (4.3).

$$CO_2 + H_2 \rightleftharpoons CO + H_2O \tag{4.2}$$

$$Pt{-}CO_{2ads} + 2\,H^+ + 2\,e^- \longleftrightarrow Pt{-}CO_{ads} + H_2O \tag{4.3}$$

H_2S also competes with H_2 for adsorption on Pt (Eqn. 4.4). Additionally, H_2S dissociates chemically and electrochemically to adsorbed sulfur, forming H_2 (Eqn.4.5, 4.6). The complex reaction pathways following H_2S adsorption on platinum can be found in [Seth2010; Dong2022; Faro1977].

$$Pt\cdot + H_2S \rightleftharpoons Pt{-}H_2S_{ads} \tag{4.4}$$

$$Pt{-}H_2S_{ads} \rightleftharpoons Pt{-}S + H_2 \tag{4.5}$$

$$Pt{-}H_2S_{ads} \longrightarrow Pt{-}S + 2\,H^+ + 2\,e^-,\ E^0 = 0.165V \tag{4.6}$$

Contrary to the other listed poisons, NH_3 mainly interacts with the membrane, ionomer, and protons formed in the EHC, reducing the proton conductivity and performance [Gome2018; Verm2021b; Hals2006].

$$NH_3 + H^+ \longrightarrow NH_4^+ \tag{4.7}$$

For high-temperature, H_3PO_4-doped polybenzimidazole (PBI) based MEAs, the NH_3 reacts with the acidic groups in the membrane, reducing its conductivity. Additionally, ammonium phosphate salt may be formed, leading to reduced protonic activity and mechanical degradation of the membrane [Isor2019; Scho2021].

$$NH_3 + H_3PO_4 \rightleftharpoons H_2PO_4^- + NH_4^+ \tag{4.8}$$

For low-temperature, PFSA-based MEAs, NH_3 can lead to reduced conduc-

tivity of membrane and ionomer by substitution of H^+ with NH_4^+, resulting in the ammonium-form of Nafion™, which can be detrimental at high current densities [Gome2018; Urib2002].

$$NH_3 + -SO^- + H_3O^+ \longrightarrow -SO^- + NH_4^+ + H_2O \tag{4.9}$$

Although CH_4 is considered mostly inert, CH_4 oxidation may occur at the anode of the EHC [Jack2020].

$$CH_4 + H_2O \rightleftharpoons CO_2 + 8\,H^+ + 8\,e^-,\ E^0 = 0.169V \tag{4.10}$$

Table 4.2 summarizes studies on H_2/CH_4, H_2/natural gas mixtures, and studies of the effect of contaminants in the feed of the EHC. Nordio et al. [Nord2020] tested the effect of CO_2 on the EHC and found catalyst inhibition through adsorbed CO from reverse water gas shift. They showed that flushing with air, a so-called air bleed, can quickly recover the inhibited catalyst. Jackson et al. [Jack2020] investigated the effect of CO and H_2S on the low-temperature EHC performance and introduced oxygen and ozone dosing as poison mitigation strategies, which oxidize the adsorbed contaminants. After poisoning with 5 ppm H_2S, they achieved up to 98 % recovery of the current density after 20 min ozone cleaning at open circuit potential. In their follow-up study, Jackson et al. [Jack2023] fed H_2/CH_4 and H_2/natural gas mixtures to a low-temperature EHC. Even when adding oxidants, they could not achieve stable operation with the H_2/natural gas mixtures. Moreover, the measured product gas purity with H_2/natural gas feed did not reach the ISO 14687-2019-D standard for fuel cells [Inte2024]. Mrusek et al. [Mrus2024] investigated H_2 withdrawal from CH_4/H_2 mixtures in a low-temperature EHC and detected a CH_4 content of 300 ppm in the product gas. Moreover, they investigated the impact of the typically used odorant (THT) on the EHC performance and observed catalyst poisoning by this sulfur compound.

To overcome the aforementioned challenges commonly experienced in low-temperature EHCs, high-temperature EHCs have gained research interest. High-temperature EHCs offer a higher tolerance to impurities, improved

kinetics and mass transport, and sustainability due to the use of PFAS-free membranes [Perr2008]. Additionally, they can operate under anhydrous conditions, enabling more facile process operation [Lim2023]. The study of Vermaak et al. [Verm2021a] presents the separation of H_2 from CH_4/H_2, CO_2/H_2 and NH_3/H_2 mixtures. They employed a phosphoric acid doped pyridine-based aromatic polyether PEM in a high-temperature EHC. During operation with CO_2/H_2 mixtures, a severe decrease in polarization performance was observed due to CO adsorption on the catalyst. When introducing 1500 ppm NH_3 to the EHC, the performance was strongly reduced and broke down entirely due to membrane failure with 3000 ppm NH_3. Maxwell et al. [Maxw2023] introduced CO_2/H_2 mixtures to a high-temperature EHC with a PBI-based PEM. They observed improved polarization performance when operating the EHC at low relative humidity compared to dry operation. Moreover, the current efficiency did not decrease significantly with up to 80 vol% CO_2 in the feed when operating at 120 °C. Moreover, they identified heating as the main contributor to the EHC's energy demand and showed that waste heat utilization can significantly increase the system's energy efficiency. Arunagiri et al. [Arun2024] investigated H_2 withdrawal from natural gas containing 10 % H_2 using a high-temperature PEM and binder and observed a degradation rate of 44 µV h^{-1} in a 100 h test. However, their gas did not contain H_2S or CO, which are expected to be among the most critical impurities in the natural gas grid [Arun2024; Trég2020].

Until now, no study has systematically compared the performance of low- and high-temperature EHCs when operating with trace impurities present in natural gas, thereby enabling a critical review of which technology is most suitable for the application. Additionally, poison mitigation strategies, apart from dosing oxidants, which can cause PEM degradation by H_2O_2 and subsequent radical formation, have been neglected in literature for EHC. In this chapter, the effect of H_2S, CO, CO_2,NH_3, and natural gas on the EHC's performance is systematically investigated, and operation strategies to mitigate the effect of the gas impurities are tested for suitability for EHC operation.

Table 4.2: Overview of studies on poison impact in low and high-temperature electrochemical hydrogen compression, NG: natural gas.

Study	Membrane	Effect of CO	CO_2	H_2S	NH_3	NG	Poison mitigation	Mix with CH_4	Compr. and sep.	Product gas Purity
[Nord2020]	Nafion		x							
[Jack2020]	Nafion	x		x			x			
[Verm2021b]	TPS	x	x		x					x
[Durm2022]	PBI	x	x							
[Maxw2023]	PBI	x	x							x
[Jack2023]	Nafion					x				x
[Mrus2024]	Nafion							x	x	
[Arun2024]	PBI					x			x	x
This work	Nafion, PBI	x	x	x	x		x	x	x	(x)

4.2 Materials and Methods

The methods used are described in Chapter 3.2.

8 % CO_2 blended with H_2 and N_2 5.0 and natural gas H was supplied from Westfalen AG (GER), 8 ppm H_2S in H_2, 60 ppm in H_2, H_2 5.0 and Ar 4.8 from Air Products & Chemicals (USA). 28.5 ppm NH_3 in H_2, CH_4 4.5 and synthetic air were obtained from Taiyo Nippon Sanso Corporation (JP).

4.2.1 Poisoning and poison mitigation

Table 4.3 lists the procedure for the poisoning experiments. Before the contaminants are introduced into the system, measurements are denoted as BoT (Beginning of Test) and afterward as EoT (End of Test). Data obtained after performing a mitigation strategy are labeled according to the strategy.

Before the recording of the BoT measurements, the EHC was operated at the experimental conditions, without the contaminant, at 400 mA cm^{-2} until the change in potential was less than 1 µV s^{-1}. A new MEA was used for each contaminant. For H_2S contamination, three CV oxidation cycles were added before the test procedure to remove residual H_2S. ECSA, electrochemical impedance, and polarization were recorded at BoT (Fig. 4.2 (0)), EoT (Fig. 4.2 (4)), and after mitigation. After measuring the BoT, the system was again run at 500 mA cm^{-2} with pure H_2 feed for a minimum of 30 min until the change of potential was less than 1 µV s^{-1}. However, only the last 30 min will be shown in the data. The contaminants were then fed to the EHC for 3.5 h or the mentioned time period (Fig. 4.2 (1-2)). Then, the feed was switched back to pure H_2 for 15 min(Fig. 4.2 (2-3)) and then back to the contaminant for the remainder of the measurement to verify the observations (Fig. 4.2 (3-4)). The EoT was measured (Fig. 4.2 (4)). Then, the mitigation strategy was performed. The following mitigation strategies were employed. For air bleeding, synthetic air was introduced for 90 seconds at 150 mL min^{-1}. Before and after the air bleed, the cell was flushed with N_2 for 30 s at the same flow rate. For cyclic oxidation, 5 CV cycles were performed in the potential window of 0.02 to 1.2 V at a scan rate of 35 mV s^{-1}.

Table 4.3: Experimental protocol for the investigation of catalyst poisoning. CV: Cyclic voltammetry; OCV: Open circuit voltage; CA: Chronoamperometry; LSV: Linear sweep voltammetry; GEIS: galvanostatic electrochemical impedance spectroscopy; CP: Chronopotentiometry; PC: Polarization curve.

Index	Group	Technique	Settings	Duration
1	CV cleaning	CV		
2	Stabilization	CP	10 A	
3	BoT	CV anode 1		
4	BoT	CV cathode 1		
5	BoT (PC1)	CP 1-1	0.25 A	2 min
6	BoT (PC1)	CP 1-2	2.5 A	2 min
7	BoT	GEIS 1	0.25 A	3 min
8	BoT (PC1)	CP 1-3	5 A	2 min
9	BoT (PC1)	CP 1-4	7.5 A	2 min
10	BoT (PC1)	CP 1-5	10 A	2 min
11	Poisoning	CP 12-6	12.5 A	4.5 h
12	EoT (PC2)	CP 2-5	10 A	2 min
13	EoT (PC2)	CP 2-4	7.5 A	2 min
14	EoT (PC2)	CP 2-3	5 A	2 min
15	EoT (PC2)	CP 2-2	2.5 A	2 min
16	EoT	GEIS		3 min
17	EoT (PC2)	CP 2-1		2 min
18	EoT	CV anode 2		
22	EoT	CV cathode 2		
23	Mitigation			
24	After Mitigation (PC3)	CV anode 3		
25	After Mitigation (PC3)	CV cathode 3		
26	After Mitigation (PC3)	CP 3-1	0.25 A	2 min
27	After Mitigation (PC3)	CP 3-2	2.5 A	2 min
28	After Mitigation (PC3)	GEIS 3		3 min
29	After Mitigation (PC3)	CP 3-3	5 A	2 min
30	After Mitigation (PC3)	CP 3-4	7.5 A	2 min
31	After Mitigation (PC3)	CP 3-5	10 A	2 min
32	After Mitigation (PC3)	CP 3-6	12.5 A	2 min
(33)	-	(CV anode 4)		
(34)	-	(CV cathode 4)		

When performing cyclic heating, the cell was repeatedly heated to 160°C, then switched off until the base temperature of 120°C was reached.

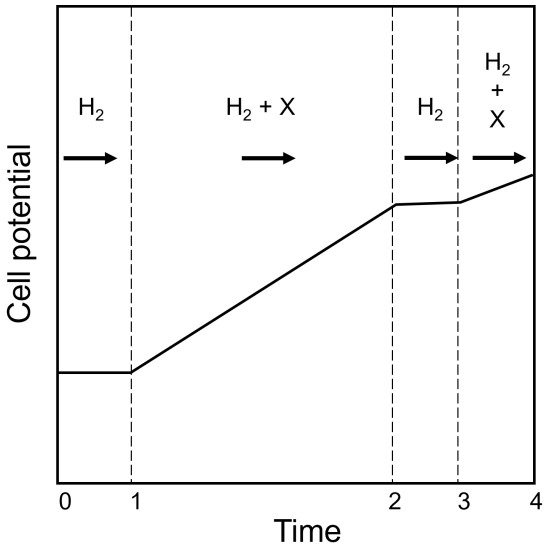

Figure 4.2: Illustration of the experimental method for the poisoning experiments.

4.2.2 Electrochemically active surface area (ECSA) determination

The electrochemically active surface area (ECSA) was determined via underpotential hydrogen adsorption and desorption method [Luka2016; Tras1992]. To determine the ECSA, the potential is cycled between 0.02 to 0.6 V at a scan rate of 35 mV s^{-1} unless otherwise noted. A minimum of five cycles are performed until the CV is stable. The CV measurements are performed using dry gas at a flow rate of 25 mL min^{-1}. The last cycle is used to determine the ECSA according to Eqn. 4.11 by manual integration of the respective areas (A_{ads}, A_{de}) in *EC-Lab* and with the specific oxidation charge q_{Pt} = 210 µC cm^{-2} [Luka2016].

$$\text{Area per area of GDE: } ECSA = 0.5 \cdot \frac{A_{ads} + A_{de}}{q_{Pt} \cdot Scanrate} \tag{4.11}$$

4.3 Results

4.3.1 Impact of CO_2 in H_2 on the EHC performance

To differentiate the effect of the contaminants in NG, mixtures of H_2 and single poisons were introduced to the EHCs. The cell potential of the Nafion-EHC, presented in Figure 4.3 (a), increases for 3 h upon introduction of 4 vol% CO_2 until stabilizing at 180 mV, which is a 35 mV increase in cell potential compared to the BoT. The potential does not recover when switching the feed back to pure H_2. When CO_2 is introduced to the Celtec-MEA, the cell potential increases by 3 mV and drops by 2 mV once switching back to pure H_2. The EoT polarization curves (Fig. 4.4) show a 20 % increase in the potential for the Nafion-EHC and a 3 % increase for the Celtec-EHC (Fig. 4.4), which is also observed in the iR-corrected polarization curve, indicating that the increased potential is mainly caused by deteriorating charge or mass transfer. With 4 % CO_2, an increase of 0.6 to 0.7 mV would be expected from the Nernst equation depending on the operating temperature. The charge transfer resistance of the Nafion-EHC in the EoT EIS strongly increases (Fig. 4.3 (b)), while no significant changes are observed for the Celtec-EHC. The potential and charge transfer resistance increase can be attributed to catalyst poisoning by CO_2 and CO, formed by RWGS (Eqn. 4.2), adsorption on the Pt active sites, decreasing the active catalyst surface for the HOR [Durm2022; Nord2020].

The ECSA of the electrodes was determined before and after the poisoning experiments. A reference experiment with H_2 and CH_4 showed an ECSA reduction of 3.6 % for the anode and 5.8 % for the cathode (Fig. 4.7). The ECSA was determined using the last of at least five cycles; consequently, changes in ECSA due to oxidation of adsorbed species in prior cycles are undetected. The ECSA analysis could not be performed for CO_2 because most of the adsorbed CO was oxidized in the 'pre-peak' region below 0.6 V (Fig. 4.3 (c)) [McPh2017]. However, in the CV of the anode at EoT, a reduced hydrogen oxidation charge (0.1 to 0.3 V) can be qualitatively observed (Fig. 4.3 (c)). The oxidation peak in CO-stripping can also be observed in the CV of the cathode in Figure 4.3 (d), indicating that CO_2

crossover to the cathode side occurs. The cathode catalyst is also poisoned as CO is formed by electroreduction of CO_2 (Eqn. 4.3). For the Celtec-EHC, a more severe decrease of the anode ECSA of 12 % was measured (Fig. 4.7), which can be caused by increased CO formation from the RWGS at higher temperatures and low humidity. For the Celtec-EHC no CO oxidation peak was observed at potentials below 0.6 V (Fig. 4.5 (c)).

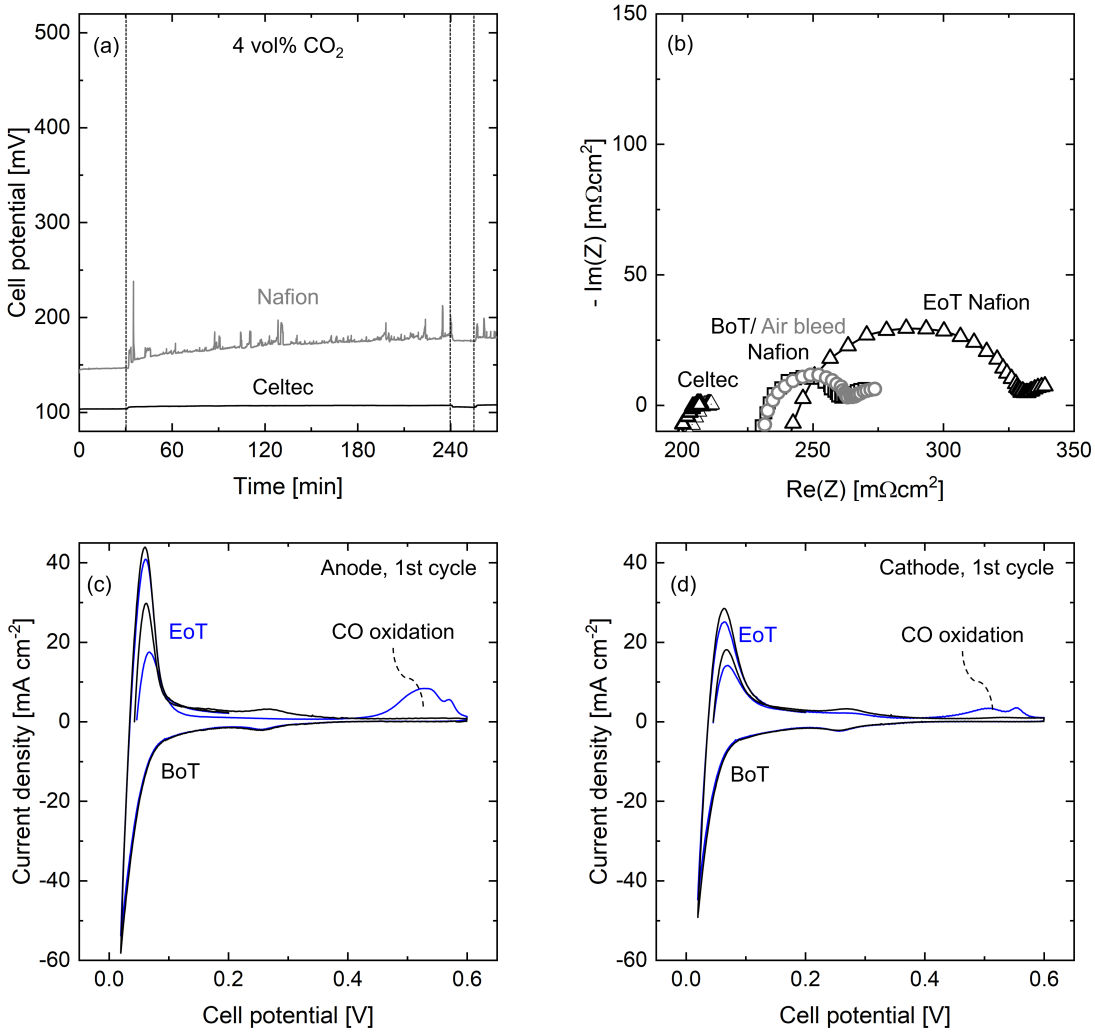

Figure 4.3: Cell potential over time when adding 4 vol% CO_2 to the EHC feed, 500 mA cm^{-2}, λ = 1.6, Nafion-EHC: 70 °C, 100 % RH; Celtec-EHC: 120 °C, 0.7 % RH; (b) Electrochemical impedance spectra with 4 vol% CO_2 Beginning of Test (BoT): squares, End of Test (EoT): triangles, after air bleed: grey circles; First cycle of the cyclic voltammograms of the Nafion-EHC, black: BoT, blue: EoT, (c) Anode, (d) Cathode.

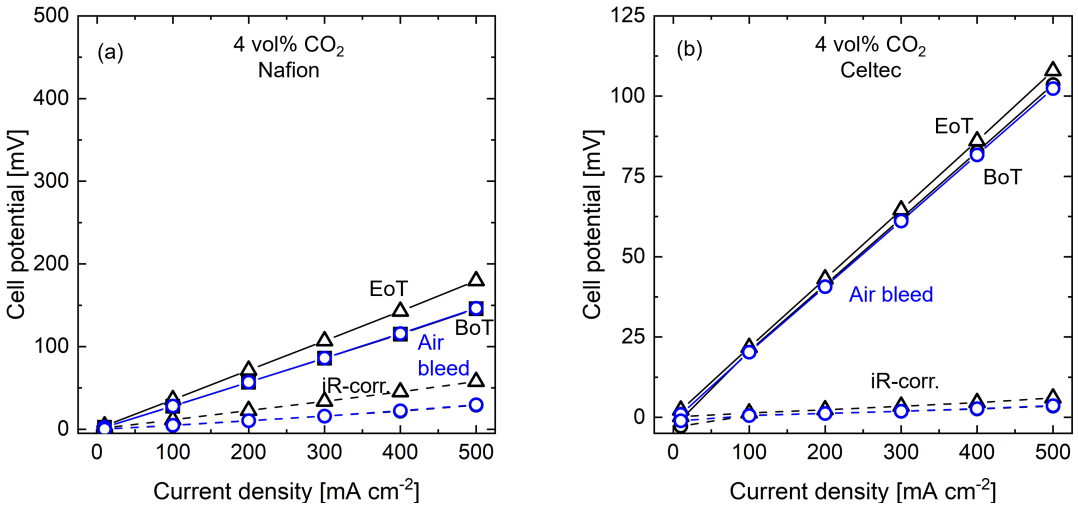

Figure 4.4: Polarization behavior of Nafion-EHC, 70 °C, 100 % RH and Celtec-EHC, 120 °C, 0.7 % RH, EoT: End of Test, BoT: Beginning of Test, Air bleed (blue): After flushing the anode compartment with synthetic air for 90 s.

4.3.2 Impact of CO in H_2 on the EHC performance

With 30 ppm CO in the feed stream, the cell potential of the Nafion-EHC, shown in Figure 4.5, rises steeply for the first 30 min and then increases until stabilizing after about 3 h at 380 mV (Fig. 4.5 (a)). At controlled current operation, an equilibrium between CO adsorption and oxidation is maintained, leading to operation at elevated potential [Gard2007; Jusy2001]. When switching back to H_2, the potential drops steeply but immediately jumps back to 380 mV when CO is reintroduced. This stark change can also be observed in the charge transfer resistance semi-circle in the EIS analysis (Fig. 4.5 (b)). For the Celtec-EHC, the potential rises with decreasing slope by 4 mV over 3.5 h (Fig. 4.5 (a)). The poisoning effect of CO is less severe for the Celtec-EHC because the equilibrium surface coverage of CO on the Pt catalyst is reduced with increased temperature [Trég2020]. Additionally, HER and HOR kinetics are faster at increased temperatures, and the Celtec-EHC has a higher catalyst loading. When adding 50 vol% CH_4 to the feed of the Celtec-EHC, the potential increases by 11% (Fig. 4.7 (a)). In the Nafion-EHC EoT polarization curve (Fig. 4.6 (a)), a jump in potential with a 200 % increase is observed from 100 mA cm^{-2} on. The potential remains at the oxidation potential of CO, indicating a high catalyst surface coverage

with CO. An increase of 4 % is observed in the EoT polarization curve of the Celtec-EHC (Fig. 4.6 (b)). The ECSA of the Celtec-EHCs anode decreased by 24 % with CO (Fig. 4.7).

The performance was restored for both cells by an air bleed after poisoning with CO_2 or CO. In summary, adding 4 vol% CO_2 or 30 ppm CO to the feed gas strongly impaired the Nafion-EHC performance, while for the Celtec-EHC, a minimal increase in cell potential was observed.

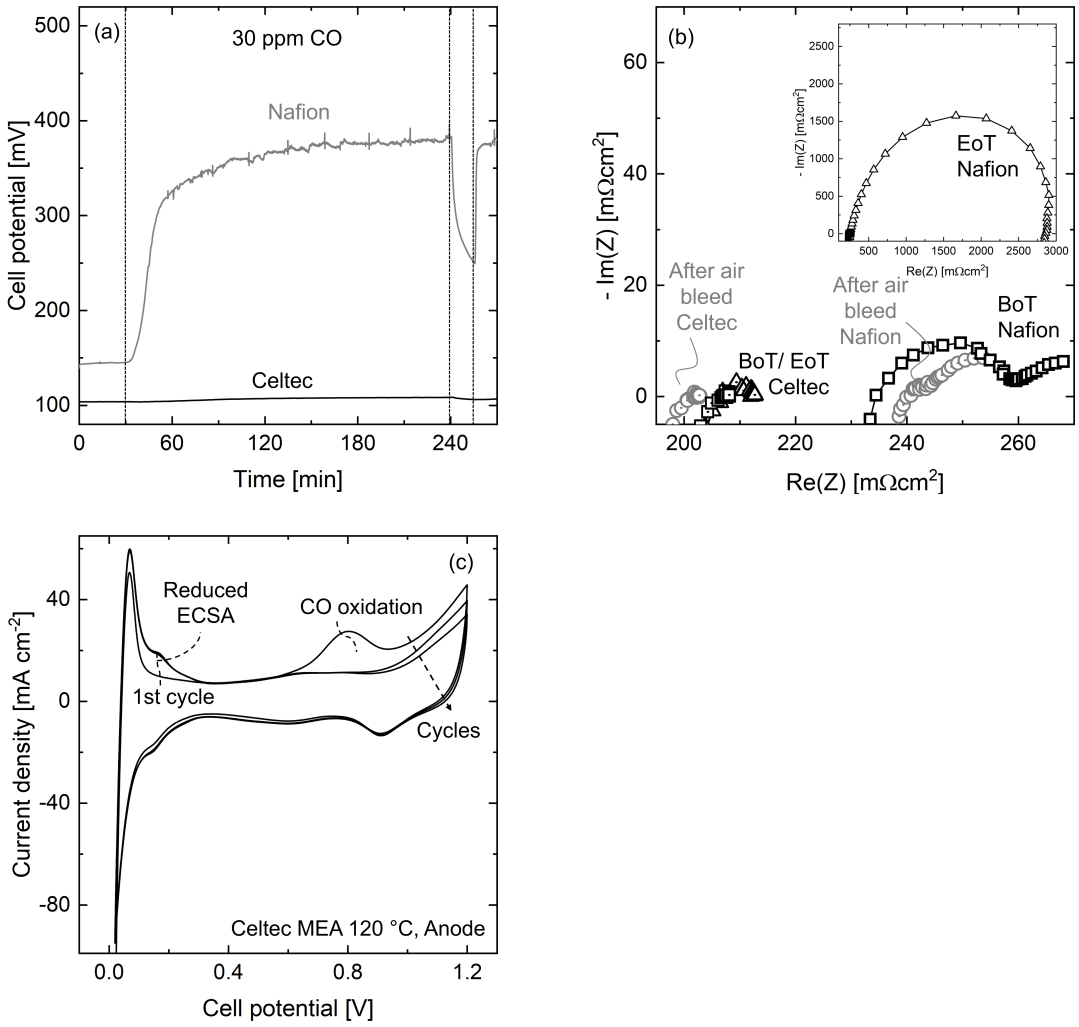

Figure 4.5: (a) Cell potential over time when adding 30 ppm CO to the EHC feed, 500 mA cm^{-2}, λ = 1.3 for CO; Nafion-EHC: 70 °C, 100 % RH; Celtec-EHC 120 °C, 0.7% RH; (b) Electrochemical impedance spectra with 30 ppm CO Beginning of Test (BoT): squares, End of Test (EoT): triangles, After air bleed (flushing the anode compartment with synthetic air for 90 s): grey circles; (c) CV-cleaning of the Celtec-EHC.

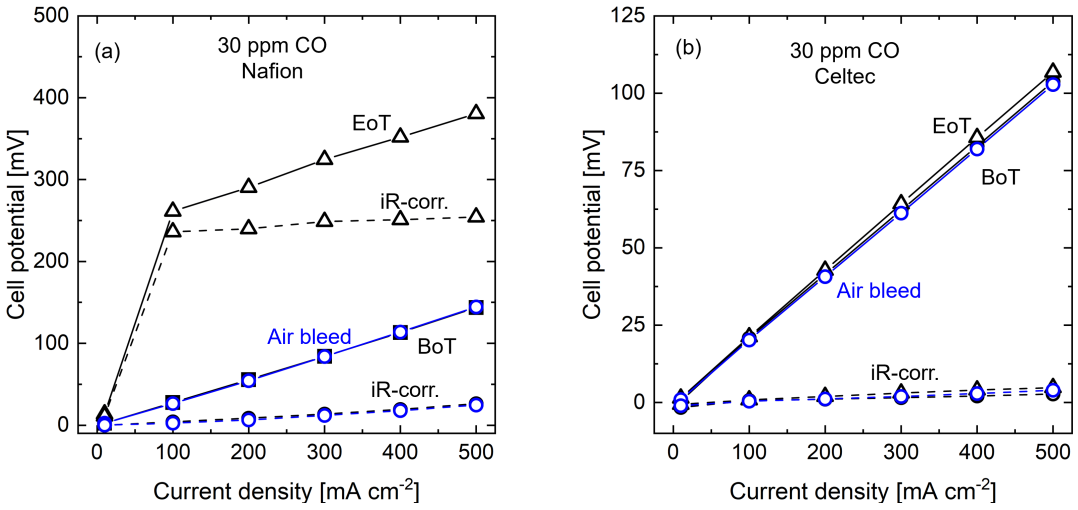

Figure 4.6: Polarization behavior of Nafion-EHC, 70 °C, 100 % RH and Celtec-EHC, 120 °C, 0.7 % RH, EoT: End of Test, BoT: Beginning of Test, Air bleed (blue): After flushing the anode compartment with synthetic air for 90 s.

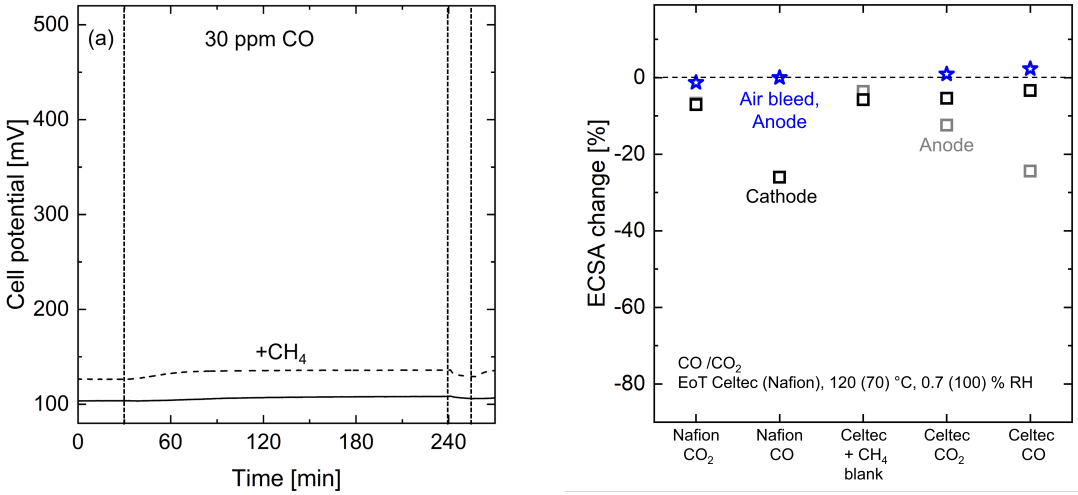

Figure 4.7: (a) Impact of CO poisoning when feed stream is diluted with CH_4 (dashed lines), λ = 1.6, NH_3 50 vol% CH_4, undiluted measurement as reference (solid line), 120 °C, 0.7% RH; (b) Electrochemically active surface area change from BoT to EoT (black: Cathode, grey: anode) and from BoT to after 90 s air bleed (blue); BoT: Beginning of Test (Triangles); EoT: End of Test (Squares); Grey: Anode, Black: Cathode, Air bleed (blue): After flushing the anode compartment with synthetic air for 90 s.

4.3.3 Impact of NH_3 in H_2 on the EHC performance

Adding 14 ppm NH_3 to the feed of the EHC, a slight increase in cell potential slope (0.76 mV h^{-1}) can be observed for the Nafion-EHC, in Figure 4.8 (a), compared to the reference experiment without poison (0.12 mV h^{-1}). Figure 4.8 (b) shows the EIS analysis of the Nafion-EHC before and after poisoning. The EoT measurement shows an increased HFR and charge transfer resistance. The increased HFR and charge transfer resistance might be attributed to reduced ionomer conductivity by ion exchange to the NH^+ form of Nafion™[Urib2002]. However, the effect observed herein of adding 14 ppm NH_3 is less severe than reported in literature by Halseid et al. [Hals2007] for a Gore MEA at 40 °C, which might be due to the higher operating temperature and the thicker membrane used in our study [Soto2003]. No significant changes in cell potential (Fig. 4.8 (a)), impedance spectra (Fig. 4.8 (b)) or polarization behavior (Fig. 4.9) can be observed for the Celtec-EHC during the 3.5 h poisoning experiment with 14 ppm NH_3, also when diluted with CH_4 (Fig. 4.10 (a)).

To challenge the Celtec-MEA for long-term operation stability when introducing NH_3, a long-term test for 75 h alternately introducing H_2 with 14 ppm NH_3 and pure H_2 for 12 h was performed (Fig. 4.8 (d)). For the periods with a pure H_2 feed, the potential declines with an average slope of $-83\,\mu V\,h^{-1}$ while during the periods with NH_3 the potential increases by $124\,\mu V\,h^{-1}$. Although no change in potential was measured in the 3.5 h poisoning experiment, these observations indicate an adverse long-term effect of NH_3 on the Celtec-EHC, which could be caused by reduction of the membrane conductivity by the interaction of NH_3 with H_3PO_4 (Eqn. 4.7). The long-term adverse effect of NH_3 has been reported for fuel cells with Celtec MEAs [Scho2021].

Even though the charge transfer resistance increased significantly, the change in cell potential after 3.5 h NH_3-poisoning in the Nafion-EHC was minimal. This can be explained by the HFR dominating the cell potential, which increased after poisoning but only minimal. After CV-cleaning, the charge transfer resistance and the HFR decrease. Consequently, CV-cleaning mitigates NH_3 poisoning, but it is unclear if the poisoning is com-

pletely reversible. Longer poisoning experiments focusing on the ionomer and membrane conductivity should be conducted in future research to further elucidate the effect of NH_3 on Nafion-EHCs and possible mitigation strategies.

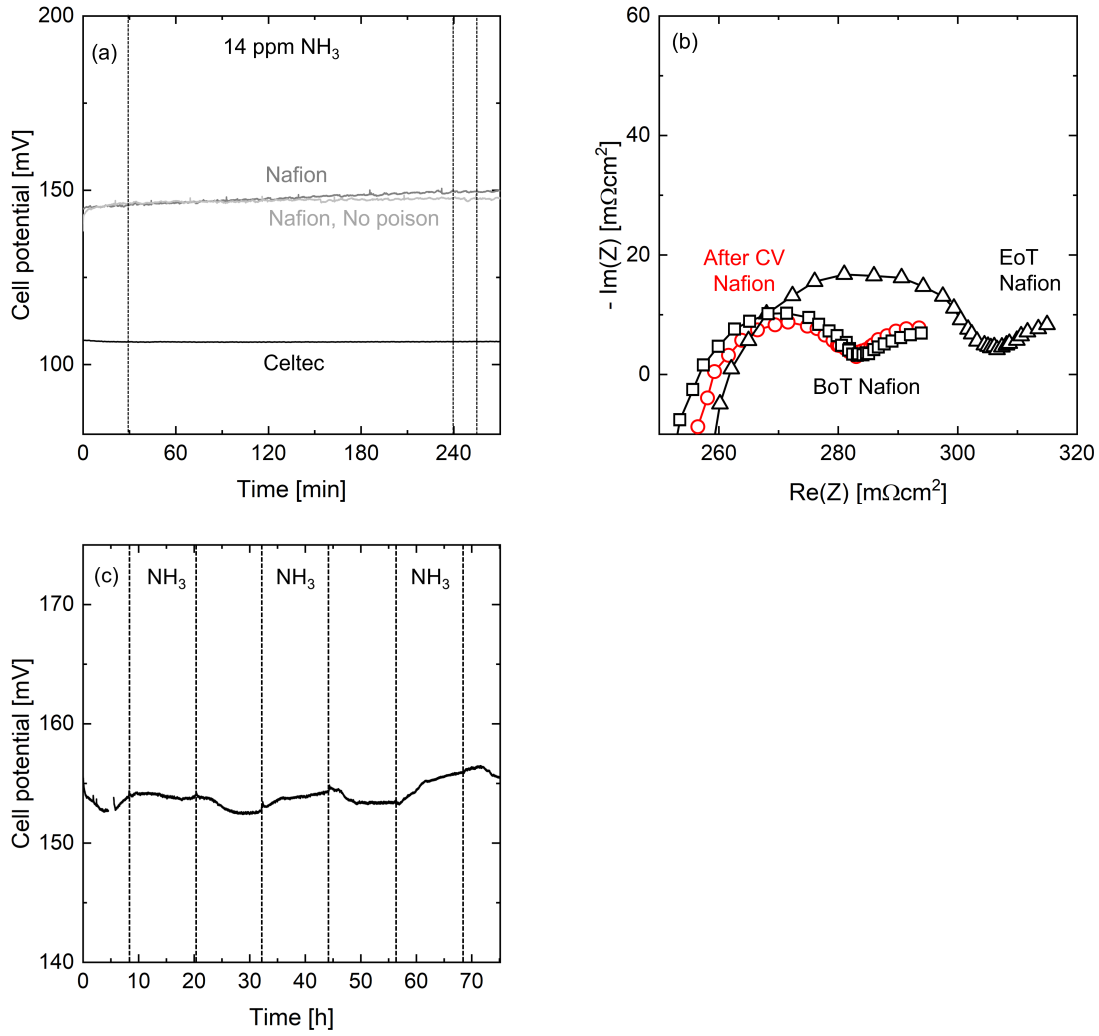

Figure 4.8: (a) Cell potential over time when adding 14 ppm NH_3 to the EHC feed, no poison was introduced for the first 30 min and from 240 to 255 min, 500 mA cm^{-2}, λ = 1.3; Nafion-EHC: 70 °C, 100 % RH; Celtec-EHC: 120 °C, 0.7 % RH; (b) Electrochemical impedance spectra with 14 ppm NH_3, Beginning of Test (BoT): squares, End of Test (EoT): triangles, after CV cleaning: red circles; (c) Cell potential of a Celtec EHC when alternately introducing H_2 with 14 ppm NH_3 and pure H_2 for 12 h each, 120 °C, 0.7 % RH, λ = 1.3.

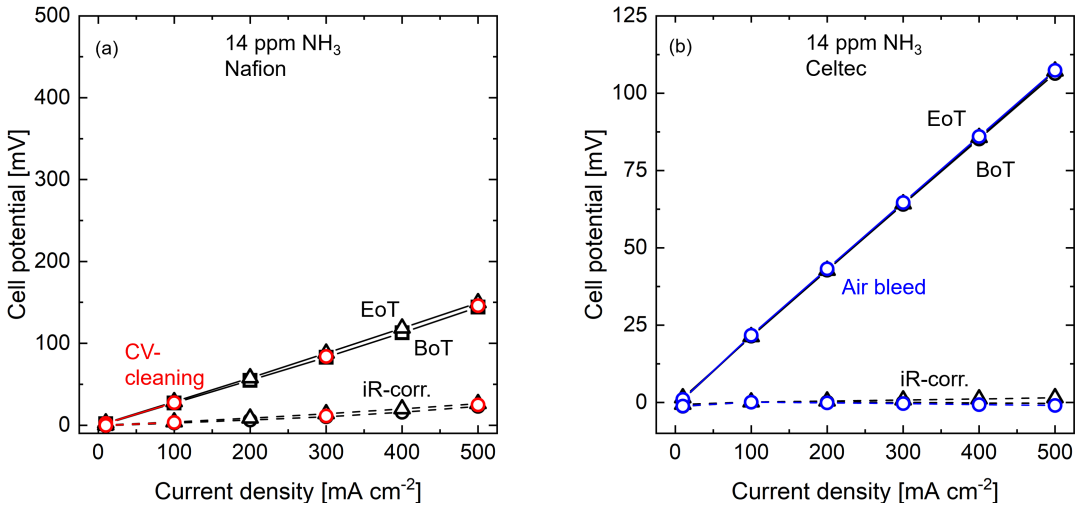

Figure 4.9: Polarization behavior of (a) Nafion-EHC, 70 °C, 100 % RH and (b) Celtec-EHC, 120 °C, 0.7 % RH, EoT: End of Test, BoT: Beginning of Test, CV-cleaning: After electro-oxidation by CV cycling (red), Air bleed (blue): After flushing the anode compartment with synthetic air for 90 s.

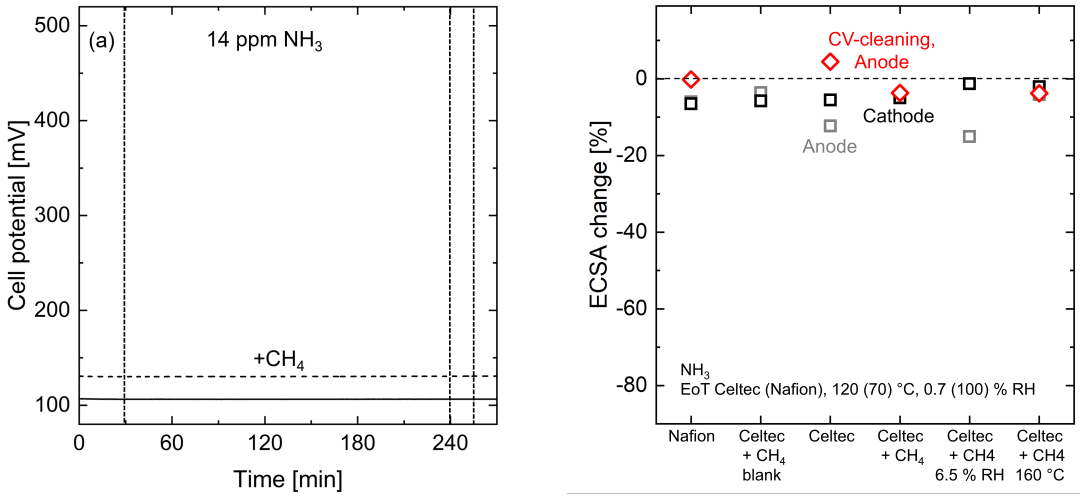

Figure 4.10: (a) Impact of NH_3 poisoning when feed stream is diluted with CH_4 (dashed lines), λ = 1.6, NH_3 51 vol% CH_4, undiluted measurement as reference (solid line), 120 °C, 0.7% RH; (b) Electrochemically active surface area change from BoT to EoT (black: Cathode, grey: anode) and from BoT to after CV-cleaning (red); BoT: Beginning of Test (Triangles); EoT: End of Test (Squares); Grey: Anode, Black: Cathode.

4.3.4 Impact of H_2S in H_2 and H_2/CH_4 mixtures on the EHC performance

When introducing 3.5 ppm H_2S to the Nafion-EHC, the cell potential starts increasing 30 min after the poison is introduced and then rises linearly until it reaches 420 mV after 3.5 h. Even when the feed is switched back to pure H_2, the cell potential continues to increase, see Fig. 4.11 (a). The charge transfer resistance semi-circle in the EoT EIS analysis increased (Fig. 4.11 (b)). The cell potential of the Celtec-EHC increases by 1 mV throughout the poisoning experiment with H_2S, and no significant change can be observed in the EIS analysis (Fig. 4.11 (a) & (d)). The potential in the EoT polarization curve increased by 267 % for the Nafion-EHC (Fig. 4.12). For the Celtec-EHC, no significant change in polarization behavior was observed in the 3.5 h poisoning test (Fig. 4.12). The ECSA of the Nafion-EHC anode, presented in Figure 4.13, decreased by 80 % at EoT while the ECSA of the Celtec-EHC anode decreased by 21 % at EoT.

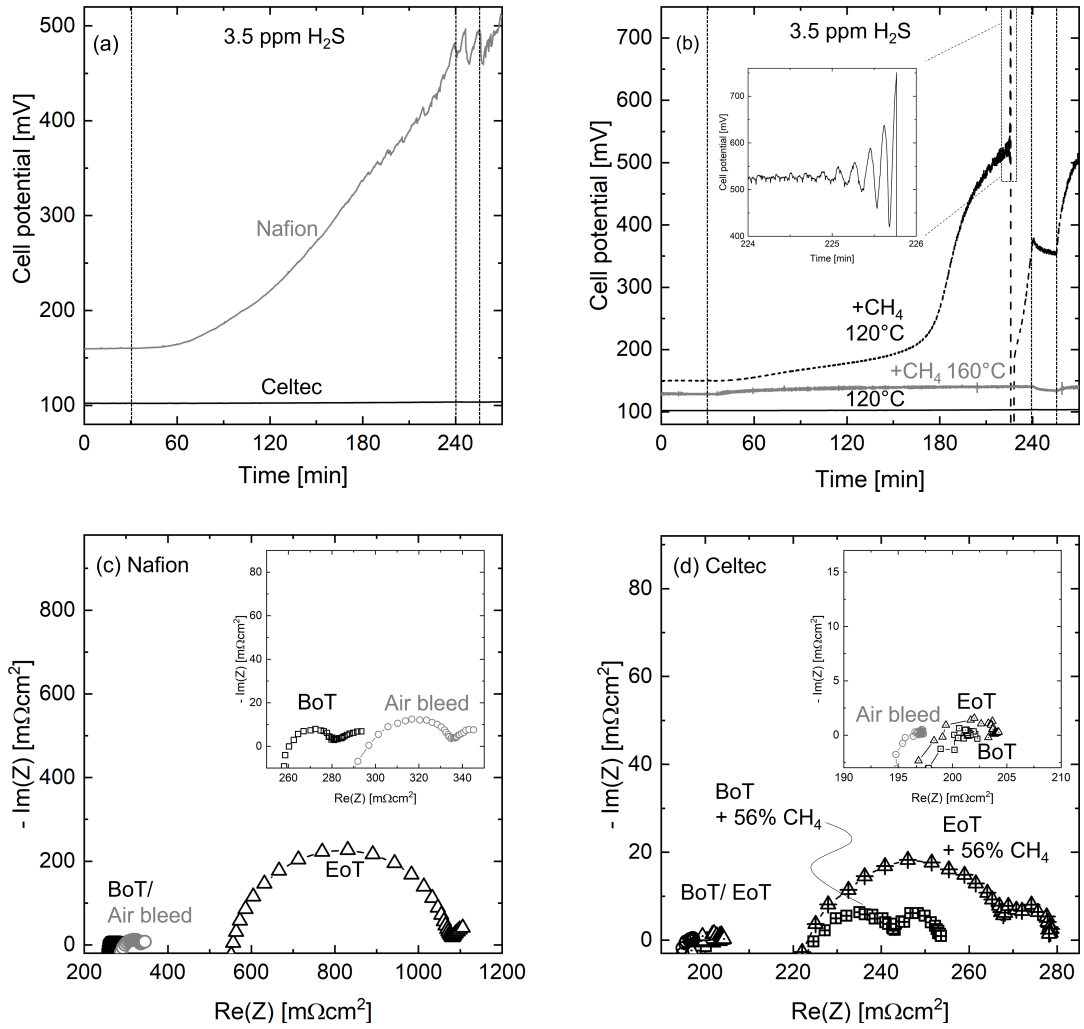

Figure 4.11: (a) Impact of 3.5 ppm H_2S on EHC performance, 500 mA cm^{-2}, λ = 1.3; Nafion-EHC: 70 °C, 100 % RH; Celtec-EHC 120 °C, 0.7 % RH; (b) Impact of H_2S when feed stream is diluted with CH_4, λ = 1.6 H_2S 56 vol% CH_4; Electrochemical impedance spectra, (c) of a Nafion™117 MEA with with 3.5 ppm H_2S BoT: squares, EoT: triangles, after air bleed: grey circles; (d) of a Celtec MEA with 3.5 ppm H_2S BoT: squares, EoT: triangles, after air bleed: grey circles with 3.5 ppm H_2S and 56 vol% CH_4 (symbols with cross).

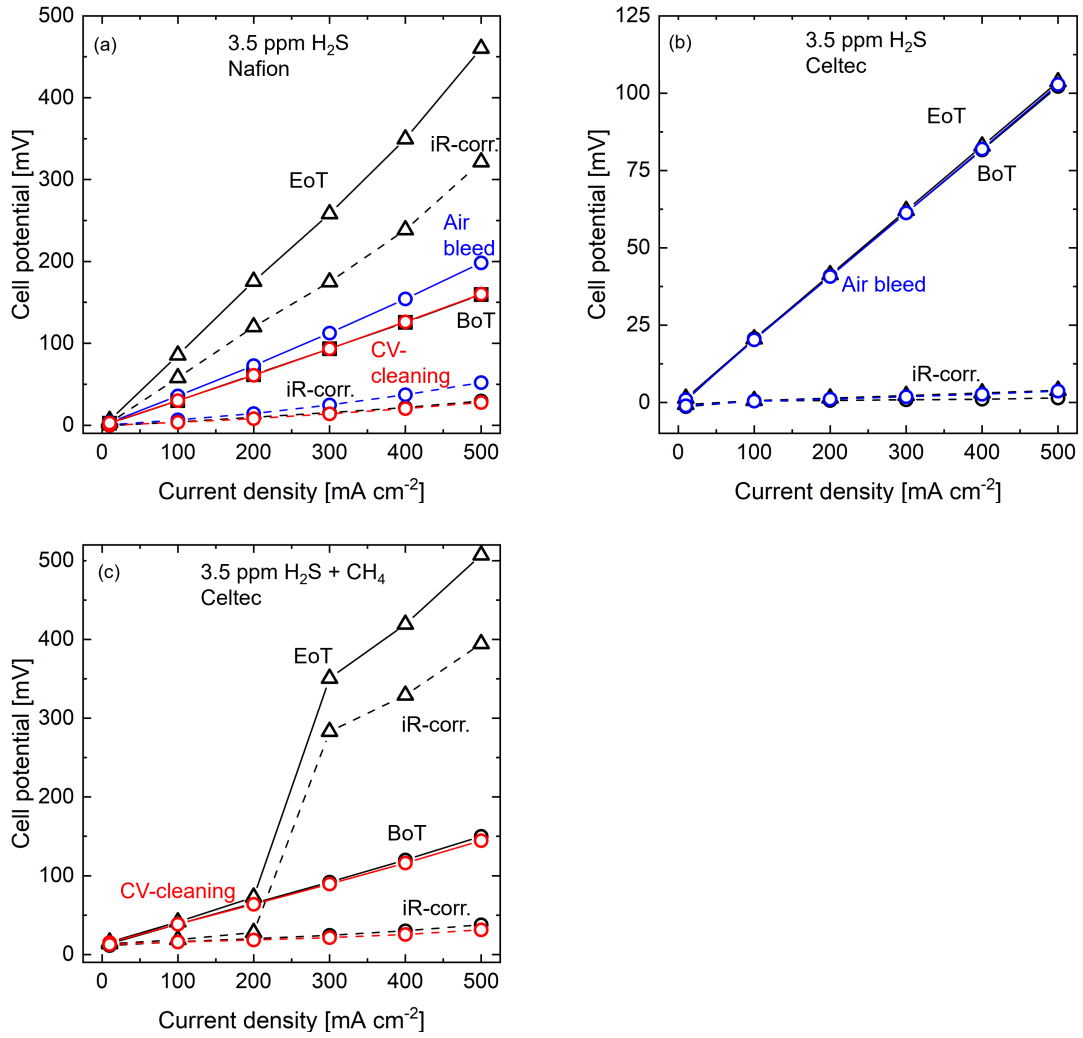

Figure 4.12: Polarization behavior before (BoT: Beginning of Test) and after (EoT: End of Test) adding 3.5 ppm H_2S of (a) Nafion-EHC, 70 °C, 100 % RH and (b) Celtec-EHC, 120 °C, 0.7 % RH, (c) Celtec-EHC with 56 % CH_4, 120 °C, 0.7 % RH.

When diluting the H_2S/H_2 feed stream of the Celtec-EHC with CH_4 (Fig. 4.11 (b)), the cell potential increases linearly for about 150 min reaching 200 mV. Subsequently, the potential increases exponentially for approximately 30 min until the slope decreases while potential oscillations can be observed. The amplitude of the oscillations increases until a potential spike to the potential limit of the potentiostat occurs after about 225 min, after which the cell potential drops and the process is repeated. The EoT charge transfer resistance approximately doubled compared to the BoT measurement (Fig. 4.11 (c)). With the diluted H_2S/H_2 feed stream, an increased HFR and charge transfer resistance compared to the non-diluted feed can

be observed in the impedance spectrum at BoT and EoT (Fig. 4.11 (d)). Additionally, a second semi-circle indicating mass transport limitation was measured. At EoT the charge transfer resistance increases compared to BoT, indicating catalyst poisoning and a disrupted proton conduction path. The ECSA with diluted H_2S/H_2 feed decreases by 25 % compared to BoT, which is 5 % more compared to the undiluted feed (Fig. 4.13). Possibly, even more severe ECSA reduction from sulfur-poisoning occurred during the poisoning experiment, but high cell potentials during the self-oxidation cycles probably lead to partial oxidation of the adsorbed sulfur species recovering the catalyst area.

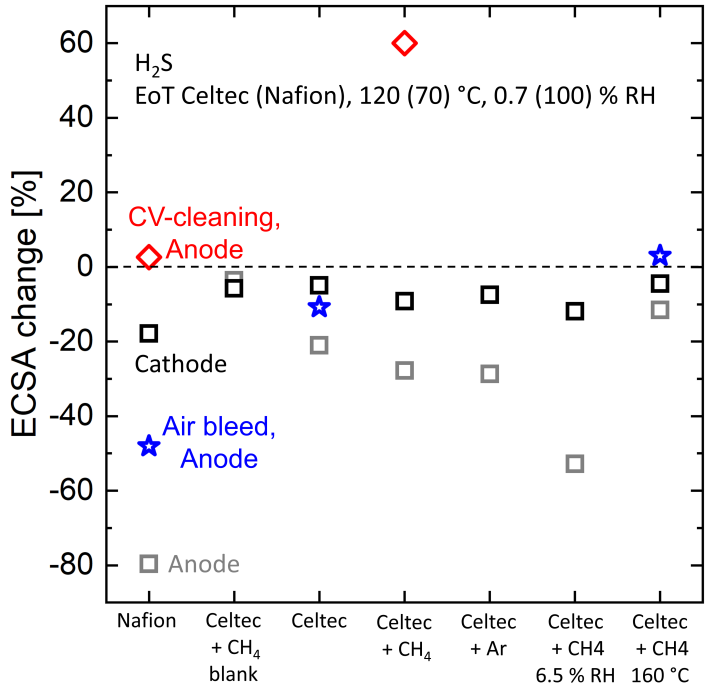

Figure 4.13: Electrochemically active surface area change when adding 3.5 ppm H_2S to the EHC feed from BoT to EoT (black: Cathode, grey: anode) and from BoT to after 90 s air bleed (blue) and from BoT to after CV-cleaning (red) in percent; BoT: Beginning of Test (Triangles) ; EoT: End of Test (Squares); Grey: Anode, Black: Cathode.

The detrimental effect upon dilution can be explained by the poisoning mechanisms of H_2S. H_2S dissociates to S and H_2 when adsorbing to Pt (Eqn. 4.5). Consequently, with decreased H_2 share in the feed, the adsorption equilibrium is shifted towards sulfur adsorption. The significant increase

in cell potential after 150 min may be induced by the start of electro-oxidation of H_2S, which has a thermodynamic equilibrium potential of 165 mV vs. SHE [Faro1977]. Pt – S interferes electrostatically with the adjacent active sites, leading to more severe poisoning due to a greater reduction of active catalyst. Additionally, the electrochemical dissociation may hinder the backreaction of Pt – S to H_2S and Pt because the intermediate of the reaction (Pt – H_2S) is electrochemically oxidized [Zolf1999]. The potential spike may be caused by severe catalyst poisoning, which leads to an increase in cell potential until the oxidation potential for sulfur is reached. The oxidation onset potential for sulfur oxidation to SO_2 at 70 °C is between 500 to 600 mV vs. DHE [Seth2010]. The polarization curves displayed in Figure 4.12 (c) show a strong potential dependence of the poisoning. Between 200 to 300 $mAcm^{-2}$, a pronounced non-linear increase in cell potential was observed, which coincides with the start of electro-oxidation of H_2S to S and the enhanced poisoning thereof. Moreover, Sethuraman et al. [Seth2010] propose an increase in the adsorption degree of sulfur species until 500 mV vs. DHE and a decrease at higher potentials, which could also lead to more pronounced poisoning at elevated cell potentials.

Oscillating phenomena are reported for sulfide oxidation on Pt [Feng2005]; however, they are not reported for the EHC or PEM fuel cells when H_2S is introduced. Jackson et al. [Jack2020] conducted the only EHC study investigating H_2S by operating a low-temperature EHC with reformate/H_2S mixtures under potentiostatic conditions. Upon the introduction of 100 ppb H_2S, the current decreased to 2 % of the current observed without poisoning. Due to the controlled potential in their study, the oxidation potential of sulfur species could not be reached, preventing the attainment of the second metastable state necessary for system oscillation. In contrast, our study examined H_2S poisoning in a high-temperature EHC under amperostatic conditions. We propose that the harmonic oscillations before the potential spike are caused by periodic adsorption and partial oxidation of sulfur species, temporarily cleaning the catalyst surface and lowering the cell potential.

Another reason for the increased poisoning could be the onset of CH_4

oxidation at 169 mV, and corresponding increased poisoning by the CO_2 and CO formed [Jack2020]. However, the oscillatory behavior was also observed when the feed gas was diluted with Ar instead of CH_4 (Fig. 4.14 (b)). Consequently, CH_4 oxidation does not significantly contribute to the observed behavior. When changing from CH_4 to Ar the smaller oscillations leading to the self-oxidation are reduced (Fig. 4.14(b), (c)). This minor change in oscillation pattern might be attributed to the additional poisoning of CO from CH_4 oxidation.

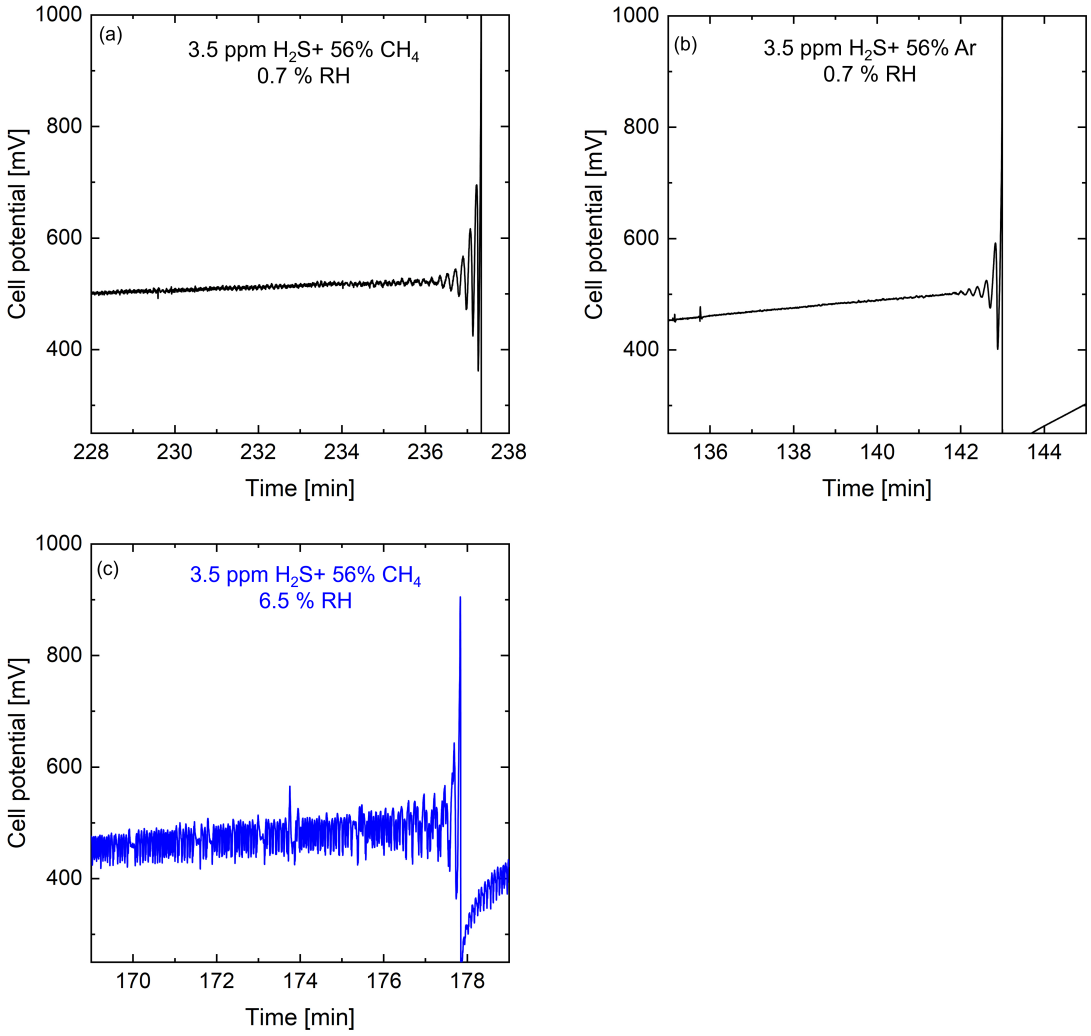

Figure 4.14: Potential oscillations when operating the Celtec-EHC with diluted H_2/H_2S feed. (a) Zoom in on oscillation with CH_4-diluted feed, with 3.5 ppm H_2S and 56 vol% CH_4 with 0.7 % RH, (b) Zoom in on oscillation with Ar-diluted feed 56 vol% Ar with 0.7 % RH (c) Cell potential over time of a Celtec-EHC at 500 mA cm^{-2} and 120 °C, with 3.5 ppm H_2S 56 vol% CH_4 with 6.5 % RH.

When increasing the relative humidity of the diluted feed to 6.5 % (Fig. 4.14 (c), 4.15), the oscillation amplitude is increased and there is no linear phase at low potentials before the exponential increase in cell potential, which could be caused by facilitated dissociative adsorption with more water present leading to enhanced poisoning. Moreover, catalyst recovery might be compromised by H_2S dissociation into HS^- upon desorption and HS^- being adsorbed again. The potential spike height is lowered to 0.9 V, and the frequency of the oscillation cycles is increased. This could be caused by faster sulfur oxidation when more water is present as water is consumed in the Pt-S oxidation [Louc1971]. Similar to the observations from the Nafion-EHC with H_2S- poisoning, the potential continues to increase upon discontinuation of H_2S (Fig. 4.15), which could be due to continuing dissociation of H_2S into HS^-. Additionally, H_2S previously adsorbed in the carbon support of the MEA might desorb and lead to continued poisoning of the catalyst. Due to the accelerating effect of water on H_2S poisoning of the EHC, the relative humidity of the feed should be optimized.

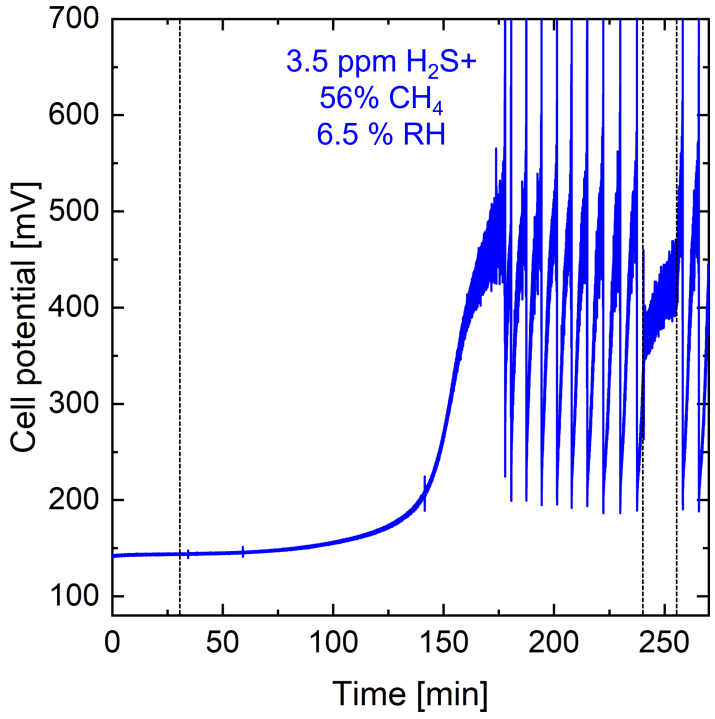

Figure 4.15: Impact of 3.5 ppm H_2S on EHC performance, 500 mA cm^{-2}, λ = 1.3; Celtec-EHC 120 °C, 6.5 % RH.

The operation with CH_4-diluted H_2S/H_2 becomes stabilized when operating the EHC at 160 °C (Fig. 4.11 (b), grey line). The cell potential increases by 10 mV upon adding H_2S to the feed, remains stable over 3.5 h, and drops by 7 mV when switching to pure H_2. The less severe effect of H_2S at 160 °C can be attributed to less adsorption of H_2S and a weakened Pt-S bond [Ke2023; Moht2005]. Additionally, the catalyst activity is increased, so less catalyst is needed to support the HOR.

In addition to the immediate effects of H_2S, a decline in the performance of the Celtec-MEA used for the H_2S poisoning experiments conducted was observed throughout the experiments. The same Celtec-MEA was used for the H_2S experimental series. The performance decline is probably caused by the irreversible loss of catalytic activity when operated with H_2S, which is reported for fuel cells. Hard-to-oxidize species are specially formed at potentials above 500 mV, and the catalyst structure is altered. Consequently, exceeding this anode overpotential should be avoided in operation [Seth2010].

4.3.5 Poison mitigation strategies for H_2S

For all poisons, except H_2S, the potential increase for the Celtec-EHC during the poisoning experiments was lower than 5 %. Consequently, the investigation of poison mitigation strategies was focused on H_2S. A 90 s offline air bleed was performed to mitigate the effect of operation with H_2S. During the air bleed, the O_2 from the air chemically oxidizes the adsorbed sulfur partially [Lope2011]. The EoT polarization performance of the Nafion-EHC remains 25 % increased compared to BoT and ECSA was still reduced by 50 % after the air bleed (Fig. 4.12 and 4.13). In comparison, Jackson et al. [Jack2020] could regain 40 to 50 % of the current when operated without poison after 15 min offline O_2 treatment. After performing CV-cleaning, during which the adsorbed sulfur or H_2S is electrochemically oxidized (Eqn. 4.12), the BoT polarization performance and the ECSA of the Nafion-EHC could be restored (Fig. 4.12 and 4.13).

$$Pt{-}S + 2\,H_2O \longrightarrow SO_2 + 4\,H^+ + 4\,e^- + Pt \tag{4.12}$$

For the Celtec-EHC operated with H_2S in H_2 at 120 °C, the ECSA and the polarization behavior were not completely recovered after 90 s air bleed, while at 160 °C the polarization behavior and ECSA was recovered by the air bleed (Fig. 4.12 and 4.13). When operating the Celtec-EHC with CH_4-diluted H_2S/H_2, the ECSA and polarization behavior were recovered by five CV-cycles (Fig. 4.12 and 4.16 (b)).

Increasing the operation temperature to 160 °C, as an online poison mitigation strategy, stabilizes the process and increases the voltage efficiency, which neglects heating, from 70 to 90 %, but decreases the energy efficiency, which considers heating, from 49 to 47 % (Fig. 4.16 (c)). Consequently, different poison mitigation strategies were analyzed regarding their effectiveness in stabilizing the process and process efficiency when operated with 3.5 ppm H_2S at 120 °C. Figure 4.16 presents the cell potential over time when air bleeds, and CV-cleaning are employed as mitigation strategies. Applying periodic air bleeds for 5 min every 90 min at 120 °C avoided oscillations of the system, and the mean cell potential was reduced compared to the non-mitigated operation. Nonetheless, the cell potential at the end of the mitigation cycles increased over the cycles, indicating a non-complete system recovery. This was also observed in the poisoning experiments, in which air bleeds at 120 °C could not completely recover the ECSA at 120 °C or lower temperatures. Periodic CV-cleaning every 90 min, however, stabilizes the operation of the Celtec-EHC. In Figure 4.16 (b), the cyclic voltammogram of the CV-cleaning is shown. The sulfur oxidation peak at potentials above 0.6 V decreases during the first three cycles until no significant changes can be observed in the CVs for cycles four and five. The reduction of oxidation charge and increase in PtO reduction charge in consecutive cycles indicate the removal of adsorbates. The energy efficiency and the voltage efficiency were improved by 14 % and 20 %, respectively, compared to the non-mitigated operation. However, Lopes et al. [Lope2011]

observed catalyst degradation when performing CVs for H_2S position mitigation. Additionally, Pt sulfides and oxides can be formed during CV cycling, which are difficult to remove [Seth2010]. The cyclic heating protocol, shown in Figure 4.16 (d), in which the cell was heated up to 160 °C periodically, although slowing the poisoning, did not yield a stable performance. Potentially, the operation time at 160 °C is too short to recover the poisoned catalyst surface sufficiently, and an exponential increase in cell potential is observed as the temperature drops back to 120 °C. Although this method could be optimized, applying it might cause accelerated component aging due to the imposed mechanical stress on the cell components from the temperature changes.

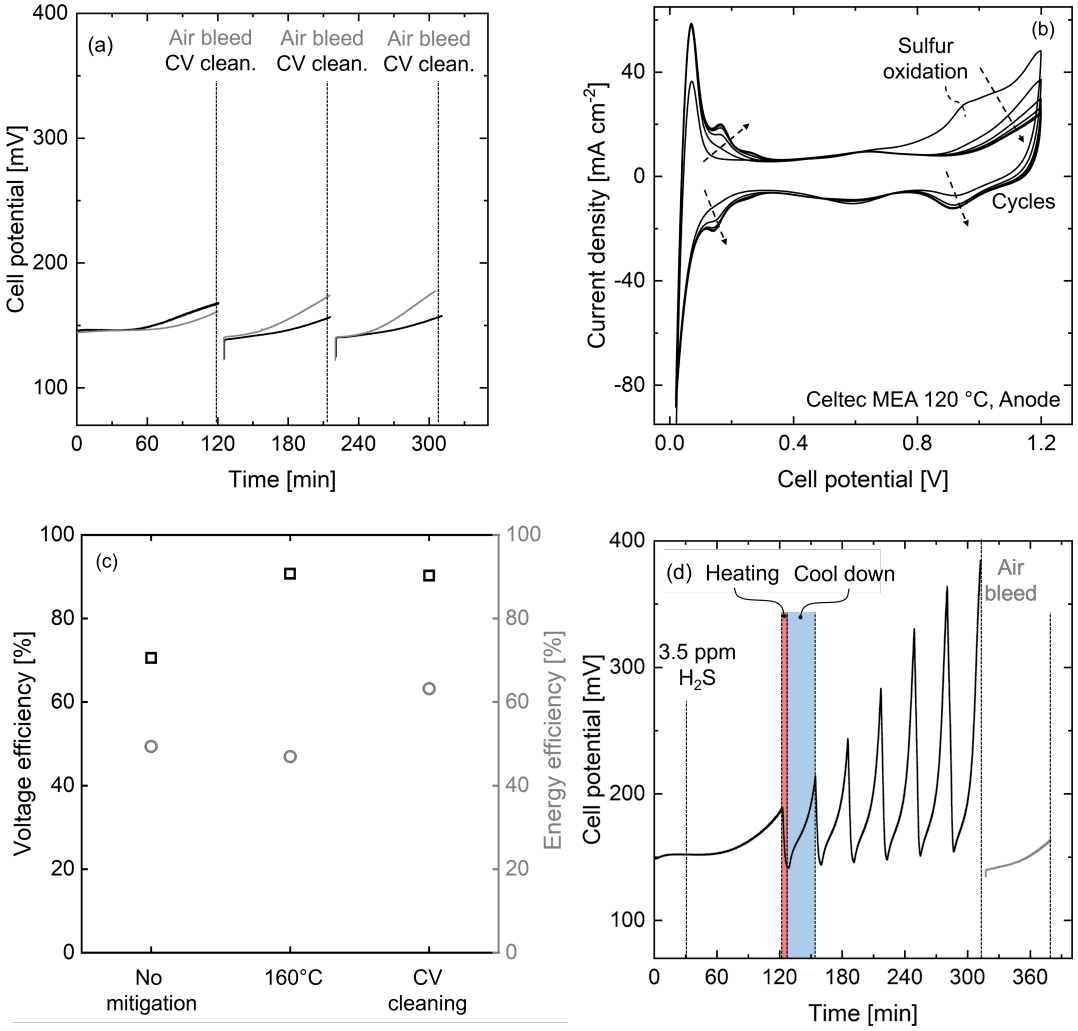

Figure 4.16: (a) Poison mitigation of 3.5 ppm H_2S in 44 vol% and 56 vol% CH_4 by 5 min air bleeds and five cycles CV-cleaning of a Celtec-EHC at 120 °C, 0.7 % RH; (b) CV of Celtec-EHC after poisoning with 3.5 ppm H_2S in 44 vol% H_2 and 56 vol% CH_4, (c) Voltage and energy efficiency of the mitigated and unmitigated operation, calculated from the average cell potential, not considering the downtime during mitigation; (d) Poison mitigation of 3.5 ppm H_2S in 44 vol% H_2 and 56 vol% CH_4 by cyclic heating to 160 °C.

4.3.6 H_2 withdrawal from natural gas

The Celtec-EHC was operated with H_2/natural gas H mixtures to evaluate the effect of higher hydrocarbons in the natural gas grid on the EHC. Figure 4.17 (a) shows the potential response when operating with 50 vol % natural gas H and the Nernst potential as reference. Upon introduction of the natural gas dilution, the mean potential increases steeply by 23.5 mV at 120 °C and

by 28.9 mV at 160 °C and then stabilizes. The Nernst potential for 50 vol % dilution of the feed is 12.7 mV at 120 °C and 13.9 mV at 160 °C. Consequently, the potential increase observed is not only caused by the partial pressure difference between the anode and cathode. During the discontinuation of the natural gas, the cell potential drops and stabilizes at 0.5 mV and 4 mV higher cell potentials than initially, at 120 °C and 160 °C, respectively. The higher remaining cell potential at 160 °C might be due to insufficient water supply to the cell because of equipment limitations (comp. Chap. 3.3.2). The relative humidity was halved upon the introduction of natural gas. In Figure 4.17 (b), the charge transfer resistance semicircle is enlarged at Eot, and a second semicircle at low frequencies appears, indicating mass transfer limitations at 120 °C. At 160 °C, in addition to an increase in charge and mass transfer resistance, the HFR increases by 10 mΩ cm^2. This increase in HFR could be caused by the reduced relative humidity or by poisoning of the natural gas components. Consequently, further investigations are needed to detangle the effects of humidity and poisoning.

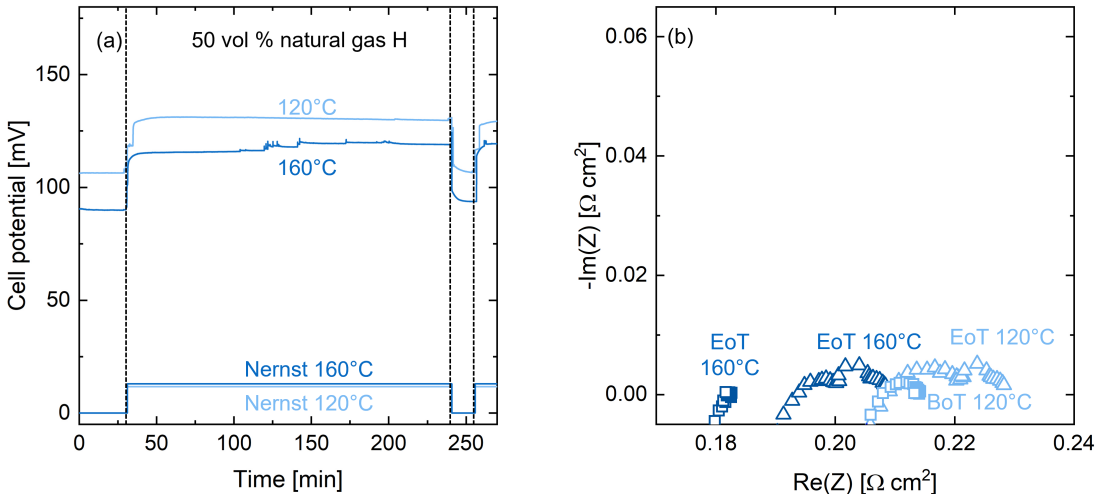

Figure 4.17: (a) Mean cell potential over time when operating the EHC with 50 vol % natural gas H equalized with H_2 feed at 120°C (light blue) and 0.8 % RH and 160°C (dark blue) 0.26 % RH, no poison was introduced for the first 30 min and from 240 to 255 min, 500 mA cm^{-2}, λ = 1.3 and Nernst potential for the respective gas mixture; (b) Nyquist plots displaying the impedance response of the EHC at 120°C (light blue) and 160°C (dark blue) before (BoT) and after (EoT) introducing 50 vol % natural gas H into the feed.

Upon introduction of 80 vol % natural gas, the mean potential, displayed in Figure 4.18, increases steeply by 61 mV at 120 °C and by 68.5 mV at 160 °C and then stabilizes for the operation at 120 °C, while at 160 °C the cell potential increases by 25 µV min^{-1}. The potential increase when diluting the feed with 80 vol % natural gas is 27.2 mV at 120 °C and by 30 mV at 160 °C. Upon discontinuation of the natural gas, the potential drops suddenly and reaches its initial value at 120 °C while 3 mV increase in cell potential is observed at 160 °C. The HFR increases at EoT at both temperatures, probably due to the very low humidification. The increase in charge transfer resistance and the second semi-circle, indicating mass transfer limitation probably due to concentration polarization, is more pronounced compared to the 50/50 mixture.

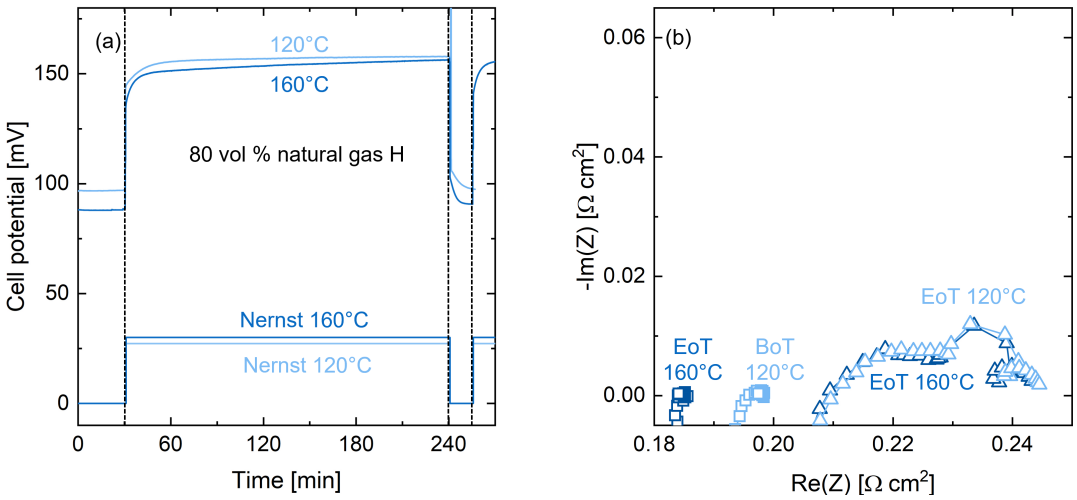

Figure 4.18: (a) Cell potential over time when operating the EHC with 80 vol % natural gas H equalized with H_2 feed at 120°C (light blue) and 0.33 % RH and 160°C (dark blue) 0.1 % RH, no poison was introduced for the first 30 min and from 240 to 255 min, 500 mA cm^{-2}, λ = 1.3 and Nernst potential for the respective gas mixture; (b) Nyquist plots displaying the impedance response of the EHC at 120°C (light blue) and 160°C (dark blue) before (BoT) and after (EoT) introducing 80 vol% natural gas H into the feed.

Figure 4.19 presents the cell potential during separation of H_2 from natural gas with 20 vol % H_2 and simultaneous compression to a differential pressure of 1 to 3 bar. The cell potential increases stepwise when the differential pressure over the cell increases, as expected from the increasing Nernst potential (grey line). The product gas of the electrochemical hydro-

gen compressor (EHC) was analyzed for trace impurities. The gas chromatography analysis determined a methane content in the product gas of below 10 ppm at 3 bar differential pressure. Due to the detection limit, other gases were not detected in the product gas.

Overall, combined compression and separation of H_2 from H_2/natural gas mixtures in shares representing the natural gas grid was demonstrated. The hydrocarbons in natural gas seem to have a minor poisoning effect, and most of the potential increase during the operation with the gas mixtures is probably caused by increased mass transfer resistance and possibly insufficient water supply. However, the operation of EHCs in real natural gas mixtures of different compositions should be investigated in more detail in future studies. Additionally, operation at higher differential pressures, being more representative of the application environment, and a thorough analysis of trace impurities in the product gas should be conducted.

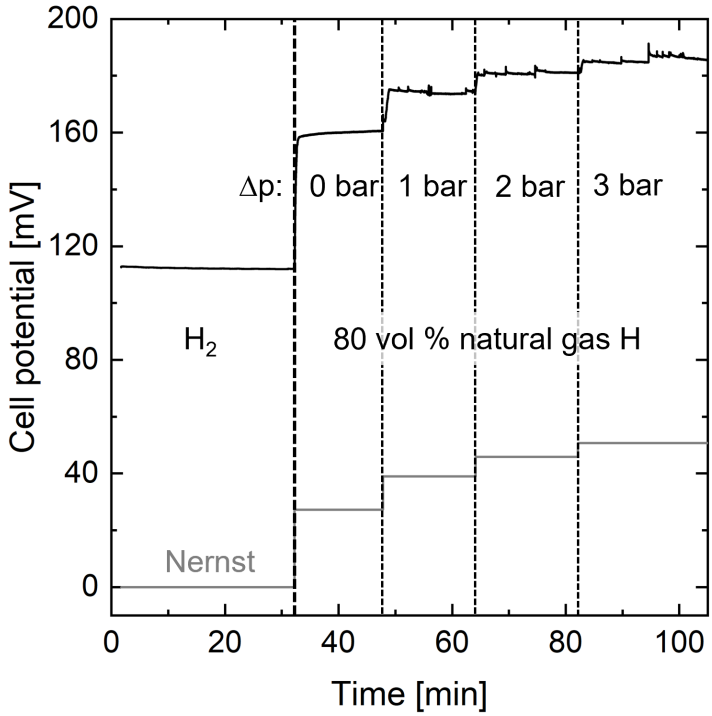

Figure 4.19: Equivalent Nernst potential (grey line) and measured cell potential (black line) over time with varying pressure difference (Δp) between cathode and anode at 120°C and 0.33% RH at 500 mAcm^{-2} and λ = 1.6.

4.4 Conclusion

We provided a comprehensive characterization of low (Nafion-EHC) and high-temperature EHC (Celtec-EHC) and elucidated the effect of CO_2, CO, NH_3, and H_2S on both EHCs' performance under galvanostatic operation. Strategies to reduce adverse effects of H_2S on the Celtec-EHC were compared regarding efficiency and effectiveness. For the Nafion-EHC, severe performance loss through poisoning was observed for CO_2, CO, and H_2S. The Celtec-EHC showed no significant performance decay when operated with CO_2 and CO at a moderate temperature of 120 °C. It was found that 14 ppm NH_3 will potentially lead to long-term performance degradation caused by ionomer alteration. The Celtec-EHC operation with 3.5 ppm H_2S in H_2 at 120 °C did not cause significant performance loss, although a reduction in active catalyst area could be detected. However, when substituting 56 % of the H_2 in the mixture by CH_4, the cell potential oscillated, and significant performance reduction was observed. When increasing the process temperature from 120 °C to 160 °C, the Celtec-EHC showed stable operation. However, the energy efficiency was impaired due to the increased need for heating power. Temperature pulsing and repeated air bleeds at 120 °C as mitigation strategies for the adverse effects of H_2S in diluted H_2 could not stabilize the performance. Repeated electro-oxidation by cyclic voltammetry leads to a stable performance with reduced poisoning, although long-term catalyst degradation needs to be evaluated.

This research underscores the applicability of EHC technologies in natural gas infrastructure while addressing operational challenges posed by contaminants like H_2S and NH_3. The comparative study of Nafion and Celtec-EHC establishes a foundation for comprehensive techno-economic evaluations. Future work should compare the long-term effects of different mitigation strategies, especially at higher current densities. Additionally, hybrid processes for separating the most detrimental contaminants H_2S and NH_3 before the EHC need to be assessed regarding economics.

5

A Tubular Electrochemical Hydrogen Compressor

Parts of this chapter have been published as:
Wibke Zängler, Mojtaba Mohseni, Robert Keller, Matthias Wessling
A tubular electrochemical hydrogen compressor, International Journal of Hydrogen Energy, 2024
DOI: 10.1016/j.ijhydene.2024.03.355

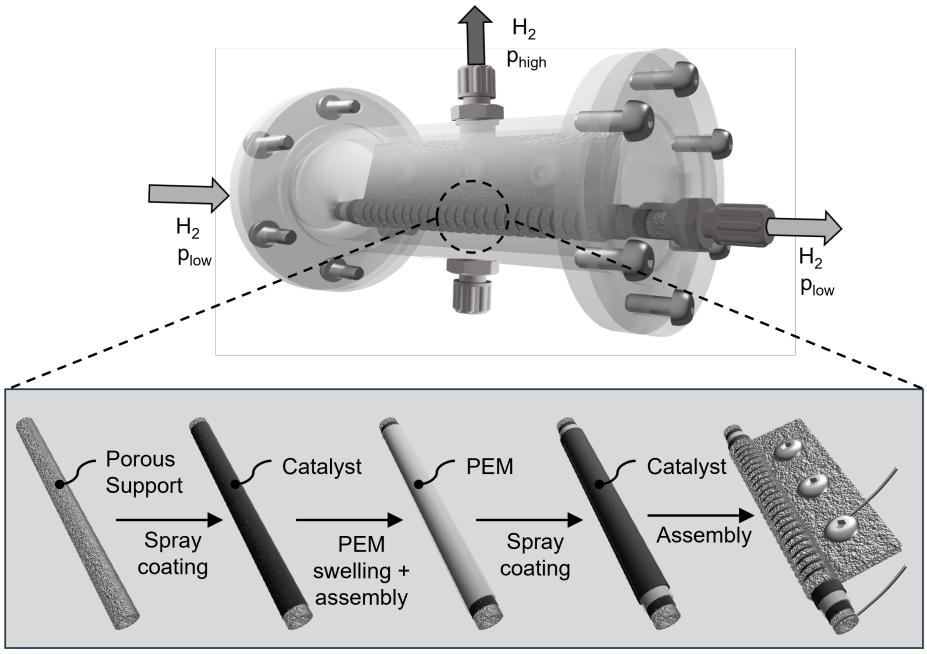

5.1 Introduction

Hydrogen is envisioned as the central energy vector in a defossilized economy [Staf2019; vdSpek2022]. By increasing the contribution of renewable energies, the role of hydrogen as chemical energy storage becomes increasingly important. Nevertheless, due to the low volumetric energy density of hydrogen, compression is of paramount importance in hydrogen processing [Abe2019; Yanx2019; Sdan2020; Nord2019]. Currently, mechanical compressors are used for hydrogen compression. These are usually positive replacement devices, e.g., membrane and piston compressors [Sdan2020]. Mechanical compression is a mature technology which offers single-stage compression ratios up to seven. However, it entails limitations such as vibration, moderate efficiency (45% [Sdan2020]) due to the isentropic compression principle, and high maintenance costs due to mechanical wear [Sdan2019b; Togh2020; Piva2024].

Alternatively, electrochemical hydrogen compressor (EHC) is an emerging technology to overcome the challenges of its mechanical counterpart because no moving parts are incorporated in the device. Additionally, theoretically unlimited compression ratios and efficient compression in small systems can be achieved, offering enhanced flexibility [Nord2019; Verm2021b; Rhan2020]. In addition, less theoretical compression work is required due to the isothermal compression [Zach2021].

The main challenges in EHC are membrane and catalyst materials, water mass transport to humidify the PEM, sealing, and cost [Durm2021; Zou2020; Gong2023; Chou2020]. State-of-the-art catalysts in EHC are platinum group metals, which are costly and are susceptible to catalyst poisoning in media containing impurities, e.g., by CO [Trég2020]. Most ion exchange membrane materials used in EHC must be sufficiently humidified to ensure ion conductivity, which is challenging to maintain in a process with a gaseous reactant and product such as EHC [Gong2023]. Moreover, the back-permeation of hydrogen through the ion exchange membrane is limiting the process efficiency of EHC. Additionally, sealing concepts for high-pressure applications are challenging [Ayku2023].

While there have been some studies on catalyst [Wu2012; Jack2020] and membrane [Rico2018; Zou2023; Maxw2023] development for EHC, research on process aspects e.g. cell geometry, flow field, and gas diffusion layer design, sealings, and reactor designs has been limited [Capo2022; Casa2008].

Tubular cell designs offer advantages in sealing length, surface-to-volume ratio, and mass transport [Laub2022; Cour2003; Mohs2023; Webe2023]. Additionally, tubular systems are intrinsically well-suited for differential pressure applications such as EHC. Additionally, uniform pressure distribution on the cell compared to planar ones can lead to lower ohmic losses and, consequently, less stress on the membrane and mechanical support for the PEM in tubular cells [Zou2020; Ward2011].

Despite these advantages, tubular cell concepts, especially including membrane electrode assemblies, have been sparsely realized [Laub2022; Rabi2022; Dong2021]. Laube et al. [Laub2022] developed a tubular membrane electrode assembly for PEM-electrolyzers, which can be fabricated through cost-effective and in-line co-extrusion. Recently, they achieved 450 mA cm^{-2} at 2 in their tubular PEM water electrolyzer [Laub2023]. Dong et al. [Dong2021] developed a solid electrolyte tubular cell for CO_2 electroreduction using a SN-Cu hollow fiber electrode, reporting a cell potential of -1.4 V at 0.11 mA cm^{-2} for acetaldehyde and acetone production.
However, in both studies, liquid electrolytes were employed. To date, no tubular concepts for all gas phase electrochemistry, e.g., EHC, have been presented. These pose specific challenges as mass transport to and from the catalytic site.

This chapter introduces the first all-tubular EHC with a membrane electrode assembly comprising a 3D-printed anode and a catalyst-coated membrane. The EHC's electrochemical performance was examined in a tubular module via linear sweep, multi-chronopotentiometry, and electrochemical impedance spectroscopy. The compression performance was tested in short-term stability experiments. Additionally, a 2D model of a tubular and planar EHC was developed for performance investigation.

5.2 Materials and Methods

Pt/C nanoparticles 40% Pt on carbon black and Fumion 1005, 5% suspension in n-propanol were purchased from Quintech. Nafion™ tubes with 2.18 mm inner diameter and 305 µm membrane thickness were supplied by Permapure.

5.2.1 Anode fabrication

The porous tubular anodes of 8 cm length, 3.3 mm outer diameter, and 1 mm wall thickness were produced by metal selective laser melting (SLM) using a selective laser fusion printer (Sisma MySint100 PM), enabling tunable pore size and porosity. Stainless steel powder 1.4404 (AISI 316L, particle size $<$60 µm) was employed as substrate. The anode was produced with a radial pore pattern, which was achieved by scan line patterning developed by Limper et al. [Limp2022]. The SEM image in Figure 5.1 shows the radial pore pattern of the shell side and cross section of the tubular porous support. The pore size distribution of the herein used anode is presented in Figure S1. The pore size distribution and morphology of the anode were measured via gas-liquid porosimetry (POROLOX 1000, Porometer NV) and scanning electron microscopy (SEM) (TM3030plus, Hitachi), respectively.

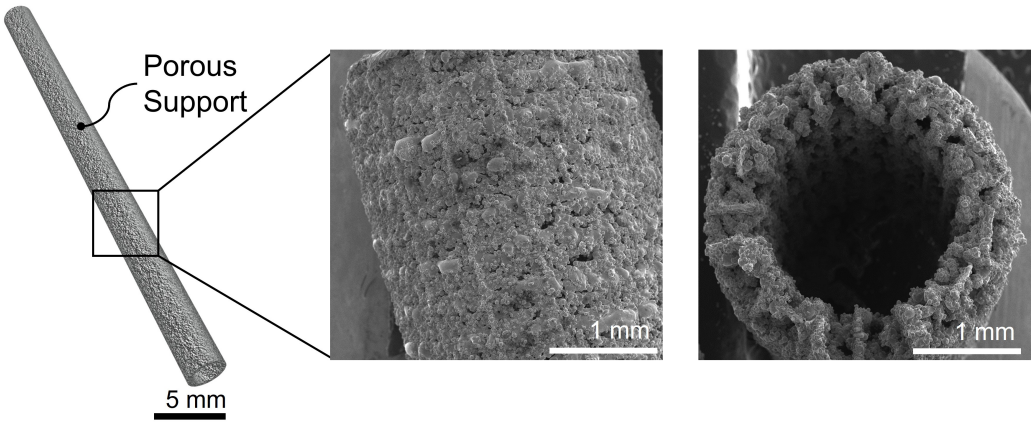

Figure 5.1: SEM image of porous support shell side and cross section.

5.2.2 Catalyst-coated membrane fabrication and MEA assembly

The fabrication process of the tubular MEA is displayed in Figure 5.2. The catalyst ink was prepared by sonicating a mixture of 14 mg Pt/C nanoparticles, 2.3 mL isopropanol, 100 µL Fumion 1005 suspension for 30 min (amounts for one 8 cm tube). First, the ink was airbrushed on the tubular anode via manual spray coating (Harder & Steinbeck, Evolution Infinity). The theoretical catalyst loading of the anode and cathode is 0.7 mg cm^{-2}. The catalyst layer was dried for two hours at a vacuum of 50 mbar and a temperature 80 °C. Subsequently, the Nafion™ tube was soaked in 80% methanol in DI-water for at least twelve hours, then slid on the tubular anode and dried at ambient conditions for 24 hours, which led to a firm shrinkage of the membrane on the anode. Afterward, the cathode catalyst layer was sprayed on the outer surface of the membrane using the same parameters as for the anode.

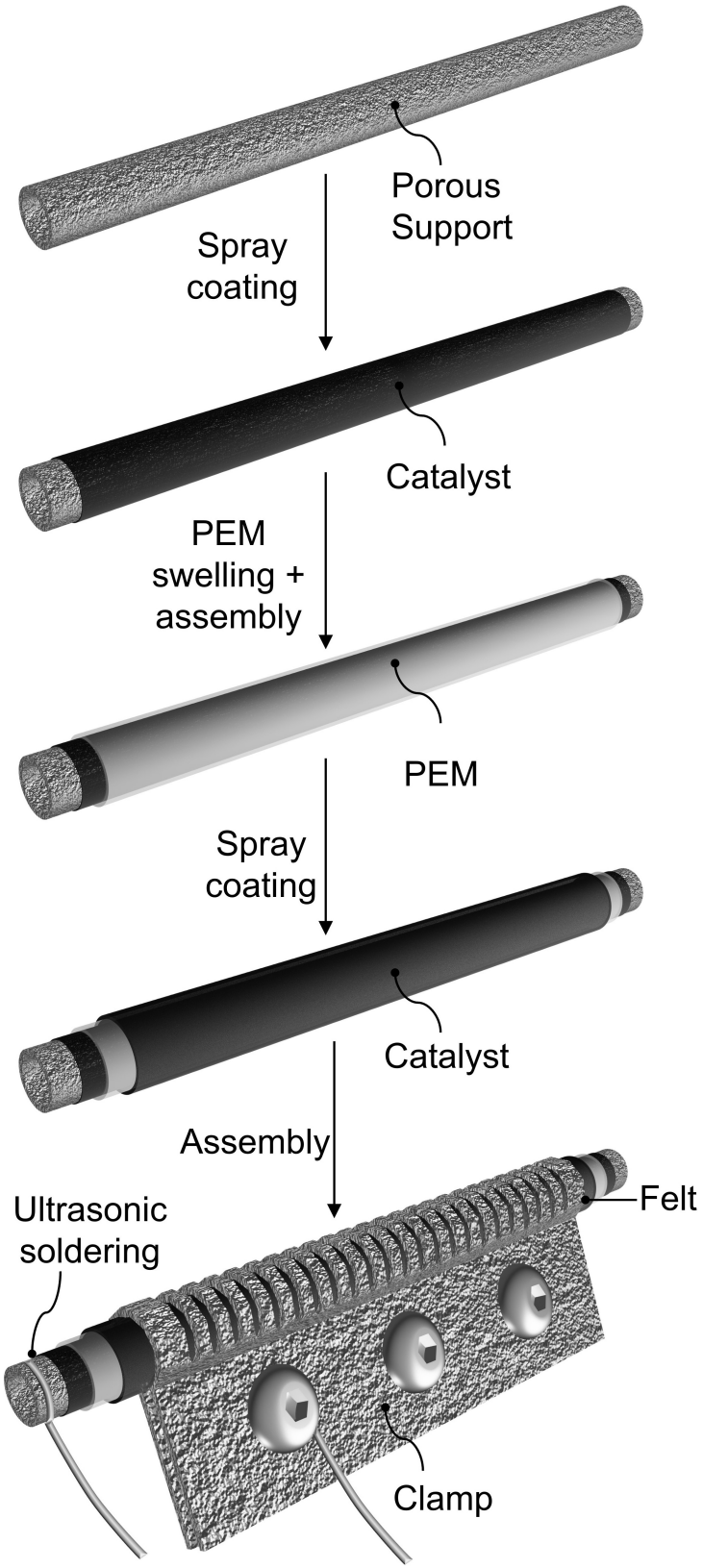

Figure 5.2: Assembly of tubular electrochemical hydrogen compressors. Porous support prepared by 3D-printing. Anode and cathode catalyst layers are prepared by manual spray coating Pt/C catalyst ink. Anode and cathode catalysts are separated by a commercial Nafion™ tube. The cathode is contacted via a stainless steel clamp.

5.2.3 Tubular EHC assembly

The tubular anode was contacted via a silver-coated copper wire as the current collector by ultrasonic soldering (MBR electronics). The cathode of the tubular membrane electrode assembly was contacted by titanium felt (Bekaert, 20 µm fiber diameter, 400 g m^{-2} weight, nominal porosity of 50 %) and a stainless steel clamp (3D-printed), as shown in Figure 5.1. Three bolts ensure the tightness of the clamp for electrical contacting.

The membrane electrode assembly was potted into polyethylene tubing using two component epoxy resin (UHU Plus Epoxy Ultra Quick) and then installed into the reactor. All experiments were conducted in an in-house fabricated tubular reactor, depicted in Figure 5.3.

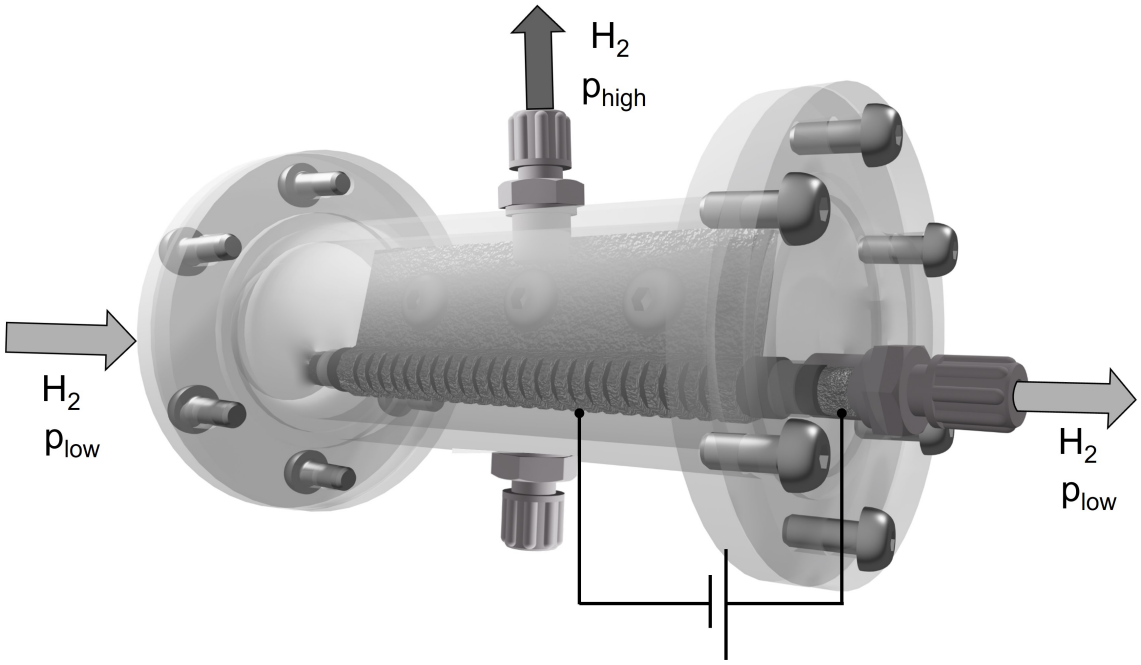

Figure 5.3: Reactor for the operation of tubular EHC.

5.2.4 Electrochemical experiments and analytics

All experiments were executed in a two electrode set-up and at room temperature. Mass flow controllers (Series 358, Analyt MTC) were used to control the gas supply to the cell. The relative humidity was monitored by a humidity sensor (UFT75-ST1, MELTEC). The back pressure on the cathode side was regulated by a check valve (Spring loaded back pressure regulator,

Swagelok), if required, and monitored (A-10, WIKA).

Before supplying hydrogen, the anode and cathode compartments of the reactor were flushed with nitrogen for safety reasons. For preconditioning, humidified hydrogen (100% RH) with a flow rate of 50 N mL min^{-1} was fed to the anode, starting 20 min in advance of each experiment to ensure saturation of the compartment with hydrogen.

Electrochemical experiments were conducted by a biologic VSP potentiostat with a booster (VMP3B-20) and impedance module. Polarization curves were obtained by multi-chronopotentiometry experiments with a step duration of 40 min. The mean value of the last five minutes of the current step is displayed in the polarization curve. All electrochemical impedance measurements were performed at OCV with 10 mV perturbation and six points per decade. Electrochemical impedance spectra were measured from 10 k Hz to 1 k Hz before an experimental series and from 10 k Hz to 10 Hz for all other impedance measurements. Linear sweep voltammetry (LSV) measurements were performed with 0.5 mV s^{-1} scan rate. The ohmic resistance for the LSV was determined at 5 k Hz, and 85% iR-compensation was considered. Unless otherwise mentioned, all data is presented as the mean value of duplicate experiments, with the standard deviation as the error bar.

5.3 Model formulation

2D models for a planar and a tubular EHC were developed in the simulation and computation software Matlab to investigate hydrogen separation and compression with EHCs. The main features of the model are illustrated in Figure 5.5. The inlet stream is a ternary gas mixture of hydrogen, methane and water vapor. The cell was modeled using the following sub-models. The EHC cell is symmetrically built, as illustrated in Figure 5.5. The anode feed side and the cathode product stream were modeled as a bulk phase with constant feed concentration. The gaseous mass transport in porous gas diffusion layers on the anode and cathode side was modeled. The active catalyst layer was implemented as an infinitesimally thin layer accommodating the faradic reaction. The mass transport resistance of the catalyst layer was modeled in the gas diffusion layer regime. Mass transport in the proton exchange membrane was described using the solution-diffusion model. Water transport in the membrane was included in the model. The proton conductivity, depending on water activity in the membrane, was computed. The input parameters are the molar feed flow rate, molar share of H_2 and H_2O in the feed and product gas and the anode and cathode pressure p_a, p_c.

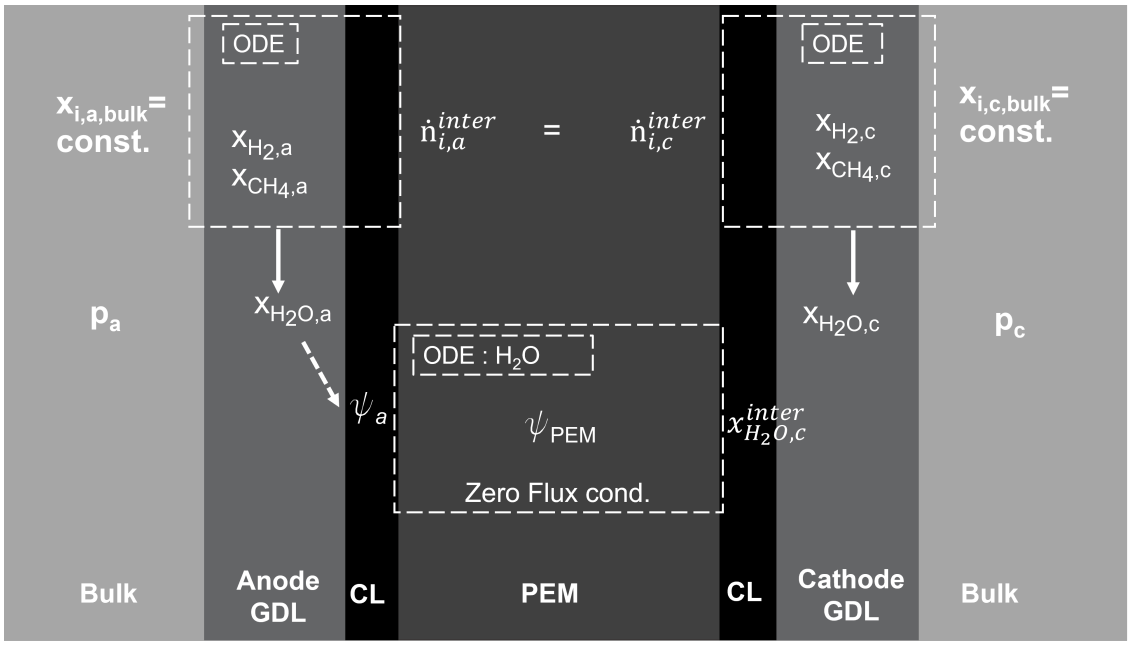

Figure 5.4: Simplified illustration of an EHC with the input parameters and boundary conditions. The variables in thick print are inputs. A solid line means "calculated from", a dash dot line "solved by ODE" and a dashed line "determined by empirical formula".

The model determines the cell potential with varying current density and the substance mole fractions in steady state in r- and z-direction. Additionally, the model allows parameter examination for temperatures, cathode pressures, inlet molar flows, current densities, membrane thickness and electrode porosity.

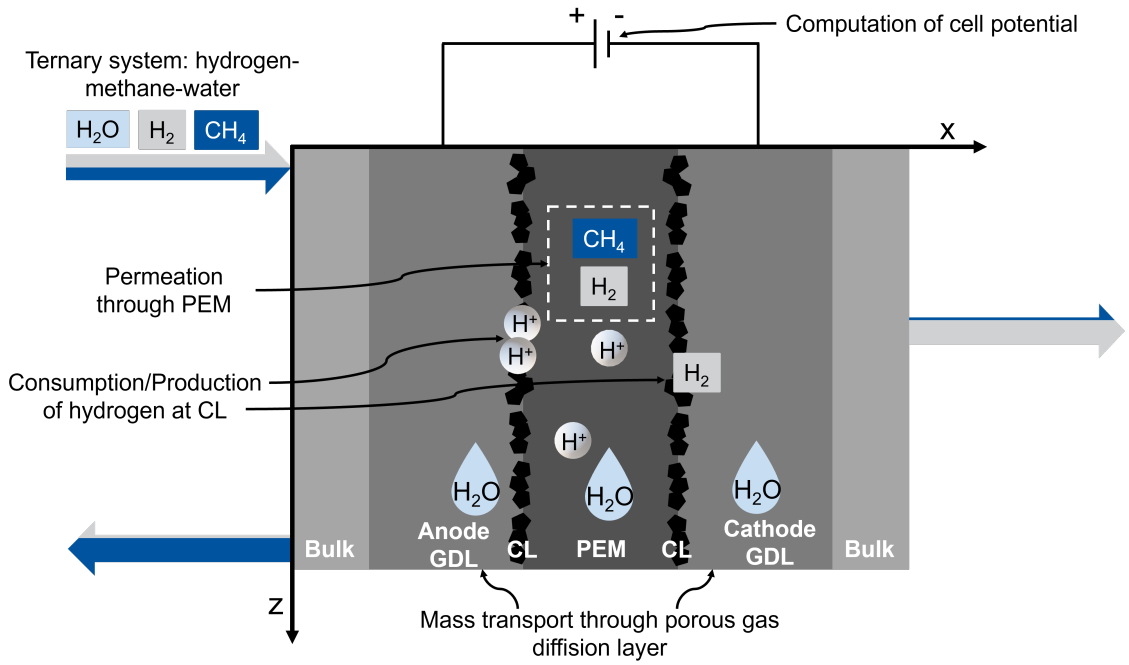

Figure 5.5: Illustration of the main features considered by the model for the planar cell example.

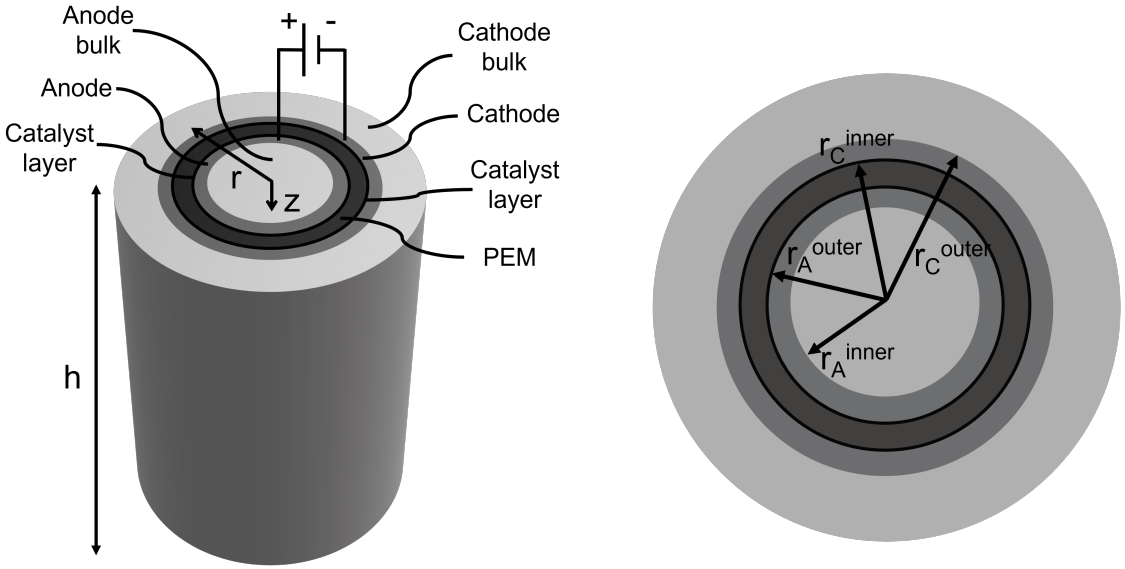

Figure 5.6: Illustration of the tubular EHC model.

5.3.1 Model assumptions

The model is based on the following assumptions:

- The process is at steady state ($\frac{\partial}{\partial t} = 0$)

- The temperature in the cell is constant
- The pressure at the anode and cathode is constant
- Hydrogen and methane are treated as ideal gases
- Only the influence of the membrane proton conductivity is considered in the calculation of the ohmic overvoltage
- Only diffusion in x-direction for the planar cell and in the r-direction for the tubular cell is considered
- Advection is neglected
- The catalyst layer is considered as an infinitely thin interface layer, thus $r_a^{outer} = r_{PEM}^{inner} = r_a^{CL}$ and $r_c^{inner} = r_{PEM}^{outer} = r_c^{CL}$
- The cathode bulk is ideally-mixed
- The current along the electrodes is constant
- Precipitating water has no influence on mass transport

5.3.2 Porous gas diffusion layer

The gas diffusion layers borders the bulk inlet and outlet streams and the catalyst layer. In the gas diffusion layer, only gaseous mass transport of the modeled components occurs.

The mass transport of a species i as the molar flux $\dot{n}_i$ in the gas compartments of the electrochemical cell is described by the Maxwell-Stefan equation with the concentration gradient $\frac{\partial c_i}{\partial t}$, the concentration c_i and the source/sink term S_i^m [Kris1997].

$$\frac{\partial c_i}{\partial t} + \nabla \dot{n}_i = S_i^m \tag{5.1}$$

The flux of a species i is composed of a diffusion part expressed by use of Fick's law and an advection part, as seen in Equation 5.2. The advection

term (second term) is neglected in the model. Additionally, no production or consumption of a species occurs in the porous gas diffusion layer of the anode and cathode; thus, the source/sink term can be omitted.

$$\dot{n}_i = -D_i \cdot \nabla C_i + C_i \cdot u \tag{5.2}$$

For a planar EHC, the nabla operator is simplified to a partial derivative in the x-direction.

$$\dot{n}_i = -D_i \cdot \frac{\partial C_i}{\partial x} \tag{5.3}$$

For a tubular EHC, the general equation can be simplified to a partial derivative in radial direction.

$$\dot{n}_i = -D_i \cdot \frac{\partial C_i}{\partial r} \tag{5.4}$$

The gaseous mass transport in the porous gas diffusion layer was modeled considering a diffusion coefficient for multi-component mass transport according to Rieckmann et al. [Riec1997] with the binary mass diffusivities, $D_{i,j}$ and $D_{i,k}$, the Knudsen diffusion coefficient $D_{Kn,i}$, and the mole fraction of the respective component x.

$$D_i = \left[\frac{1}{D_{Kn,i}} + \frac{x_j}{D_{i,j}} + \frac{x_k}{D_{i,k}} \right]^{-1} \tag{5.5}$$

The binary diffusion coefficients $D^0_{i,j}(T_0, p_0)$ were computed as a function of temperature and pressure based on the diffusion coefficient at a reference temperature T_0 and reference pressure p_0 [Sdan2020].

$$D_{i,j}(T, p) = D^0_{i,j}(T_0, p_0) \cdot \frac{p_0}{p} \cdot \left(\frac{T}{T_0} \right)^{\frac{3}{2}} \tag{5.6}$$

The Knudsen diffusion coefficient is computed by the following equation with the pore diameter d_{pore} and the molar mass of component i M_i [Yuan2014].

$$D_{Kn,i}(T) = \frac{d_{pore}}{3} \cdot \sqrt{\frac{8 \cdot R \cdot T}{\pi \cdot M_i}} \tag{5.7}$$

The Bruggeman correlation delineates the effective diffusion coefficient in porous media, based on the porosity ϵ and tortuosity τ [Sabh2019]. The relation $\tau = \epsilon^{-0.5}$ was assumed.

$$D_i^{eff}(p,T) = \frac{\epsilon}{\tau} \cdot D_i(p,T) = \epsilon^{\frac{3}{2}} \cdot D_i(p,T) \tag{5.8}$$

5.3.3 Catalyst layer

The catalyst layer was modeled as a layer without thickness and thus is not resolved in the model. Consequently, the mass transport resistance of the porous catalyst was added to the equation modeling the gas diffusion layer. having a fixed mass transport resistance. In the catalyst layers, the faradaic reaction of hydrogen oxidation on the anode and hydrogen evolution on the cathode take place.

The hydrogen catalyst layer mass transport resistance R_{CL} was set to 30 s/m for a catalyst layer with a thickness L_{CL} of 8 µm [Mu2019]. The resistance was chosen to be 80 % of the total hydrogen mass transport resistance. The catalyst layer resistance is included in the hydrogen diffusion coefficient of the gas diffusion layer as a parallel resistance, as the catalyst layer is not resolved in the model.

$$D_{H_2}^{eff} = \frac{\delta}{\frac{\delta - \delta_{CL}}{D_{H_2,GDL}^{eff}} + R_{CL}} \tag{5.9}$$

The temperature dependence was approximated with the temperature re-

lationship of the diffusion coefficients in Equation 5.8 with $T_0 = 318K$.

$$R_{CL} = 30\frac{s}{m} \cdot \left(\frac{T_0}{T}\right)^{\frac{3}{2}} \tag{5.10}$$

The faradaic reactions at the anode and cathode were modeled with Faraday's law (compare section 2.3), which describes the correlation of the current density j and the amount of hydrogen consumed or produced at the catalyst interfaces. The anodic current density is defined as negative, and the cathodic current density is defined as positive as proposed by Bard et al. [Bard2001] ($j = j_c = j_a$).

$$j = \frac{I}{A} = \frac{z \cdot F \cdot \dot{N}_{H_2}}{A} \tag{5.11}$$

For a tubular cell, the current density is a function of the radius r:

$$j = \frac{I}{2 \cdot \pi \cdot r \cdot H} \tag{5.12}$$

5.3.4 Ion exchange membrane

The solution-diffusion model was used to describe the permeation of hydrogen and methane through the dense membrane. The back diffusion flux $\dot{n}_{b,i}$ of a gaseous component i across the membrane, assuming a constant concentration profile and constant diffusion coefficients for hydrogen and methane along the membrane thickness L, can be described with the following equation.

$$\dot{n}_{b,i} = D_i \cdot \frac{\Delta C_i}{L} \tag{5.13}$$

The relation between the partial pressure and the molar fraction of the component is given by Dalton's law:

$$p_i = p \cdot x_i \tag{5.14}$$

Henry's law correlates the partial pressure of a component with its concentration in the liquid phase using the Henry constant S_i. The permeability coefficient P_i is defined in Equation 2.8. The permeability coefficient values of Mukaddam et al. [Muka2016], obtained at 2 atm and 35°C for dry Nafion™, were used in the model.

The global water flux $\dot{n}_{H_2O}^{Membrane}$ for a planar EHC is described by the following equation with ψ the membrane water content, ζ the electro-osmotic drag coefficient (the number of water molecules dragged per proton), $D_{H_2O}^{Membrane}$ the diffusion coefficient of water across the membrane, ρ_{dry} the dry membrane density and EW the membrane equivalent weight [Sdan2020].

$$\dot{n}_{H_2O}^{Membrane} = \zeta \cdot \frac{j}{F} - D_{H_2O}^{Membrane} \cdot \frac{\rho_{dry}}{EW} \cdot \frac{\partial \psi}{\partial x} \tag{5.15}$$

And for a tubular EHC:

$$\dot{n}_{H_2O}^{Membrane} = \zeta \cdot \frac{j}{F} - D_{H_2O}^{Membrane} \cdot \frac{\rho_{dry}}{EW} \cdot \frac{\partial \psi}{\partial r} \tag{5.16}$$

The membrane water content can also be expressed as membrane water concentration $C_{H_20}^{Membrane}$:

$$\psi = C_{H_20}^{Membrane} \cdot \frac{EW}{\rho_{dry}} \tag{5.17}$$

The electro-osmotic drag coefficient is computed as a function of the membrane water content, as described in Springer et al. [Spri1991] for Nafion™117 at 80°C:

$$\zeta(\psi) = 2.5 \cdot \frac{\psi}{22} \tag{5.18}$$

The diffusion coefficient of water across the membrane is modeled using

an empirical formula from Costamagna et al. [Cost2001]:

$$D_{H_2O}^{Membrane}(\psi) = (5.1 - 0.66 \cdot \psi + 5.2 \cdot 10^{-2} \cdot \psi^2 - 1.3 \cdot 10^{-3} \cdot \psi^3) \cdot 10^{-6} \cdot \exp\left(2416 \cdot \left(\frac{1}{303} - \frac{1}{T}\right)\right) \tag{5.19}$$

The membrane water content ψ at the membrane-electrode interface was computed as a function of water activity a_{H_2O} in the gas phase using the empirical relation in Springer et al. [Spri1991] for Nafion™117 at 30°C.

$$\psi = 0.043 + 17.81 \cdot a_{H_2O} - 39.85 \cdot a_{H_2O}^2 + 36 \cdot a_{H_2O}^3 \tag{5.20}$$

This relation is only valid for activities in the range 0 to 1. For water activities greater than 1, water condensation occurs, and a case distinction is introduced for the calculation of the membrane water content at the electrode-membrane interface, as presented by Toghyani et al. [Togh2020].

$$\psi = 14 + 1.4 \cdot (a_{H_2O} - 1) \qquad 1 < a_{H_2O} \leq 3 \tag{5.21}$$

$$\psi = 16.8 \qquad a_{H_2O} > 3 \tag{5.22}$$

The relative humidity *RH* corresponds to the water activity in the gas phase with a factor of 100 with the partial pressure p_{H_2O} of water and the water vapor pressure $p_{H_20}^{vap}$.

$$RH = 100 \cdot a_{H_2O} = 100 \cdot \frac{p_{H_2O}}{p_{H_20}^{vap}} \tag{5.23}$$

The water vapor pressure as a function of temperature *T* was determined using the Antoine equation with the parameters $A = 6.20963$, $B = 2354.731$ and $C = 7.559$ [Lins].

$$p_{H_20}^{vap} = 10^{A - \frac{B}{C+T}} \cdot 10^5 \tag{5.24}$$

The partial pressure of water at the anode-membrane interface is obtained from the mole fraction closure condition (Equation 5.33), using Dal-

ton's law.

The membrane water content ψ_a computed from Equation 5.20 and Equation 5.23 is used as the left boundary condition in the differential equation of membrane water mass transport. The water content at the membrane cathode interface is defined as the right boundary. The sum of all component fluxes in the proton exchange membrane (PEM) is equal to zero.

5.3.5 Potential calculation

The cell potential was calculated as the sum of Nernst potential, Ohmic and concentration overpotential as presented in Section 2.3.

The activation overpotential is neglected due the fast reaction kinetics of the hydrogen oxidation reaction (HOR) and the hydrogen evolution reaction (HER) [Sdan2019b; Strö2002].

The ohmic overpotential can be described as a function of the membrane proton conductivity σ and membrane position x or r in the planar and tubular reactor, respectively by:

$$j = \sigma \cdot \frac{dE_{Ohmic}}{dx} \tag{5.25}$$

$$j = \sigma \cdot \frac{dE_{Ohmic}}{dr} \tag{5.26}$$

The membrane proton conductivity of Nafion™117 can be expressed by Equation 5.27, obtained in Springer et al. [Spri1991], as a function of the temperature T and the membrane water content ψ, for $\psi > 1$:

$$\sigma(T, \psi) = 100 \cdot \exp\left(1268 \cdot \left(\frac{1}{303} - \frac{1}{T}\right)\right) \cdot (0.005139 \cdot \psi - 0.00326) \tag{5.27}$$

The concentration overpotential occurs due to mass transport limiting effects and is computed by the following equation with the limiting current density at the anode $j_{L,a}$ and the current density at the anode j_a [Bard2001]. The cathode mass transport limitation was neglected in the model, which is standard practice in the literature, and initial computation showed the cath-

ode limiting current to be significantly higher than the anode limiting current.

$$E_{Conc,a/c} = \pm \frac{R \cdot T}{n \cdot F} \cdot \log \frac{j_{L,a} - j_a}{j_{L,a}} \tag{5.28}$$

The mass transport differential equation of the gas diffusion layers (Section 5.3.2) was solved in a "while loop" to compute the limiting current density. The current density was increased gradually after each calculation loop. The calculation process was aborted when reaching a mole fraction of less than 0.00277 (at 1 bar and 333.15 K) at the anode-membrane interface of the last sub-element, and the current density was given as output. This method results in a slight inaccuracy due to the selected current steps and the termination condition. Furthermore, calculation time is high.

5.3.6 Boundary and closing conditions

The model structure, including boundary and closing conditions is illustrated in Figure 5.4. For both gas diffusion layers, the bulk mole fractions of hydrogen and water are fixed.

$$x^{bulk}_{a/c,H_2} = \frac{C^{bulk}_{a/c,H_2} \cdot R \cdot T}{p_{a/c}} = const. \tag{5.29}$$

$$x^{bulk}_{a/c,H_20} = \frac{p^{bulk}_{a/c,H_20}}{p_{a/c}} = const. \tag{5.30}$$

The flux of H_2 and CH_4 at electrode-membrane interfaces were set as the Neumann boundary conditions.

$$\dot{n}^{inter}_{a,H_2} = \dot{n}^{inter}_{c,H_2} \tag{5.31}$$

$$\dot{n}^{inter}_{a,CH_4} = \dot{n}^{inter}_{c,CH_4} \tag{5.32}$$

The mole fraction of the n^{th} substance was calculated with the mole frac-

tion closure condition.

$$\sum_i x_i = 1 \tag{5.33}$$

5.3.7 Discretization of the Cell

A 2D model was developed to model the planar and tubular EHC. The cell was discretized into n_z sub elements of the height dz along the z-axis, as illustrated on the example of mass transport in Figure 5.7. Mass transport and electrochemical overpotentials are solved separately in x- or r-direction. Coupling between the domains in x- or r-direction is achieved through boundary conditions.

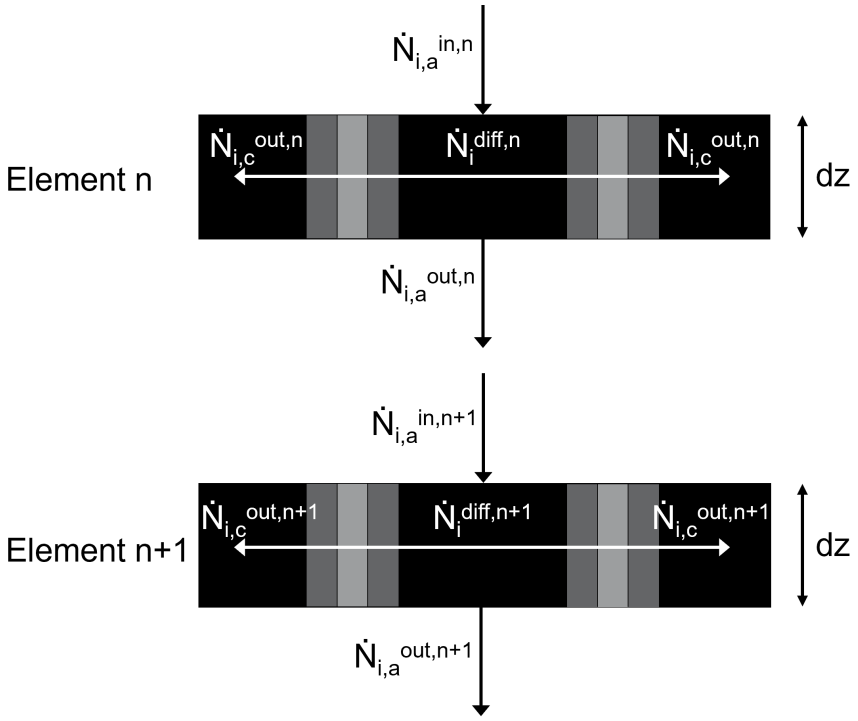

Figure 5.7: Discretization in inlet flow direction exemplary for the mass balance of sub elements in a tubular EHC.

The Nernst voltage of the cell is determined by averaging the Nernst voltages of all sub elements. The ohmic overvoltage of a sub element as well

as of the entire cell is determined as follows:

$$E^{n}_{Ohmic} = \int_{0}^{L} \frac{j}{\sigma(\lambda(x)) \cdot n_z} dx \tag{5.34}$$

$$E^{n}_{Ohmic} = \int_{r_a^{outer}}^{r_c^{inner}} \frac{i}{2 \cdot \pi \cdot dz \cdot \sigma(\lambda(r)) \cdot r} \cdot dr \tag{5.35}$$

$$E_{Ohmic} = \sum_{n=0}^{n_z} E^{n}_{Ohmic} \tag{5.36}$$

Moreover, by determining the limiting current density of each sub-element, the concentration polarization overpotential can be computed. To determine the concentration polarization potential of the whole cell, the concentration polarization of the sub elements are averaged.

5.3.8 Efficiency and Recovery Factor

The power efficiency η of an electrochemical hydrogen compressor was calculated as the quotient of the power requirement of a thermodynamically ideal compressor P_{ideal} and the actual power requirement P_{actual} [Chou2020]:

$$\eta = \frac{P_{ideal}}{P_{actual}} \tag{5.37}$$

Assuming isothermal conditions, the ideal power requirement was computed by [Chou2020]:

$$P_{ideal} = \dot{N}_{net,H_2} \cdot R \cdot T \cdot \log \frac{p_c}{p_a} \tag{5.38}$$

The net hydrogen flow rate $\dot{N}_{net,H_2}$ is the difference of the rate of moles oxidized $\dot{N}_{f,H_2}$ according to Faraday's law and the rate of moles diffusing back $\dot{N}_{b,H_2}$:

$$\dot{N}_{net,H_2} = \dot{N}_{f,H_2} - \dot{N}_{b,H_2} \tag{5.39}$$

The actual power requirement was calculated by [Chou2020]:

$$P_{actual} = z \cdot F \cdot E_{Electrode} \cdot \dot{N}_{f.H_2} = I \cdot E_{Electrode} \tag{5.40}$$

The Hydrogen Recovery Factor (HRF) was calculated as the quotient of the outlet $\dot{N}_{H_2}^{outlet}$ and the inlet hydrogen flux $\dot{N}_{H_2}^{inlet}$

$$HRF = \frac{\dot{N}_{H_2}^{outlet}}{\dot{N}_{H_2}^{inlet}} \tag{5.41}$$

5.4 Results and Discussion

5.4.1 Design concept

Electrical contacting is a significant challenge for small, tubular designs. For adequate contact, sufficient pressure must be applied on the membrane electrode assembly, requiring high mechanical stability of the centered anode as it bears the applied force. The herein-employed 3D-printed metal anode with tunable porosity provides sufficient mechanical stability. The tailor-made clamping device also ensures a uniform pressure distribution from the cathode to the membrane and anode. Additionally, the design facilitates self-reinforcement, as the pressurized side of the cell is the cathode side. A pressure gradient between the cathode and anode develops upon electrochemical hydrogen compression, pressing the MEA onto the rigid anode support.

5.4.2 Electrochemical characterization

The tubular EHC was characterized electrochemically by linear sweep voltammetry, multi-chronopotentiometry, and electrochemical impedance spectroscopy. Figure 5.8 shows the iR-corrected and non-corrected polarization curve of the tubular EHC as well as the results from the multi-chronopotentiometry. Linear behavior of the polarization curves is observed until 60 mA cm^{-2}, followed by an exponential increase at higher current densities. The current-voltage behavior is validated by the results from the multi-chronopotentiometry (square symbols). The limiting current density under non-pressurized operation conditions reached approximately 90 mA cm^{-2}.

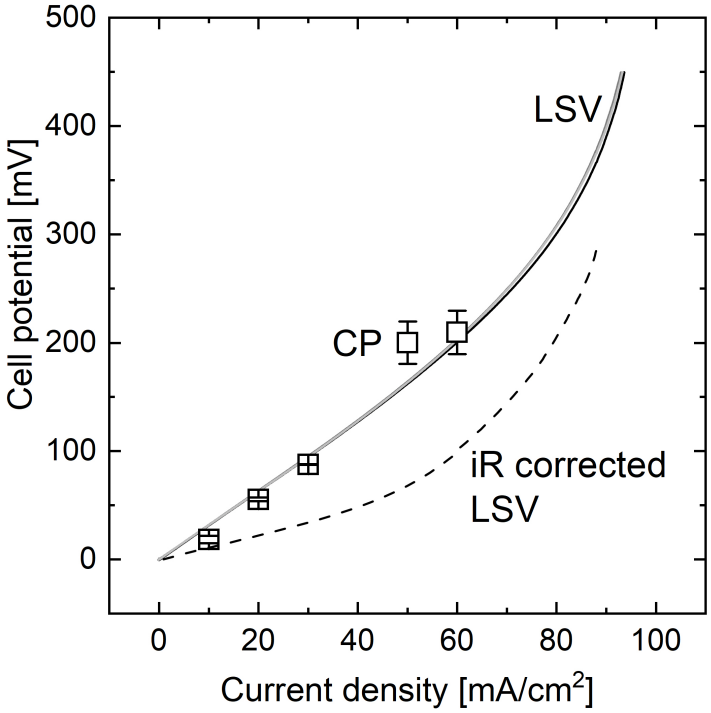

Figure 5.8: Steady-state current-voltage behavior of tubular EHC recorded by current steps (40 min, squares) and polarization behavior recorded by linear sweep voltammetry (solid lines) and iR corrected linear sweep (dashed line), 50 ml/min H_2, 100% relative humidity in the feed gas.

Figure 5.10 (a) presents the Nyquist plot of electrochemical impedance spectra recorded between multi-chronopotentiometry experiments. The current and voltage response of the consecutive runs between the impedance spectra is presented in Figure 5.9. The high-frequency resistance of the cell ranged between 2 to 2.75 Ωcm^2 in electrochemical impedance measurements (Fig. 5.10 (a)). In comparison, studies on planar EHCs have reported limiting current densities ranging from 0.5 to 3.5 A cm^{-2} at room temperature, which is significantly higher than achieved in this work [Zou2021; Strö2002]. For instance, Zou et al. achieved 3.5 A cm^{-2} with similar catalyst loading as in this study but with a significantly thinner ion exchange membrane of 15 µm compared to 300 µm in this work. The iR-corrected linear sweep demonstrates cell potentials comparable to those in the literature and emphasizes major ohmic loss contributions to overall cell performance. For example, at a current density of 50 mA cm^{-2}, the potential declines from 150 mV to 50 mV after iR correction. However, it should

be noted that this work introduces the first tubular EHC, and the potential for optimization is thus not yet tapped.

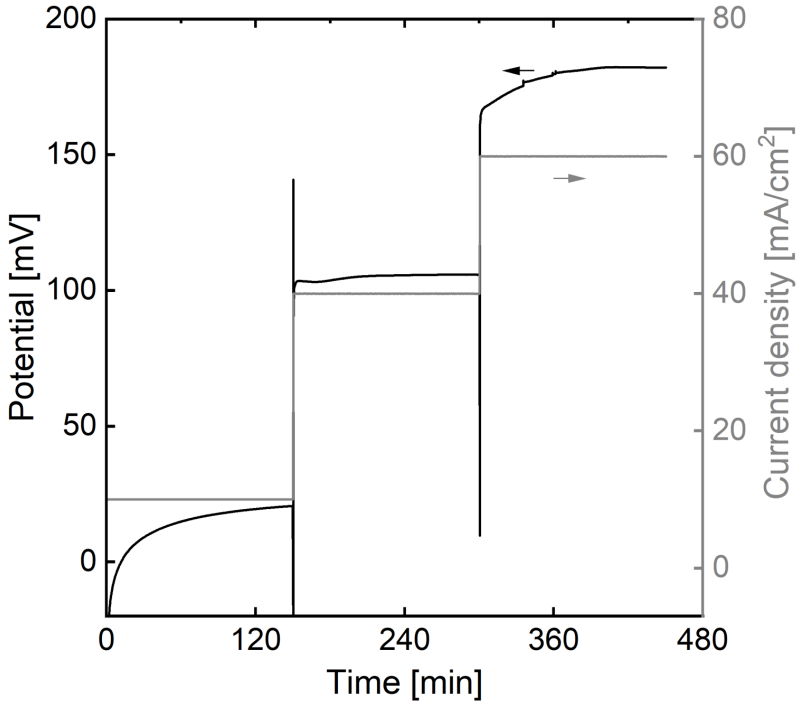

Figure 5.9: Cell potential and current over time during a multichronopotentiometric measurement.

Possible reasons for the limited electrochemical performance of the tubular EHC, especially at current densities above 60 mA cm^{-2}, might be drying out of the proton exchange membrane, condensation of water in the porous support or on the electrodes, and corrosion of the stainless steel anode support. At higher current densities, more water is needed to maintain a sufficient wetting degree of the proton exchange membrane. Thus, non-ideal humidification of the proton exchange membrane, due to mass-transport limitations in the porous transport layer of the anode, could lead to an increase of the cell potential at higher current densities [Piva2024; Pine2022a].

This hypothesis can be underlined by the impedance data (Fig. 5.10 (a)). After preconditioning, the ohmic resistance of the cell is 2.75 Ωcm^2. After 2.5 h chronopotentiometry at 10 mA cm^{-2}, the ohmic resistance drops to 2.18 Ωcm^2 (Fig. 5.10 (a), plot 2), but the Nyquist plot qualitatively re-

mains similar to the initial spectrum. After 2.5 h chronopotentiometry at 40 mA cm^{-2} (Fig. 5.10 (a), plot 3), the first semicircle in the Nyquist plot is significantly smaller. The spectrum's shape changes over the whole frequency range indicating rehumidification of the membrane [Méri2006]. After operation at 60 mA cm^{-2}, the magnitude of the impedance increases (Fig. 5.10 (d), plot 4), and the spectrum is shifted to higher resistances indicating again the dehumidifaction of the membrane, also correlating with the increase of potential observed in the linear sweep at current densities above 60 mA cm^{-2} (Fig. 5.8). After running the cell at 80 mA cm^{-2} (Fig. 5.10 (d), plot 5) for 4 min, the spectrum shifts to the initial high-frequency intercept and additionally changes qualitatively, indicating a fundamental change in the electrochemical system such as dehydration of the membrane.

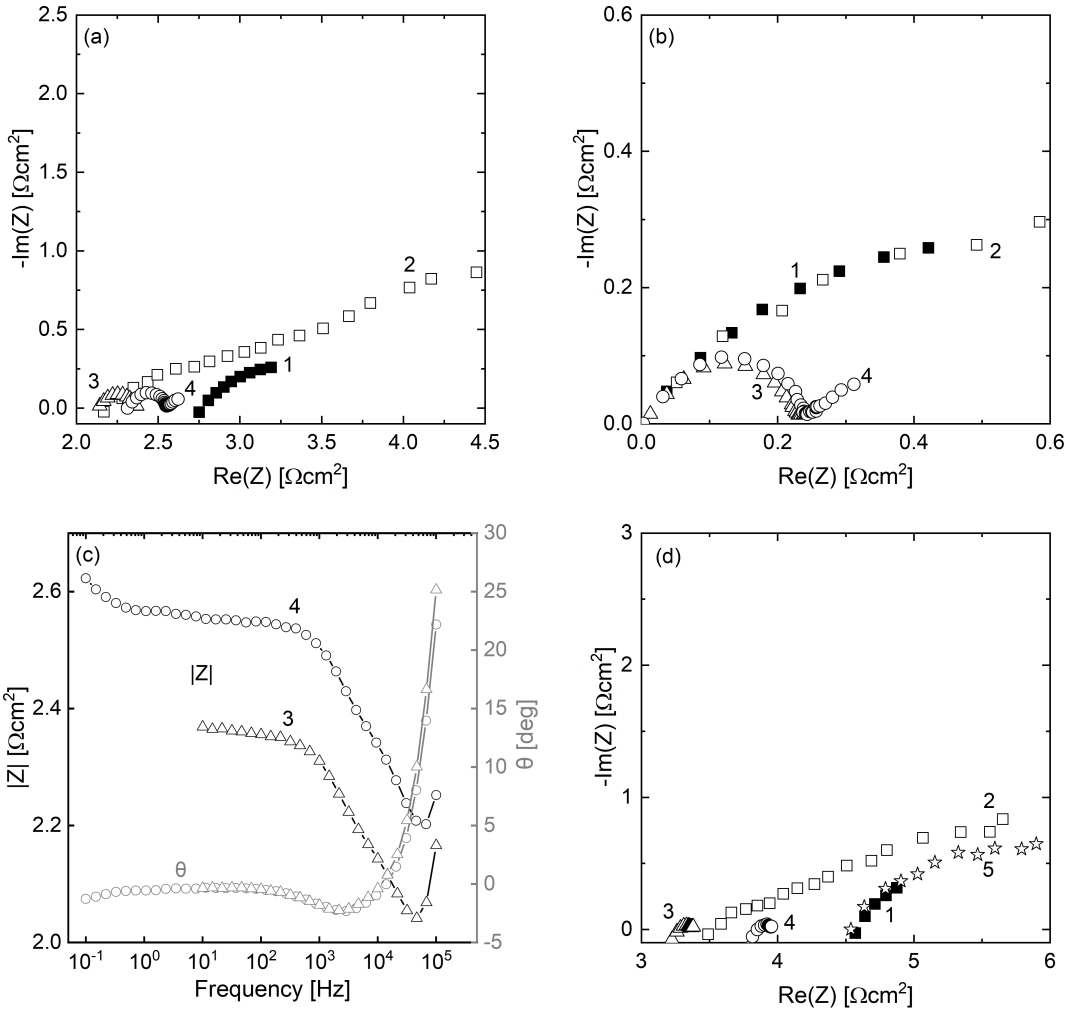

Figure 5.10: (a) Nyquist plot of impedance spectra consecutively recorded between multi-chronopotentiometry experiments, 1: after preconditioning of the cell, 2: after 2.5 h at 10 mA cm^{-2}, 3: after 2.5 h at 40 mA cm^{-2}, 4: after 2.5 h at 60 mA cm^{-2}; (b) zoom in on high frequencies of (a) all spectra shifted to zero ohmic resistance; (c) Bode diagram of measurement 3 and 4, (d) Nyquist plot of impedance spectra consecutively recorded between multichronopotentiometry experiments, 1: after preconditioning of the cell, 2: after 2.5 h at 20 mA cm^{-2}, 3: after 2.5 h at 40 mA cm^{-2}, 4: after 2.5 h at 60 mA cm^{-2}, 5: after 4 min at 80 mA cm^{-2}.

Additionally, water might condense in the hydrophilic porous anode and on the catalyst surface, leading to flooding and resulting in diffusion-limited hydrogen and water vapor transport toward the cathode [Nguy2011]. In electrochemical impedance analysis, the effect of flooding can be observed in the low-frequency regime. As membrane drying seems to occur simultaneously, changing the impedance spectrum over the whole frequency range, it is difficult to separate the two effects (Fig. 5.10 (a, b)) [Méri2006].

Consequently, optimizing the water transport to the EHC membrane is crucial to improve the performance of the herein presented prototype. Moreover, corrosion might occur on the stainless steel anode support structure, leading to increased contact resistance between the anode gas diffusion and anode catalyst layers and, consequently, higher cell potentials [Miya2013]. The leaching of iron ions from the stainless steel anode could additionally lead to contamination and severe degradation of the proton exchange membrane, leading to decreased cell performance [Li2020; Chen2007].

5.4.3 Hydrogen compression in tubular reactor

The hydrogen compression capability of the tubular EHC was examined at a cathode pressure of 2 bar at a constant current density of 60 $mAcm^{-2}$ for three and at a constant current density of 50 $mAcm^{-2}$ for six hours. It should be noted that the three-hour and six-hour experiments were not conducted consecutively. Figure 5.11 (a) shows the pressure build-up on the cathode side of the EHC in the initial electrolysis phase. The targeted 2 bar cathode pressure was achieved after 60 min electrolysis. The set pressure was maintained for 100 min at a mean cell potential of 180 mV. In a six-hour experiment, presented in 5.11 (b), the pressure on the cathode side was set to 1.8 bar at the beginning of the experiment. The cell potential decreases from 230 mV to 190 mV during the first 150 min of the experiment. As the cell potential is elevated compared to the 60 min experiment, we hypothesize that the system's preconditioning was insufficient. Thus, in the first 150 min of the experiment, the membrane is hydrated further, and the resistance decreases [Pine2022a].

This hypothesis is also underlined by the impedance spectra measured before and after the experiment - the high frequency ohmic cell resistance decreases from 3.75 Ωcm^2 to 2.75 Ωcm^2 over the course of the experiment. The cell potential of both pressurized experiments is not significantly different from the non-pressurized experiments, as to be expected from eq. 2.3.

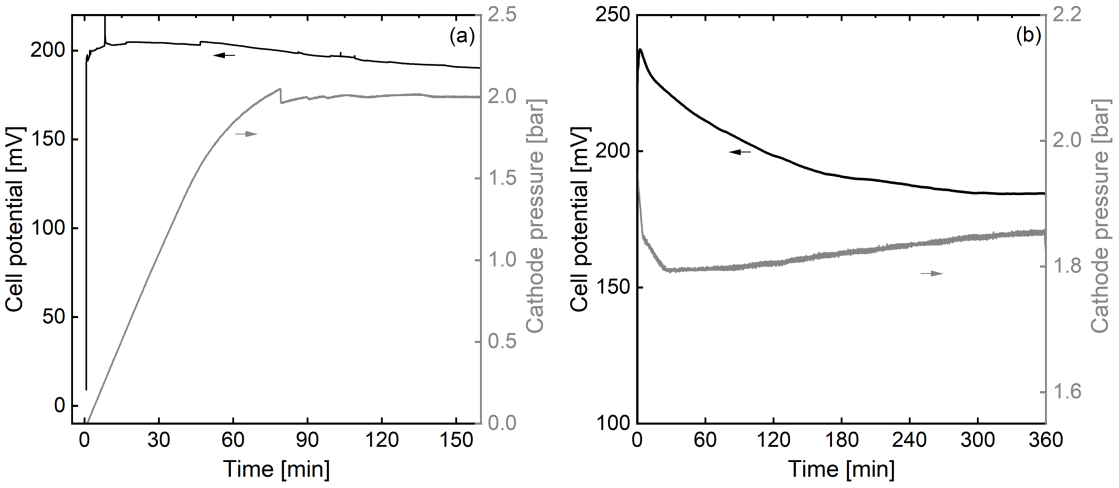

Figure 5.11: Cathode pressure (grey) and cell potential (black) of tubular EHC over electrolysis time, 50 mL min^{-1} H_2 feed flow rate equals lambda of 10, 100% relative humidity of the feed gas, (a) 60 mA cm^{-2} constant current, (b) 50 mA cm^{-2} constant current, the three-hours and six-hours experiments were not conducted consecutively.

5

5.4.4 Modeling of a tubular EHC

A numerical model was developed to investigate mass transport and evaluate the compression and separation performance of tubular EHCs. The planar EHC model is validated by comparing the modeled polarization curves with experimental research data from Onda et al. [Onda2007] and Ibeh et al. [Ibeh2007]. The validation is also assumed to be valid for the tubular EHC model as only the geometrical parameters change, and the general model equations are the same as for the planar cell. The following tables 5.1 and 5.2 summarize the modeling parameters for the validation.

Table 5.1: Inputs used in the validation with experimental data from Ibeh et al. [Ibeh2007].

Input	Value
T	318 K
p_a	1.013 bar
p_c	1.013 bar
L_{membr}	140 μm
δ_a	176 μm
A	25 cm^2
RH^{in}	100 %
RH^{out}	100 %
x^{bulk}_{c,H_2}	0.9
$\dot{N}^{in}_{Tot}$	$1.891 * 10^{-4}$ $\frac{mol}{s}$
R^{add}	6.1 $m\Omega$

Table 5.2: Inputs used in the validation with experimental data from Onda et al. [Onda2007].

Input	Value
T	333.15 K
p_a	1.013 bar
p_c	4, 8, 10 bar
L_{membr}	112 μm
δ_a, δ_c	200 μm
A	10 cm^2
RH^{in}	100 %
RH^{out}	97 %
$\dot{N}^{in}_{Tot}$	$3.22 * 10^{-5}$ $\frac{mol}{s}$

Table 5.3: Hydrogen bulk mole fractions used for the model validation with experimental data from Onda et al. [Onda2007].

Cathode Pressure	x_{a,H_2}^{inlet}	x_{c,H_2}^{bulk}
4 bar	0.8037	0.9517
8 bar	0.8037	0.9758
10 bar	0.8037	0.9807

The cell potential reported by Ibeh et al. [Ibeh2007] increases logarithmic at low current densities, transitioning to a linear rise towards infinity at the limiting current density, as illustrated in Figure 5.12. Overall, the numerical method agrees well with the experimental data from Onda et al. The predicted limiting current density demonstrates an accuracy of 2.3 % for a hydrogen inlet mole fraction of 0.25 and 1.2 % for 0.08. However, the cell voltage is underestimated near the limiting current density, likely due to the assumption of constant hydrogen and water content in the bulk phase.

In Figure 5.12, the polarization curve computed using the model is compared with experimental data from Onda et al. [Onda2007]. The numerically determined cell potential trend aligns well with the experimental findings, with ohmic overpotential—exhibiting a linear trend—dominating the cell voltage. Onda et al. determined that the activation overpotential is one order of magnitude smaller than ohmic potential, making its neglect in the model reasonable. Overall, the numerically determined cell potential is exceeding the experimental values over the whole current density regime, which indicates an overestimation of the ohmic resistances of the cell.

Overall, less than 10 % deviation in the ohmic region and under 2.3 % deviation for limiting current density predictions were achieved in the model validation. It was confirmed that activation overpotential and mass transport limitations at the cathode are negligible for EHC modeling.

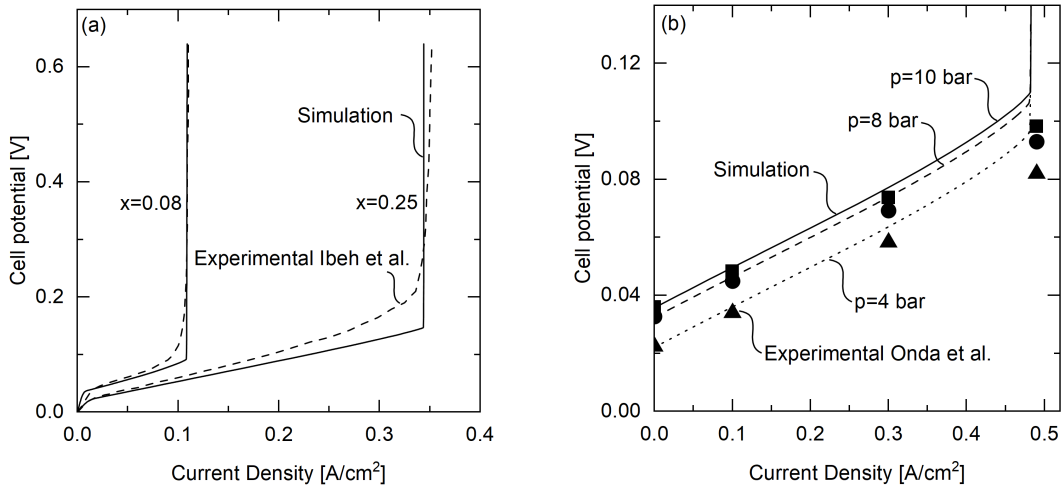

Figure 5.12: (a) Comparison of simulation (dashed line) and experimental results of Ibeh et al. [Ibeh2007] (solid line) of the polarization behavior with different feed compositions; (b) Comparison of simulation (line) and experimental results (points) of Onda et al. [Onda2007] of the polarization behavior with different cathode pressures.

Table 5.4: Inputs used in the model examination.

Inputs	Value
p_a	60 *bar*
p_c	700 *bar*
T	323.15 *K*
I	1 *A*
L	280 μm
x_{a,H_2}^{inlet}	0.1
x_{c,H_2}^{bulk}	0.9997
RH^{in}	100 %
RH^{out}	100 %
$\dot{N}_{Tot}^{in}$	$1.03643 * 10^{-4}$ $\frac{mol}{s}$
ϵ_a	0.4
ϵ_c	0.6

Polarization behavior

The model input parameters used in the model examination if not explicitly mentioned otherwise, are presented in Table 5.4. In the modeled polariza-

tion curve of the tubular cell in Figure 5.13 shows the predominant contribution of the Nernst voltage resulting from the high partial pressure gradient across the cell. The ohmic overpotential exhibits a typical linear relationship with current. As the current increases, the impact of mass transport limitations becomes more pronounced. At a current density of 2.25 A cm^{-2}, which represents the maximum achievable value, based on the hydrogen feed flow and Faradays law, the limiting current is reached. At this current, no hydrogen is available for oxidation at the catalyst layer of the anode outlet, as the diffusion rate is insufficient to support higher oxidation rates at elevated currents. This results in an increase in both mass transport overpotential and total electrode voltage towards infinity. The abrupt rise in mass transport overpotential observed in the simulation arises from averaging across all sub-elements, with the steep exponential increase in electrode voltage of the final sub-element becoming evident just before reaching the limiting current.

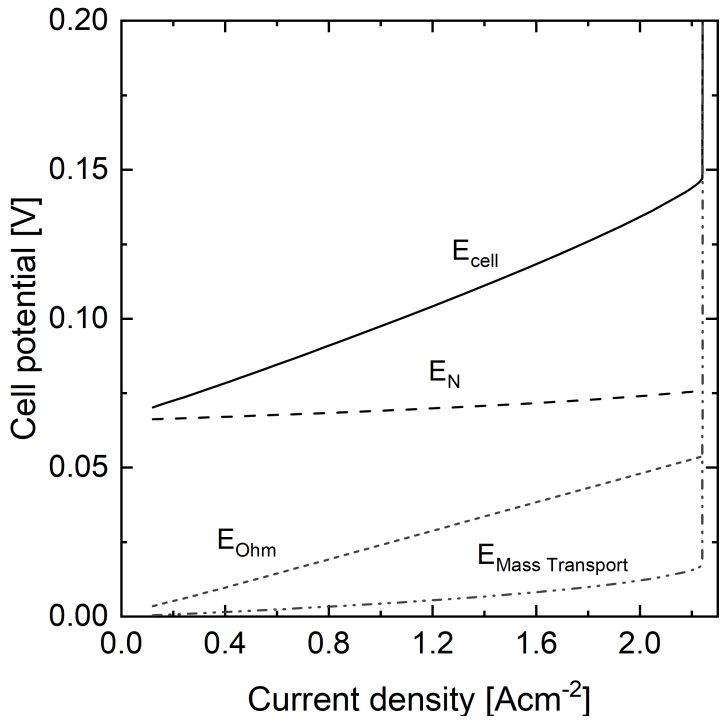

Figure 5.13: Polarization curve of the tubular EHC. The inputs used in the computation can be found in Table 5.4.

Anode porosity

Mass transport plays a crucial role in the performance of the EHC. As illustrated in Figure 5.13, mass transport limitations at the anode result in a significant rise in electrode voltage at elevated currents. Consequently, understanding and optimizing mass transport becomes increasingly important. The optimization objective should focus on maximizing the limiting current to enhance the hydrogen recovery factor (HRF). Therefore, a more detailed analysis of hydrogen mole fractions at the anode was conducted.

The influence of anode porosity on limiting current density and hydrogen mole fraction is investigated in Figure 5.14 (a) and (b). The anode hydrogen mole fraction decreases from the bulk to the catalyst layer. Hydrogen is oxidized at the catalyst layer, resulting in a mole fraction gradient towards the membrane. A higher porosity leads to a higher diffusion coefficient (see Bruggeman correlation in 5.8), i.e. to smaller mass transport resistances. Thus, the mole fraction gradient at the anode towards the membrane decreases with increasing porosity, as shown in Figure 5.14 (b). A hydrogen mole fraction of zero at the anode catalyst layer of the last sub element is observed at a higher current when using a more porous anode. Consequently, the limiting current density, shown in Figure 5.14 (a), increases with increasing anode porosity.

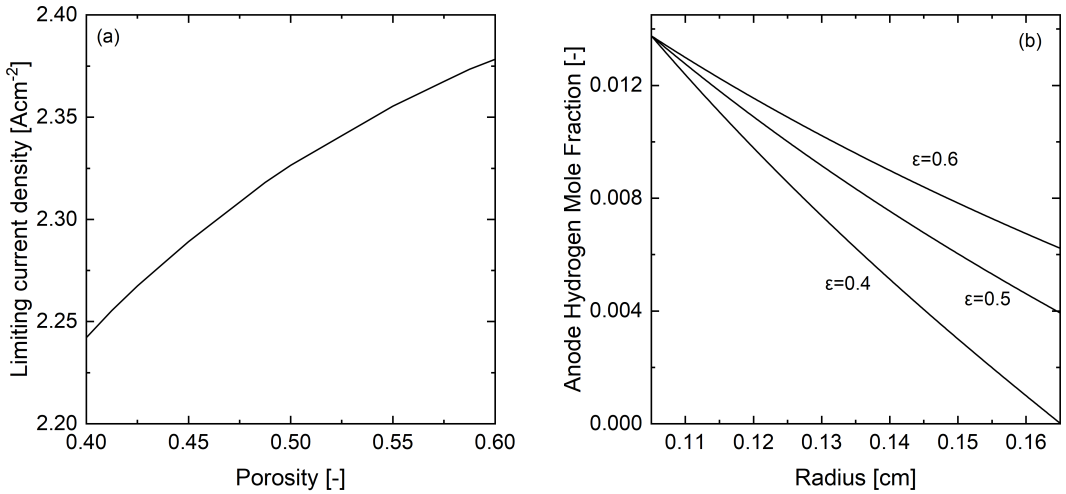

Figure 5.14: (a) Limiting current for the last sub element (number 50), and thus for the entire cell as a function of the anode porosity. The inputs used in the computation can be found in 5.4. (b) Anode hydrogen mole fraction for last sub element (number 50) for three different anode porosities at 2.2 A cm^{-2}.

Aiming for maximum process efficiency, both HRF and power efficiency should be maximal. The power efficiency, shown in Figure 5.15, increases at low current densities until reaching a maximum, which shifts to higher current densities for thinner membranes, and then, decreases again. The trend of power efficiency relative to current in Figure 5.15 can be explained as follows: back diffusion, decreasing logarithmically with increasing membrane thickness, dominates efficiency at low currents, making thicker membranes preferable in this range. Conversely, at high currents, the cell potential dominates the efficiency, favoring thinner membranes; this advantage grows with increasing current due to increasing ohmic potential. Overall, thicker membranes are more efficient at low currents and thin membranes exhibit high efficiency at high currents. These observation are consistent with the findings of Kim et al. [Kim2022] on specific power consumption, which is inversely proportional to the power efficiency.

The HRF, increases linearly with increasing current density and constant feed flow, due to the linear relation of the hydrogen product flow and current by Faradays law. Back diffusion shows minimal dependence on current since the boundary conditions, including cathode pressure and purity, are maintained constant. Consequently, the net hydrogen flow to the cathode

is nearly linear with respect to current, which also applies to the HRF.

The operating point with maximum HRF and power efficiency in our computations was obtained for a membrane thickness of 100 µm at a current of 2.5 A achieving a HRF of 87.5 % at an efficiency of 56.8 %. In comparison, the HRF using pressure swing adsorption is in the range of 35 % for comparable inputs, and the isentropic efficiency of a reciprocal hydrogen compressor is in the range of 56 %, indicating technological competitiveness of EHC for hydrogen compression and separation [Nord2019; Liem2017; Gard2009].

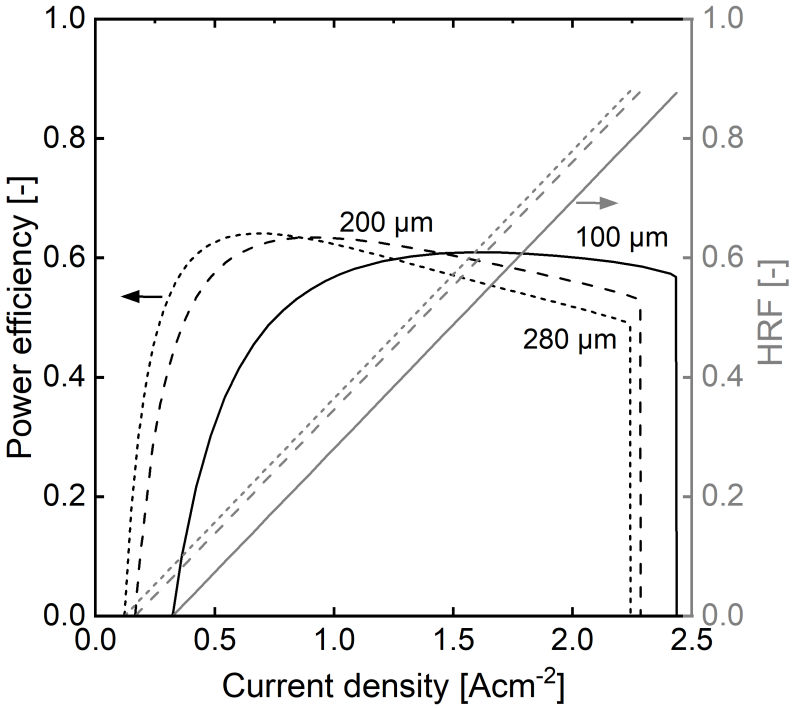

Figure 5.15: Power efficiency and hydrogen recovery factor for varying current densities with 100 µm (solid lines), 200 µm (big dashed line) and 280 µm (small dashed line) , all other input parameters according to Table 5.4.

Model Shortcomings and Outlook

To further refine the model, it is recommended to eliminate the fixed cathode hydrogen purity as a boundary condition. The model simplifies the boundary layers by assuming constant molar concentrations, neglecting concentration gradients developing by component transport towards the electrodes.

However, those concentration gradients significantly influence mass transport resistance and humidification of the membrane. A more detailed treatment of these gradients should be implemented to provide a realistic assessment of mass transport limitations. Additionally, flow conditions in the bulk phase, which is a key difference between planar and tubular cells are not included in the model due to the constant bulk assumption. At 700 bar, H_2 significantly deviates from ideal gas behavior, consequently dropping the assumption of ideal gas behavior and incorporating real gas equations of state would improve prediction accuracy under these conditions. The catalyst layer mass transport resistance constitutes a substantial portion of total resistance [Spin2017]. Future work should focus on modeling transport processes within the catalyst layer to understand how various catalyst layer morphology affect the EHC performance.

5.5 Conclusion

This chapter introduces the first tubular electrochemical hydrogen compressor (EHC) featuring a 3D-printed, stainless-steel porous tubular anode. This work introduces an innovative concept to fabricate tubular membrane electrode assemblies for high differential pressure applications comprising a rigid, 3D-printed anode and a catalyst-coated tubular membrane. Electrochemical testing revealed the tubular MEA's efficacy for gas-phase electrochemistry at current densities up to 60 $mAcm^{-2}$ in continuous mode, reaching a differential pressure of 2 bar across the anode and cathode compartments. Additionally, electrochemical impedance spectroscopy analysis before and after EHC experiments demonstrate the change in electrochemical properties of the EHC, which could be attributed to the membrane drying, flooding caused by water condensation in the porous network of the anode, and contamination due to the undesired leaching of iron ions from the stainless-steel anode. This work spotlights the proof-of-concept for the first tubular EHC, expanding the horizons in the field of EHC, transitioning from planar to tubular modules that promise greater surface-to-volume ratios, superior packing densities, and facile high differential pressure operation. The presented module has potential for improvement by considering thinner tubular membranes, inert electrode materials, e.g., titanium, and depositing noble metals for enhanced stability and electrical conductivity, which is under investigation in our group. Additionally, a basic 2D model was developed to investigate mass transport in the tubular cell. The efficiency and hydrogen recovery of tubular EHC with varying operation conditions and membrane thickness was evaluated. At optimal operating conditions, a hydrogen recovery of 87 % at a power efficiency of 56 % was computed for compression of hydrogen from 60 to 700 bar and purification from 10 vol % to 99.97 vol %. However, due to simplifying assumptions, the model could not capture the cell's behavior observed in the experimental part.

6

Conclusion and Perspectives

Hydrogen compression will play a crucial role in a decarbonized energy system by facilitating the efficient storage, transportation, and utilization of hydrogen as a carbon-free energy carrier. Electrochemical hydrogen compressors (EHCs) are a promising alternative to conventional mechanical compressors due to their high theoretical compression efficiency, reduced maintenance needs, and lower capital costs. Additionally, EHCs combine compression and separation of hydrogen, enabling both withdrawal from natural gas/hydrogen mixtures for on-site use and separating hydrogen from gas mixtures to yield value-added products. This thesis focuses on the development and assessment of electrochemical hydrogen compression technologies, emphasizing their role in facilitating efficient combined hydrogen purification and compression. The answers to the research questions raised in the introduction are summarized in the following:

Sub-question 1: How do low- and high-temperature EHCs compare regarding hydrogen compression and separation performance?

The first sub-question was addressed by comparing the performance of perfluor sulfonic acid (PFSA, low-temperature) and polybenzimidazole (PBI, high-temperature) based EHCs in terms of operational parameters, polarization behavior, and compression efficiency. While both EHCs achieved hydrogen compression to 6 bar, the high-temperature EHC demonstrated

a higher compression efficiency of 40 % compared to 30 % for the low-temperature EHC, attributed to its lower cell potential. Additionally, the influence of feed gas humidity on the high-temperature EHC was investigated. The findings highlighted that although the high-temperature EHCs can operate in anhydrous conditions, introducing very low relative humidity ($<$1 %) lowers the cell potential up to 30 %. Combining the unit operations compression and separation in one technology holds great potential for reducing process complexity, footprint, and, consequently, cost. Combined compression and separation were studied in both EHC-types while measuring the product gas purity. The high-temperature EHC achieved lower methane concentrations during separation from methane/hydrogen mixtures meeting fuel cell grade requirements.

Sub-question 2: What is the influence of trace impurities present in the natural gas grid on EHCs and how to mitigate them?

The influence of trace impurities present in the natural gas grid on EHCs was studied experimentally by introducing single natural gas impurities to the feed gas. Low- and high-temperature EHCs were compared regarding their poisoning tolerance against the natural gas impurities 4 vol.% CO_2, 30 ppm CO, 14 ppm NH_3 and 3.5 ppm H_2S. Detrimental increase in cell potential of up to 270 % was observed upon introduction of CO_2, CO and H_2S in the hydrogen-feed of the low-temperature EHC. Stable operation of the high-temperature EHC was achieved in the presence of CO_2, CO, and H_2S, with an increase in cell potential remaining below 5 %. The effect of dilution with methane - as a model for natural gas - on the poisoning of the EHc was investigated for the high-temperature EHC to get closer to the real operation conditions in natural gas. Diluting the CO_2, CO, and NH_3/hydrogen mixtures with methane yielded negligible changes in the high-temperature EHC. However, diluting the H_2S/hydrogen feed led to a stark potential increase and potential oscillations, which were attributed to the adsorption mechanism of H_2S on the Pt-catalyst. Focusing on H_2S poisoning in high-

temperature EHC, poison mitigation strategies were evaluated regarding effectiveness and process efficiency. Temperature cycling, air bleeds, and electro-oxidation by cyclic voltammetry were investigated as strategies to mitigate the poisons' effect. Performing repetitive electro-oxidation showed the most potential among the investigated strategies. However, future research should focus on the long-term effects of the mitigation strategies. Finally, the effect of natural gas on the high-temperature EHC was investigated. The higher hydrocarbons in the natural gas had a minor effect on the EHC operation. Separation of hydrogen from 20 vol. % hydrogen in natural gas was demonstrated, achieving a product gas purity of 99.999%. Furthermore, simultaneous compression and separation from natural gas/hydrogen mixtures was performed for the high-temperature EHC, which had not yet been demonstrated.

In summary, the high-temperature EHC with a H_3PO_4-doped polybenzimidazole membrane showed superior compression efficiency, product gas purity, and robustness. Challenges remaining for a successful combination of compression and separation of hydrogen from natural gas are mechanical and chemical stability of PBI-membranes. Additionally, a mechanistic understanding of sulfur catalyst poisoning and membrane alteration by NH_3 is lacking, as well as long-term operation data with those poisons enabling lifetime predictions.

Sub-question 3: Can a tubular EHC be built and operated?

An innovative tubular design for EHCs based on 3D-printed porous anodes was developed. After establishing a production method for the tubular membrane electrode assembly, an experimental proof-of-concept of the tubular gas phase electrochemical cell achieving compression up to 3 bar was conducted. A 2D model for the analysis of the tubular EHC was developed. By establishing a proof-of-concept of the tubular reactor design for EHC, a starting point for future transitioning from planar to tubular modules that promise higher packing densities and facile high differential pressure opera-

tion was established. Additionally, this work opens up new research opportunities in electrochemical process engineering by translation of the concept to other applications, for example, electrochemical CO_2 reduction. Future work should focus on reaching state-of-the-art current densities as well as lower cell potentials, for example, by improved material systems of the tubular anode and contacting concepts. The developed 2D model enabled the evaluation of anode morphology and indicated the technological competitiveness of the EHC against state-of-the-art technologies. The current 2D model provides insights into the operational characteristics of the tubular design; however, its simplifying assumptions limit its ability to fully capture the interactions occurring within the electrochemical cell. To enable technological comparison of tubular and planar EHCs, and thus predict technological feasibility, a more detailed model, especially considering mass transport phenomena, should be established.

Overall, this work advances the industrial applicability of EHCs by elucidating key challenges related to impurity tolerance and developing mitigation strategies and novel reactor concepts. This research paves the way for more effective integration of hydrogen into existing energy infrastructures, ultimately supporting the transition to a sustainable hydrogen economy in both industrial applications and broader energy systems.

Bibliography

[Aasa2021] M. Aasadnia, M. Mehrpooya, and B. Ghorbani. “A novel integrated structure for hydrogen purification using the cryogenic method”. *Journal of Cleaner Production*, vol. 278. 2021. DOI: 10.1016/j.jclepro.2020.123872 (cit. on p. 10).

[Abe2019] J. O. Abe, A. P. Popoola, E. Ajenifuja, and O. M. Popoola. “Hydrogen energy, economy and storage: Review and recommendation”. *International Journal of Hydrogen Energy*, vol. 44, no. 29. 2019. DOI: 10.1016/j.ijhydene.2019.04.068 (cit. on pp. 9, 91).

[Agmo1995] N. Agmon. “The Grotthuss mechanism”. *Chemical Physics Letters*, vol. 244, no. 5-6. 1995. DOI: 10.1016/0009-2614(95)00905-J (cit. on pp. 22, 23).

[Amin2023] M. Amin, A. S. Butt, J. Ahmad, C. Lee, S. U. Azam, H. A. Mannan, A. B. Naveed, Z. U. R. Farooqi, E. Chung, and A. Iqbal. “Issues and challenges in hydrogen separation technologies”. *Energy Reports*, vol. 9. 2023. DOI: 10.1016/j.egyr.2022.12.014 (cit. on p. 10).

[Ange2025] R. Angelico, F. Giametta, B. Bianchi, and P. Catalano. “Green Hydrogen for Energy Transition: A Critical Perspective”. *Energies*, vol. 18, no. 2. 2025. DOI: 10.3390/en18020404 (cit. on p. 1).

[Arun2024] K. Arunagiri, J. M. Turssline, and C. G. Arges. “Purifying Hydrogen from Dilute Hydrogen - Natural Gas Mixtures Using HT-PEM Electrochemical Hydrogen Pumps”. *ACS Energy Letters*, vol. 9, no. 6. 2024. DOI: 10.1021/acsenergylett.4c00746 (cit. on pp. 61, 62).

[Ayku2022] Y. Aykut and A. Bayrakçeken Yurtcan. “Catalyst development for viability of electrochemical hydrogen purifier and compressor (EHPC) technology”. *International Journal of Hydrogen Energy*, vol. 47, no. 45. 2022. DOI: 10.1016/j.ijhydene.2021.12.148 (cit. on pp. 22, 28).

[Ayku2023] Y. Aykut and A. B. Yurtcan. “The role of the EHC system in the transition to a sustainable energy future: A review”. *International Journal of Hydrogen Energy*, vol. 48, no. 60. 2023. DOI: 10.1016/j.ijhydene.2023.03.109 (cit. on pp. 9, 10, 91).

[Ayku2024] Y. Aykut, R. G. Akay, and A. Bayrakçeken Yurtcan. “Compression performance of an electrochemical hydrogen compressor at low and high temperatures”. *International Journal of Hydrogen Energy*, vol. 75. 2024. DOI: 10.1016/j.ijhydene.2024.01.192 (cit. on p. 33).

[Bago2005] S. Bagotsky. *Fundamentals of electrochemistry*. (The Electrochemical Society series). 2nd ed. Hoboken, New Jersey: John Wiley & Sons, Inc., Publication, 2005. ISBN: 978-1-85573-919-2.DOI: 10.1533/9781845690878.1.1 (cit. on p. 26).

[Bal2023] İ. B. Bal, G. N. Bulanık Durmuş, and Y. Devrim. “Fabrication and performance evaluation of graphene-supported PtRu electrocatalyst for high-temperature electrochemical hydrogen purification”. *International Journal of Hydrogen Energy*, vol. 48, no. 63. 2023. DOI: 10.1016/j.ijhydene.2023.03.256 (cit. on pp. 22, 28).

[Bard2001] A. J. Bard and L. R. Faulkner. *Electrochemical methods: fundamentals and applications*. 2nd ed. New York Weinheim: John Wiley & Sons, Inc., 2001. ISBN: 978-0-471-04372-0. (Cit. on pp. 27, 28, 104, 107).

[Bori2023] G. Borisov, N. Borisov, J. Heiss, U. Schnakenberg, and E. Slavcheva. “PEM Electrochemical Hydrogen Compression with Sputtered Pt Catalysts”. *Membranes*, vol. 13, no. 6. 2023. DOI: 10.3390/membranes13060594 (cit. on p. 43).

[Bouc1999] R. Bouchet and E. Siebert. “Proton conduction in acid doped polybenzimidazole”. *Solid State Ionics*, vol. 118, no. 3. 1999. DOI: 10.1016/S0167-2738(98)00466-4 (cit. on p. 24).

[Bouw2014] P. Bouwman. “Electrochemical Hydrogen Compression (EHC) solutions for hydrogen infrastructure”. *Fuel Cells Bulletin*, vol. 2014, no. 5. 2014. DOI: 10.1016/S1464-2859(14)70149-X (cit. on pp. 19, 20).

[Brai2023] M. Braig and R. Zeis. “Distribution of relaxation times analysis of electrochemical hydrogen pump impedance spectra”. *Journal of Power Sources*, vol. 576, no. 233203. 2023. DOI: 10.1016/j.jpowsour.2023.233203 (cit. on p. 28).

[Capo2022] R. Caponetto, E. Privitera, G. Mirone, and F. Matera. “Structural Analysis of Electrochemical Hydrogen Compressor End-Plates for High-Pressure Applications”. *Energies*, vol. 15, no. 16. 2022. DOI: 10.3390/en15165823 (cit. on p. 92).

[Casa2008] C. Casati, P. Longhi, L. Zanderighi, and F. Bianchi. “Some fundamental aspects in electrochemical hydrogen purification/compression”. *Journal of Power Sources*, vol. 180, no. 1. 2008. DOI: 10.1016/j.jpowsour.2008.01.096 (cit. on p. 92).

[Chen2007] X. Cheng, Z. Shi, N. Glass, L. Zhang, J. Zhang, D. Song, Z. S. Liu, H. Wang, and J. Shen. “A review of PEM hydrogen fuel cell contamination: Impacts, mechanisms, and mitigation”. *Journal of Power Sources*, vol. 165, no. 2. 2007. DOI: 10.1016/j.jpowsour.2006.12.012 (cit. on p. 117).

[Chen2022] Y. Chen, K. Azizi, W. Zhang, D. Aili, S. Primdahl, L. N. Cleemann, H. A. Hjuler, and Q. Li. “Feasibility of using thin polybenzimidazole electrolytes in high-temperature proton exchange membrane fuel cells”. *International Journal of Hydrogen Energy*, vol. 47, no. 66. 2022. DOI: 10.1016/j.ijhydene.2022.06.156 (cit. on p. 48).

[Chhe2024] M. Chhetri, D. P. Leonard, S. Maurya, P. Sharan, Y. Kim, A. Kozhushner, L. Elbaz, N. Ghorbani, M. Rafiee, C. Kreller, and Y. S. Kim. “Electrochemical pumps based on ion-pair membranes for separation of hydrogen from low-concentration mixtures”. *Nature Energy*, vol. 9. 2024. DOI: 10.1038/s41560-024-01669-6 (cit. on pp. 11, 19, 20, 22).

[Chou2020] A. Chouhan, B. Bahar, and A. K. Prasad. “Effect of back-diffusion on the performance of an electrochemical hydrogen compressor”. *International Journal of Hydrogen Energy*, vol. 45, no. 19. 2020. DOI: 10.1016/j.ijhydene.2020.02.048 (cit. on pp. 16, 91, 110, 111).

[Cost2001] P. Costamagna. “Transport phenomena in polymeric membrane fuel cells”. *Chemical Engineering Science*, 16th International Conference on Chemical Reactor Engineering, vol. 56, no. 2. 2001. DOI: 10.1016/S0009-2509(00)00232-3 (cit. on p. 106).

[Cour2003] J. F. Coursange, A. Hourri, and J. Hamelin. “Performance Comparison Between Planar and Tubular-Shaped PEM Fuel Cells by Three-Dimensional Numerical Simulation”. *Fuel Cells*, vol. 3, no. 1-2. 2003. DOI: 10.1002/fuce.200331101 (cit. on p. 92).

[Demi2018] M. E. Demir and I. Dincer. “Cost assessment and evaluation of various hydrogen delivery scenarios”. *International Journal of Hydrogen Energy*, vol. 43, no. 22. 2018. DOI: 10.1016/j.ijhydene.2017.08.002 (cit. on p. 2).

[Dong2021] X. Dong, G. Li, W. Chen, C. Zhu, T. Li, Y. Song, N. Sun, and W. Wei. “Gas-phase CO_2 electroreduction over Sn-Cu hollow fibers”. *Materials Advances*, vol. 2, no. 1. 2021. DOI: 10.1039/d0ma00851f (cit. on p. 92).

[Dong2022] W. Dong, C. Xu, W. Zhao, M. Xin, Y. Xiang, A. Zheng, M. Dou, S. Ke, J. Dong, L. Qiu, and G. Xu. “Poisoning Effects of H_2S,CS_2, and COS on Hydrogen Oxidation Reaction over Pt/C Catalysts”. *ACS Applied Energy Materials*, vol. 5, no. 10. 2022. DOI: 10.1021/acsaem.2c02284 (cit. on p. 59).

[Durm2021] G. N. B. Durmus, C. O. Colpan, and Y. Devrim. “A review on the development of the electrochemical hydrogen compressors”. *Journal of Power Sources*, vol. 494, no. 229743. 2021. DOI: 10.1016/j.jpowsour.2021.229743 (cit. on pp. 2, 20, 58, 91).

[Durm2022] G. N. B. Durmus, C. O. Colpan, and Y. Devrim. “Investigation of the performance of high-temperature electrochemical hydrogen purification from reformate gases”. *International Journal of Energy Research*, vol. 46, no. 8. 2022. DOI: 10.1002/er.7940 (cit. on pp. 62, 66).

[DVGW2021] DVGW German Technical and Scientific Association for Gas and Water, *DVGW G 260 (A) - Gasbeschaffenheit*, 2021 (cit. on p. 58).

[Eike2001] M. Eikerling, A. A. Kornyshev, A. M. Kuznetsov, J. Ulstrup, and S. Walbran. “Mechanisms of Proton Conductance in Polymer Electrolyte Membranes”. *The Journal of Physical Chemistry B*, vol. 105, no. 17. 2001. DOI: 10.1021/jp003182s (cit. on p. 23).

[Esco2020] J. Escorihuela, A. García-Bernabé, and V. Compañ. “A deep insight into different acidic additives as doping agents for enhancing proton conductivity on polybenzimidazole membranes”. *Polymers*, vol. 12, no. 6. 2020. DOI: 10.3390/POLYM12061374 (cit. on p. 24).

[Faro1977] M. Farooque and T. Z. Fahidy. “Low Potential Oxidation of Hydrogen Sulfide on a Rotating Tripolar Wiper-Blade Electrode via Continuous Anode Reactivation”. *Journal of The Electrochemical Society*, vol. 124, no. 8. 1977. DOI: 10.1149/1.2133526 (cit. on pp. 59, 78).

[Feng2005] J. Feng, Q. Gao, L. Xu, and J. Wang. “Nonlinear phenomena in the electrochemical oxidation of sulfide”. *Electrochemistry Communications*, vol. 7, no. 12. 2005. DOI: 10.1016/j.elecom.2005.10.004 (cit. on p. 78).

[Feng2011] S. Feng and G. A. Voth. “Proton Solvation and Transport in Hydrated Nafion”. *The Journal of Physical Chemistry B*, vol. 115, no. 19. 2011. DOI: 10.1021/jp2002194 (cit. on p. 23).

[Fran2024] A. Franco and C. Giovannini. “Hydrogen Gas Compression for Efficient Storage: Balancing Energy and Increasing Density”. *Hydrogen*, vol. 5, no. 2. 2024. DOI: 10.3390/hydrogen5020017 (cit. on pp. 1, 9, 18–20).

[Gard2007] C. L. Gardner and M. Ternan. “Electrochemical separation of hydrogen from reformate using PEM fuel cell technology”. *Journal of Power Sources*, vol. 171, no. 2. 2007. DOI: 10.1016/j.jpowsour.2007.06.020 (cit. on p. 68).

[Gard2009] A. Gardiner, “Energy requirements for hydrogen gas compression and liquefaction as related to vehicle storage needs”, Department of Energy, United States of America, Tech. Rep. 9013, 2009. (visited on 12/20/2024) (cit. on p. 125).

[Gebe1997] G. Gebel and J. Lambard. “Small-Angle Scattering Study of Water-Swollen Perfluorinated Ionomer Membranes”. *Macromolecules*, vol. 30, no. 25. 1997. DOI: 10.1021/ma970801v (cit. on p. 23).

[Gebe2000] G. Gebel. “Structural evolution of water swollen perfluorosulfonated ionomers from dry membrane to solution”. *Polymer*, vol. 41. 2000. DOI: 10.1016/S0032-3861(99)00770-3 (cit. on p. 24).

[Gome2018] Y. A. Gomez, A. Oyarce, G. Lindbergh, and C. Lagergren. “Ammonia Contamination of a Proton Exchange Membrane Fuel Cell”. *Journal of The Electrochemical Society*, vol. 165, no. 3. 2018. DOI: 10.1149/2.0761803jes (cit. on pp. 59, 60).

[Gong2023] M. Gong, C. Jin, and Y. Na. “Minimizing Area-Specific Resistance of Electrochemical Hydrogen Compressor under Various Operating Conditions Using Unsteady 3D Single-Channel Model”. *Membranes*, vol. 13, no. 6. 2023. DOI: 10.3390/membranes13060555 (cit. on p. 91).

[Grig2011] S. A. Grigoriev, I. G. Shtatniy, P. Millet, V. I. Porembsky, and V. N. Fateev. “Description and characterization of an electrochemical hydrogen compressor/concentrator based on solid polymer electrolyte technology”. *International Journal of Hydrogen Energy*, vol. 36, no. 6. 2011. DOI: 10.1016/j.ijhydene.2010.07.012 (cit. on p. 43).

[Hals2006] R. Halseid, P. J. Vie, and R. Tunold. “Effect of ammonia on the performance of polymer electrolyte membrane fuel cells”. *Journal of Power Sources*, vol. 154, no. 2. 2006. DOI: 10.1016/j.jpowsour.2005.10.011 (cit. on p. 59).

[Hals2007] R. Halseid, J. S. Wainright, R. F. Savinell, and R. Tunold. “Oxidation of Ammonium on Platinum in Acidic Solutions”. *Journal of The Electrochemical Society*, vol. 154, no. 2. 2007. DOI: 10.1149/1.2405851 (cit. on p. 71).

[He2006] R. He, Q. Li, A. Bach, J. O. Jensen, and N. J. Bjerrum. “Physicochemical properties of phosphoric acid doped polybenzimidazole membranes for fuel cells”. *Journal of Membrane Science*, vol. 277, no. 1-2. 2006. DOI: 10.1016/j.memsci.2005.10.005 (cit. on p. 48).

[Hert2018] E. G. Hertwich and R. Wood. “The growing importance of scope 3 greenhouse gas emissions from industry”. *Environmental Research Letters*, vol. 13, no. 10. 2018. DOI: 10.1088/1748-9326/aae19a (cit. on p. 1).

[HyET] HyET Hydrogen, *Technology and Performance*. [Online]. Available: https://hyethydrogen.com/technology/ (visited on 04/02/2025) (cit. on p. 20).

[Ibeh2007] B. Ibeh, C. Gardner, and M. Ternan. “Separation of hydrogen from a hydrogen/methane mixture using a PEM fuel cell”. *International Journal of Hydrogen Energy*, vol. 32, no. 7. 2007. DOI: 10.1016/j.ijhydene.2006.11.017 (cit. on pp. 118–121).

[Inte2020] International Renewable Energy Agency, “Green hydrogen cost reduction: Scaling up electrolysers to meet the 1.5°C climate goal”, IRENA, Abu Dhabi, Tech. Rep., 2020, ISBN: 978-92-9260-295-6 (cit. on p. 5).

[Inte2024] International Organization for Standardization, *ISO/DIS 14687:2024 Hydrogen fuel quality - Product specification*, 2024 (cit. on p. 60).

[Isor2019] F. Isorna Llerena, A. de las Heras Jiménez, E. López González, F. Segura Manzano, and J. M. Andújar Márquez. “Effects of Ammonia Impurities on the Hydrogen Flow in High and Low Temperature Polymer Electrolyte Fuel Cells”. *Fuel Cells*, vol. 19, no. 6. 2019. DOI: 10.1002/fuce.201900031 (cit. on p. 59).

[Jack2020] C. Jackson, L. F. Raymakers, M. J. Mulder, and A. R. Kucernak. “Poison mitigation strategies for the use of impure hydrogen in electrochemical hydrogen pumps and fuel cells”. *Journal of Power Sources*, vol. 472. 2020. DOI: 10.1016/j.jpowsour.2020.228476 (cit. on pp. 60, 62, 78, 79, 81, 92).

[Jack2023] C. Jackson, G. Smith, and A. R. Kucernak. “Deblending and purification of hydrogen from natural gas mixtures using the electrochemical hydrogen pump”. *International Journal of Hydrogen Energy*, vol. 52, no. Part B. 2023. DOI: 10.1016/j.ijhydene.2023.05.065 (cit. on pp. 21, 60, 62).

[Jusy2001] Z. Jusys and R. J. Behm. “Electrooxidation of CO and H_2/CO mixtures on a carbon-supported Pt catalyst—a kinetic and mechanistic study by differential electrochemical mass spectrometry”. *Physical Chemistry Chemical Physics*, vol. 3, no. 21. 2001. DOI: 10.1021/jp011510y (cit. on p. 68).

[Kane2022] K. Kanellopoulos, S. Busch, M. De Felice, S. Giaccaria, and A. Costescu, “Blending hydrogen from electrolysis into the European gas grid A joint modelling assessment of the European Power and Gas systems with METIS”, Publications Office of the European Union, Tech. Rep. EUR 30951 EN, 2022, ISBN: 9789276463467. DOI: 10.2760/908387 (cit. on p. 57).

[Ke2023] S. Ke, C. Sun, B. Cui, Y. Qin, and M. Dou. “Operatable and Efficient Mitigation Strategies for H_2S Poisoning in Proton Exchange Membrane Fuel Cells: Releasing Pt Reactive Sites for Hydrogen Oxidation”. *ACS Applied Energy Materials*, vol. 6, no. 6. 2023. DOI: 10.1021/acsaem.2c04026 (cit. on p. 81).

[Kee2019] B. L. Kee, D. Curran, H. Zhu, R. J. Braun, S. C. DeCaluwe, R. J. Kee, and S. Ricote. “Thermodynamic insights for electrochemical hydrogen compression with proton-conducting membranes”. *Membranes*, vol. 9, no. 7. 2019. DOI: 10.3390/membranes9070077 (cit. on pp. 2, 17, 18, 21, 33).

[Kim2022] C. Kim, M. Gong, J. Lee, and Y. Na. “Minimizing Specific Energy Consumption of Electrochemical Hydrogen Compressor at Various Operating Conditions Using Pseudo-2D Model Simulation”. *Membranes*, vol. 12, no. 1214. 2022. DOI: 10.3390/membranes12121214 (cit. on p. 124).

[Kreu1982] K.-D. Kreuer, A. Rabenau, and W. Weppner. “Vehicle Mechanism, A New Model for the Interpretation of the Conductivity of Fast Proton Conductors”. *Angewandte Chemie International Edition in English*, vol. 21, no. 3. 1982. DOI: 10.1002/anie.198202082 (cit. on pp. 22, 23).

[Kris1997] R. Krishna and J. Wesselingh. “The Maxwell-Stefan approach to mass transfer”. *Chemical Engineering Science*, vol. 52, no. 6. 1997. DOI: 10.1016/S0009-2509(96)00458-7 (cit. on p. 101).

[Lamb2021] W. F. Lamb *et al.* “A review of trends and drivers of greenhouse gas emissions by sector from 1990 to 2018”. *Environmental Research Letters*, vol. 16, no. 7. 2021. DOI: 10.1088/1748-9326/abee4e (cit. on p. 1).

[Lang1969] S. H. Langer and R. G. Hademan, “Electrolytic hydrogen purification and recovery of same”, US 3475302, 1969 (cit. on p. 15).

[Laub2022] A. Laube, A. Hofer, B. Sánchez Batalla, S. Ressel, A. Chica, S. Fischer, C. Weidlich, J. Bachmann, and T. Struckmann. “Tubular membrane electrode assembly for PEM electrolysis”. *International Journal of Hydrogen Energy*, vol. 7. 2022. DOI: 10.1016/j.ijhydene.2022.03.135 (cit. on p. 92).

[Laub2023] A. Laube, B. Sánchez Batalla, C. Weidlich, A. Hofer, J. Bachmann, S. Zallmann, C. Körner, S. Fischer, A. Chica, and T. Struckmann. “Tubular PEM electrolysis cells with a 3D-printed oxygen electrode and ALD catalyst coating”. *International Journal of Hydrogen Energy*, vol. 49, no. Part C. 2023. DOI: 10.1016/j.ijhydene.2023.08.084 (cit. on p. 92).

[Laza2023] A. C. Lazanas and M. I. Prodromidis. “Electrochemical Impedance SpectroscopyA Tutorial”. *ACS Measurement Science Au*, vol. 3, no. 3. 2023. DOI: 10.1021/acsmeasuresciau.2c00070 (cit. on p. 27).

[Li2020] N. Li, S. S. Araya, X. Cui, and S. K. Kær. “The effects of cationic impurities on the performance of proton exchange membrane water electrolyzer”. *Journal of Power Sources*, vol. 473, no. 228617. 2020. DOI: 10.1016/j.jpowsour.2020.228617 (cit. on p. 117).

[Liem2017] W. Liemberger, M. Groß, M. Miltner, and M. Harasek. “Experimental analysis of membrane and pressure swing adsorption (PSA) for the hydrogen separation from natural gas”. *Journal of Cleaner Production*, vol. 167. 2017. DOI: 10.1016/j.jclepro.2017.08.012 (cit. on pp. 11, 125).

[Lim2023] K. H. Lim, I. Matanovic, S. Maurya, Y. Kim, E. S. De Castro, J. H. Jang, H. Park, and Y. S. Kim. “High Temperature Polymer Electrolyte Membrane Fuel Cells with High Phosphoric Acid Retention”. *ACS Energy Letters*, vol. 8, no. 1. 2023. DOI: 10.1021/acsenergylett.2c02367 (cit. on p. 61).

[Limp2022] A. Limper, N. Weber, A. Brodersen, R. Keller, M. Wessling, and J. Linkhorst. “Additive manufacturing of composite porosity mixer electrodes”. *Electrochemistry Communications*, vol. 134, no. 107176. 2022. DOI: 10.1016/j.elecom.2021.107176 (cit. on p. 93).

[Lins] P. Linstrom J. and W. Mallard. “Gas phase thermochemistry data”, in: *NIST Chemistry WebBook, NIST Standard Reference Database Number 69*. Gaithersburg MD, 20899, USA: National Institute of Standards and Technology. (Cit. on p. 106).

[Lope2011] T. Lopes, V. A. Paganin, and E. R. Gonzalez. “Hydrogen sulfide tolerance of palladium-copper catalysts for PEM fuel cell anode applications”. *International Journal of Hydrogen Energy*, vol. 36, no. 21. 2011. DOI: 10.1016/j.ijhydene.2011.07.126 (cit. on pp. 81, 82).

[Louc1971] T. Loucka. “Adsorption and oxidation of sulphur and of sulphur dioxide at the platinum electrode”. *Journal of Electroanalytical Chemistry and Interfacial Electrochemistry*, vol. 31, no. 2. 1971. DOI: 10.1016/S0022-0728(71)80162-6 (cit. on p. 80).

[Lu2016] S. Lu and Z. Zhuang. “Electrocatalysts for hydrogen oxidation and evolution reactions”. *Science China Materials*, vol. 59, no. 3. 2016. DOI: 10.1007/s40843-016-0127-9 (cit. on p. 22).

[Lube2022] M. Luberti and H. Ahn. “Review of Polybed pressure swing adsorption for hydrogen purification”. *International Journal of Hydrogen Energy*, vol. 47, no. 20. 2022. DOI: 10.1016/j.ijhydene.2022.01.147 (cit. on pp. 9, 11).

[Ludu2011] G. A. Ludueña, T. D. Kühne, and D. Sebastiani. “Mixed Grotthuss and Vehicle Transport Mechanism in Proton Conducting Polymers from Ab initio Molecular Dynamics Simulations”. *Chemistry of Materials*, vol. 23, no. 6. 2011. DOI: 10.1021/cm102674u (cit. on p. 23).

[Luka2016] M. Lukaszewski, M. Soszko, and A. Czerwiński. “Electrochemical methods of real surface area determination of noble metal electrodes - an overview”. *International Journal of Electrochemical Science*, vol. 11, no. 6. 2016. DOI: 10.20964/2016.06.71 (cit. on pp. 29, 65).

[Ma2004] Y.-L. Ma, J. S. Wainright, M. H. Litt, and R. F. Savinell. “Conductivity of PBI Membranes for High-Temperature Polymer Electrolyte Fuel Cells”. *Journal of The Electrochemical Society*, vol. 151, no. 1. 2004. DOI: 10.1149/1.1630037 (cit. on pp. 24, 33, 43–46).

[Mage1970] H. J. R. Maget, “Process for Gas Purification”, US 3489670, 1970 (cit. on p. 15).

[Maha2022] D. Mahajan, K. Tan, T. Venkatesh, P. Kileti, and C. R. Clayton. “Hydrogen Blending in Gas Pipeline Networks—A Review”. *Energies*, vol. 15, no. 10. 2022. DOI: 10.3390/en15103582 (cit. on pp. 2, 57).

[Male2009] D. Malevich, E. Halliop, B. A. Peppley, J. G. Pharoah, and K. Karan. “Investigation of Charge-Transfer and Mass-Transport Resistances in PEMFCs with Microporous Layer Using Electrochemical Impedance Spectroscopy”. *Journal of The Electrochemical Society*, vol. 156, no. 2. 2009. DOI: 10.1149/1.3033408 (cit. on p. 46).

[Maxw2023] D. S. Maxwell, Q. Sun, H. Rojas, R. Kendrick, R. K. Pavlicek, E. S. D. Castro, A. Aurora, and S. Mukerjee. “High Purity Hydrogen Separation with HT-PBI Based Electrochemical Pump Operation at 120°C”. *Journal of The Electrochemical Society*, vol. 170, no. 034510. 2023. DOI: 10.1149/1945-7111/acc6f7 (cit. on pp. 21, 34, 41, 61, 62, 92).

[McPh2017] I. J. McPherson, P. A. Ash, L. Jones, A. Varambhia, R. M. Jacobs, and K. A. Vincent. “Electrochemical CO Oxidation at Platinum on Carbon Studied through Analysis of Anomalous in Situ IR Spectra”. *Journal of Physical Chemistry C*, vol. 121, no. 32. 2017. DOI: 10.1021/acs.jpcc.7b02166 (cit. on p. 66).

[Mela2013] M. Melaina, O. Antonia, and M. Penev, “Blending hydrogen into natural gas pipelines networks: A review of key issues”, National Renewable Energy Laboratory, Golden, Colorado, Tech. Rep., 2013, Publication Title: Technical Report NREL/TP-500-51995 Issue: March (cit. on pp. 2, 57).

[Melc2017a] J. P. Melchior, G. Majer, and K. D. Kreuer. “Why do proton conducting polybenzimidazole phosphoric acid membranes perform well in high-temperature PEM fuel cells?”, *Physical Chemistry Chemical Physics*, vol. 19, no. 1. 2017. DOI: 10.1039/c6cp05331a (cit. on pp. 33, 43).

[Melc2017b] J.-P. Melchior, K.-D. Kreuer, and J. Maier. “Proton conduction mechanisms in the phosphoric acid–water system ($H_4P_2O_7$ – $H_3PO_4 \cdot 2H_2O$): A ^{1}H, ^{31}P and ^{17}O PFG-NMR and conductivity study”. *Physical Chemistry Chemical Physics*, vol. 19, no. 1. 2017. DOI: 10.1039/C6CP04855B (cit. on p. 25).

[Méri2006] W. Mérida, D. A. Harrington, J. M. Le Canut, and G. McLean. “Characterisation of proton exchange membrane fuel cell (PEMFC) failures via electrochemical impedance spectroscopy”. *Journal of Power Sources*, vol. 161, no. 1. 2006. DOI: 10.1016/j.jpowsour.2006.03.067 (cit. on pp. 115, 116).

[Miya2013] A. Miyazawa, E. Tada, and A. Nishikata. “Influence of corrosion of SS316L bipolar plate on PEFC performance”. *Journal of Power Sources*, vol. 231. 2013. DOI: 10.1016/j.jpowsour.2012.12.088 (cit. on p. 117).

[Mohs2023] M. Mohseni, D. Felder, K. Percin, M. Thönes, M. Gassenmeier, R. Kupec, C. Weidlich, J. Linkhorst, R. G. Keller, and M. Wessling. “Toward decentralized wastewater treatment: A flow-through module using microtubular gas diffusion electrodes for micropollutants removal”. *Journal of Hazardous Materials*, vol. 458. 2023. DOI: 10.1016/j.jhazmat.2023.131987 (cit. on p. 92).

[Moht2005] R. Mohtadi, W. K. Lee, and J. W. Van Zee. “The effect of temperature on the adsorption rate of hydrogen sulfide on Pt anodes in a PEMFC”. *Applied Catalysis B: Environmental*, vol. 56, no. 1-2. 2005. DOI: 10.1016/j.apcatb.2004.08.012 (cit. on p. 81).

[Mrus2024] S. Mrusek, M. Blasius, F. Morgenroth, S. Thiele, and P. Wasserscheid. “Hydrogen extraction from methane-hydrogen mixtures from the natural gas grid by means of electrochemical hydrogen separation and compression”. *International Journal of Hydrogen Energy*, vol. 50, no. Part A. 2024. DOI: 10.1016/j.ijhydene.2023.08.195 (cit. on pp. 2, 58, 60, 62).

[Mu2019] Y.-T. Mu, A. Z. Weber, Z.-L. Gu, and W.-Q. Tao. “Mesoscopic modeling of transport resistances in a polymer-electrolyte fuel-cell catalyst layer: Analysis of hydrogen limiting currents”. *Applied Energy*, vol. 255. 2019. DOI: 10.1016/j.apenergy.2019.113895 (cit. on p. 103).

[Muka2016] M. Mukaddam, E. Litwiller, and I. Pinnau. “Gas Sorption, Diffusion, and Permeation in Nafion”. *Macromolecules*, vol. 49, no. 1. 2016. DOI: 10.1021/acs.macromol.5b02578 (cit. on p. 105).

[Nase2012] M. M. Nasef and A. A. Aly. “Water and charge transport models in proton exchange membranes: An overview”. *Desalination*, vol. 287. 2012. DOI: 10.1016/j.desal.2011.06.054 (cit. on p. 23).

[Nguy2011] M. T. Nguyen, S. A. Grigoriev, A. A. Kalinnikov, A. A. Filippov, P. Millet, and V. N. Fateev. “Characterisation of a electrochemical hydrogen pump using electrochemical impedance spectroscopy”. *Journal of Applied Electrochemistry*, vol. 41, no. 9. 2011. DOI: 10.1007/s10800-011-0341-9 (cit. on pp. 21, 28, 116).

[Nord2019] M. Nordio, F. Rizzi, G. Manzolini, M. Mulder, L. Raymakers, M. Van Sint Annaland, and F. Gallucci. “Experimental and modelling study of an electrochemical hydrogen compressor”. *Chemical Engineering Journal*, vol. 369. 2019. DOI: 10.1016/j.cej.2019.03.106 (cit. on pp. 2, 58, 91, 125).

[Nord2020] M. Nordio, M. Eguaras Barain, L. Raymakers, M. Van Sint Annaland, M. Mulder, and F. Gallucci. “Effect of CO_2 on the performance of an electrochemical hydrogen compressor”. *Chemical Engineering Journal*, vol. 392. 2020. DOI: 10.1016/j.cej.2019.123647 (cit. on pp. 58, 60, 62, 66).

[Nord2021] M. Nordio, S. A. Wassie, M. Van Sint Annaland, D. A. Pacheco Tanaka, J. L. Viviente Sole, and F. Gallucci. “Techno-economic evaluation on a hybrid technology for low hydrogen concentration separation and purification from natural gas grid”. *International Journal of Hydrogen Energy*, vol. 46, no. 45. 2021. DOI: 10.1016/j.ijhydene.2020.05.009 (cit. on pp. 9, 11, 57).

[Onda2007] K. Onda, K. Ichihara, M. Nagahama, Y. Minamoto, and T. Araki. “Separation and compression characteristics of hydrogen by use of proton exchange membrane”. *Journal of Power Sources*, vol. 164, no. 1. 2007. DOI: 10.1016/j.jpowsour.2006.10.018 (cit. on pp. 118–121).

[Padd2005] S. J. Paddison and J. A. Elliott. “Molecular Modeling of the Short-Side-Chain Perfluorosulfonic Acid Membrane”. *The Journal of Physical Chemistry A*, vol. 109, no. 33. 2005. DOI: 10.1021/jp0524734 (cit. on p. 23).

[Pawe2020] G. Pawelec, M. Muron, J. Bracht, B. Bonnet-Cantalloube, A. Floristean, and N. Brahy, “Hydrogen demand and supply in the EU”, Hydrogen Europe Intelligence Departmen, Tech. Rep., 2020, Publication Title: Hydrogen Europe Clean Hydrogen Monitor. [Online]. Available: https://hydrogeneurope.eu/hydrogen-transport-distribution (cit. on p. 57).

[Perr2008] K. A. Perry, G. A. Eisman, and B. C. Benicewicz. “Electrochemical hydrogen pumping using a high-temperature polybenzimidazole (PBI) membrane”. *Journal of Power Sources*, vol. 177, no. 2. 2008. DOI: 10.1016/j.jpowsour.2007.11.059 (cit. on pp. 21, 34, 45, 61).

[Perr2014] K. A. Perry, K. L. More, E. A. Payzant, R. A. Meisner, B. G. Sumpter, and B. C. Benicewicz. “A comparative study of phosphoric acid-doped m-PBI membranes”. *Journal of Polymer Science, Part B: Polymer Physics*, vol. 52, no. 1. 2014. DOI: 10.1002/polb.23403 (cit. on p. 25).

[Pesc2020] A. Peschel. “Industrial Perspective on Hydrogen Purification, Compression, Storage, and Distribution”. *Fuel Cells*, vol. 20, no. 4. 2020. DOI: 10.1002/fuce.201900235 (cit. on p. 9).

[Pine2022a] J. L. Pineda-Delgado, A. U. Chávez-Ramirez, C. K. Gutierrez B, S. Rivas, C. R. Marisela, R. de Jesús Hernández-Cortes, J. A. Menchaca-Rivera, and J. F. Pérez-Robles. “Effect of relative humidity and temperature on the performance of an electrochemical hydrogen compressor”. *Applied Energy*, vol. 311, no. 118617. 2022. DOI: 10.1016/j.apenergy.2022.118617 (cit. on pp. 33, 43, 114, 117).

[Pine2022b] J. L. Pineda-Delgado, J. A. Menchaca-Rivera, J. F. Pérez-Robles, L. M. Aviles-Arellano, A. U. Chávez-Ramirez, C. K. Gutierrez B., R. de Jesús Hernández-Cortes, J. G. Rivera, and S. Rivas. “Energetic evaluations of an electrochemical hydrogen compressor”. *Journal*

of Energy Storage, vol. 55, no. 105675. 2022. DOI: 10.1016/j.est.2022.105675 (cit. on pp. 17, 18).

[Piva2024] I. Pivac, A. S. Pavasović, and F. Barbir. “Recent advances and perspectives in diagnostics and degradation of electrochemical hydrogen compressors”. *International Journal of Hydrogen Energy*, vol. 54. 2024. DOI: 10.1016/j.ijhydene.2023.01.281 (cit. on pp. 2, 19, 91, 114).

[Prok2025] G. I. Prokopou, J. M. Faust, A. Mitsos, and D. Bongartz. “Cost-optimal design and operation of hydrogen refueling stations with mechanical and electrochemical hydrogen compressors”. *Computers and Chemical Engineering*, vol. 192, no. 108862. 2025. DOI: 10.1016/j.compchemeng.2024.108862 (cit. on pp. 19, 20).

[Purr2021] O. Purrucker and J. Balster. “Hydrogen on tap: Supporting decarbonization by pipelining H_2 to the point of use”. *H2T Special Focus - Future of Hydrogen Energy*. 2021. (Cit. on p. 11).

[Quar2012] E. Quartarone and P. Mustarelli. “Polymer fuel cells based on polybenzimidazole/H_3PO_4”. *Energy & Environmental Science*, vol. 5, no. 4. 2012. DOI: 10.1039/C2EE03055A (cit. on p. 24).

[Rabi2022] H. Rabiee, L. Ge, S. Hu, H. Wang, and Z. Yuan. “Microtubular electrodes: An emerging electrode configuration for electrocatalysis, bioelectrochemical and water treatment applications”. *Chemical Engineering Journal*, vol. 450, no. Part 1. 2022. DOI: 10.1016/j.cej.2022.138476 (cit. on p. 92).

[Relv2018] F. Relvas, R. D. Whitley, C. Silva, and A. Mendes. “Single-Stage Pressure Swing Adsorption for Producing Fuel Cell Grade Hydrogen”. *Industrial and Engineering Chemistry Research*, vol. 57, no. 14. 2018. DOI: 10.1021/acs.iecr.7b05410 (cit. on pp. 10, 57).

[Rhan2020] M. Rhandi, M. Trégaro, F. Druart, J. Deseure, M. Chatenet, M. Trégaro, F. Druart, J. Deseure, M. Chatenet, M. Rhandi, F. Druart, J. Deseure, M. Chatenet, M. Trégaro, F. Druart, J. Deseure, and M. Chatenet. “Electrochemical hydrogen compression and purification versus competing technologies: Part I. Pros and cons”. *Chinese Journal of Catalysis*, vol. 41, no. 5. 2020. DOI: 10.1016/S1872-2067(19)63404-2 (cit. on pp. 2, 91).

[Rico2018] A. Rico-Zavala, M. P. Gurrola, L. G. Arriaga, J. A. Bañuelos, L. Álvarez-Contreras, A. Carbone, A. Saccà, F. V. Matera, R. Pedicini, A. Álvarez, and J. Ledesma-García. “Synthesis and characterization of composite membranes modified with Halloysite nanotubes and phosphotungstic acid for electrochemical hydrogen pumps”. *Renewable Energy*, vol. 122. 2018. DOI: 10.1016/j.renene.2018.01.054 (cit. on pp. 21, 92).

[Riec1997] C. Rieckmann and F. J. Keil. “Multicomponent Diffusion and Reaction in Three-Dimensional Networks: General Kinetics”. *Industrial & Engineering Chemistry Research*, vol. 36, no. 8. 1997. DOI: 10.1021/ie9605847 (cit. on p. 102).

[Sabh2019] M. Sabharwal, L. M. Pant, N. Patel, and M. Secanell. “Computational Analysis of Gas Transport in Fuel Cell Catalyst Layer under Dry and Partially Saturated Conditions”. *Journal of The Electrochemical Society*, vol. 166, no. 7. 2019. DOI: 10.1149/2.0081907jes (cit. on p. 103).

[Sahr2024] E. Sahraie, I. Kamwa, A. Moeini, and S. M. Mohseni-Bonab. “Component and system levels limitations in power-hydrogen systems: Analytical review”. *Energy Strategy Reviews*, vol. 54, no. 101476. 2024. DOI: 10.1016/j.esr.2024.101476 (cit. on p. 1).

[Sava2014] J. Savage, Y.-L. S. Tse, and G. A. Voth. “Proton Transport Mechanism of Perfluorosulfonic Acid Membranes”. *The Journal of Physical Chemistry C*, vol. 118, no. 31. 2014. DOI: 10.1021/jp504714d (cit. on p. 23).

[Scha2015] M. Schalenbach, T. Hoefner, P. Paciok, M. Carmo, W. Lueke, and D. Stolten. “Gas Permeation through Nafion. Part 1: Measurements”. *Journal of Physical Chemistry C*, vol. 119, no. 45. 2015. DOI: 10.1021/acs.jpcc.5b04155 (cit. on p. 48).

[Scho2021] D. Schonvogel, J. Büsselmann, H. Schmies, H. Langnickel, P. Wagner, and A. Dyck. “High temperature polymer electrolyte membrane fuel cell degradation provoked by ammonia as ambient air contaminant”. *Journal of Power Sources*, vol. 502. 2021. DOI: 10.1016/j.jpowsour.2021.229993 (cit. on pp. 59, 71).

[Sdan2019a] G. Sdanghi, G. Maranzana, A. Celzard, and V. Fierro. “Review of the current technologies and performances of hydrogen compression for stationary and automotive applications”. *Renewable and Sustainable Energy Reviews*, vol. 102. 2019. DOI: 10.1016/j.rser.2018.11.028 (cit. on pp. 9, 19).

[Sdan2019b] G. Sdanghi, J. Dillet, S. Didierjean, and V. Fierro. “Experimental evidence of local heterogeneities in a PEM Electrochemical Hydrogen Compressor”, in: *European Fuel Cells Forum 2019*, vol. hal-02186543, Lucerne, France, 2019. (Cit. on pp. 91, 107).

[Sdan2020] G. Sdanghi, J. Dillet, S. Didierjean, V. Fierro, and G. Maranzana. “Feasibility of Hydrogen Compression in an Electrochemical System: Focus on Water Transport Mechanisms”. *Fuel Cells*, vol. 20, no. 3. 2020. DOI: 10.1002/fuce.201900068 (cit. on pp. 91, 102, 105).

[Seel2009] D. C. Seel, B. C. Benicewicz, L. Xiao, and T. J. Schmidt. “High-temperature polybenzimidazole-based membranes”, in: *Handbook of Fuel Cells – Fundamentals, Technology and Applications*. W. Vielstich, H. Yokokawa, and H. A. Gasteiger, Eds., vol. 5, John Wiley & Sons, Ltd., 2009. ISBN: 978-0-470-72311-1. (Cit. on p. 24).

[Seth2010] V. A. Sethuraman and J. W. Weidner. “Analysis of sulfur poisoning on a PEM fuel cell electrode”. *Electrochimica Acta*, vol. 55, no. 20. 2010. DOI: 10.1016/j.electacta.2010.05.004 (cit. on pp. 59, 78, 81, 83).

[Soto2003] H. J. Soto, W. K. Lee, J. W. Van Zee, and M. Murthy. “Effect of transient ammonia concentrations on PEMFC performance”. *Electrochemical and Solid-State Letters*, vol. 6, no. 7. 2003. DOI: 10.1149/1.1574651 (cit. on p. 71).

[Spin2017] F. B. Spingler, A. Phillips, T. Schuler, M. C. Tucker, and A. Z. Weber. “Investigating fuel-cell transport limitations using hydrogen limiting current”. *International Journal of Hydrogen Energy*, vol. 42, no. 19. 2017. DOI: 10.1016/j.ijhydene.2017.01.036 (cit. on p. 126).

[Spri1991] T. E. Springer, T. A. Zawodzinski, and S. Gottesfeld. “Polymer Electrolyte Fuel Cell Model”. *Journal of The Electrochemical Society*, vol. 138, no. 8. 1991. DOI: 10.1149/1.2085971 (cit. on pp. 105–107).

[Staf2019] I. Staffell, D. Scamman, A. Velazquez Abad, P. Balcombe, P. E. Dodds, P. Ekins, N. Shah, and K. R. Ward. “The role of hydrogen and fuel cells in the global energy system”. *Energy and Environmental Science*, vol. 12, no. 2. 2019. DOI: 10.1039/c8ee01157e (cit. on p. 91).

[Strö2002] R. Ströbel, M. Oszcipok, M. Fasil, B. Rohland, L. Jörissen, and J. Garche. “The compression of hydrogen in an electrochemical cell based on a PE fuel cell design”. *Journal of Power Sources*, vol. 105, no. 2. 2002. DOI: 10.1016/S0378-7753(01)00941-7 (cit. on pp. 107, 113).

[Suer2017] M. Suermann, T. Kiupel, T. J. Schmidt, and F. N. Büchi. “Electrochemical Hydrogen Compression: Efficient Pressurization Concept Derived from an Energetic Evaluation”. *Journal of The Electrochemical Society*, vol. 164, no. 12. 2017. DOI: 10.1149/2.1361712jes (cit. on p. 18).

[Taha2022] M.-R. Tahan. “Recent advances in hydrogen compressors for use in large-scale renewable energy integration”. *International Journal of Hydrogen Energy*, vol. 47, no. 83. 2022. DOI: 10.1016/j.ijhydene.2022.08.128 (cit. on p. 18).

[Togh2020] S. Toghyani, E. Baniasadi, E. Afshari, and N. Javani. “Performance analysis and exergoeconomic assessment of a proton exchange membrane compressor for electrochemical hydrogen storage”. *International Journal of Hydrogen Energy*, vol. 45, no. 60. 2020. DOI: 10.1016/j.ijhydene.2020.01.232 (cit. on pp. 91, 106).

[Tras1992] S. Trasatti and O. Petrii. “Real surface area measurements in electrochemistry”. *Journal of Electroanalytic Chemistry*, vol. 327, no. 1-2. 1992. DOI: 10.1016/0926-860x(96)80148-7 (cit. on p. 65).

[Trég2020] M. Trégaro, M. Rhandi, F. Druart, J. Deseure, and M. Chatenet. “Electrochemical hydrogen compression and purification versus competing technologies: Part II. Challenges in electrocatalysis”. *Chinese Journal of Catalysis*, vol. 41, no. 5. 2020. DOI: 10.1016/S1872-2067(19)63438-8 (cit. on pp. 19, 22, 58, 61, 68, 91).

[Urib2002] F. A. Uribe, S. Gottesfeld, and T. A. Zawodzinski. “Effect of Ammonia as Potential Fuel Impurity on Proton Exchange Membrane Fuel Cell Performance”. *Journal of The Electrochemical Society*, vol. 149, no. 3. 2002. DOI: 10.1149/1.1447221 (cit. on pp. 60, 71).

[US D2015] U.S. Department of Energy, “Technical Targets for Hydrogen Delivery”, Tech. Rep., 2015. [Online]. Available: https://www.energy.gov/eere/fuelcells/doe-technical-targets-hydrogen-delivery (visited on 02/04/2025) (cit. on p. 20).

[Vald2020] V. F. Valdés-López, T. Mason, P. R. Shearing, and D. J. Brett. “Carbon monoxide poisoning and mitigation strategies for polymer electrolyte membrane fuel cells – A review”. *Progress in Energy and Combustion Science*, vol. 79. 2020. DOI: 10.1016/j.pecs.2020.100842 (cit. on p. 58).

[vdSpek2022] M. van der Spek, C. Banet, C. Bauer, P. Gabrielli, W. Goldthorpe, M. Mazzotti, S. T. Munkejord, N. A. Røkke, N. Shah, N. Sunny, D. Sutter, J. M. Trusler, and M. Gazzani. “Perspective on the hydrogen economy as a pathway to reach net-zero CO_2 emissions in Europe”. *Energy and Environmental Science*, vol. 15, no. 3. 2022. DOI: 10.1039/d1ee02118d (cit. on p. 91).

[Verm2021a] L. Vermaak, H. W. J. P. Neomagus, and D. G. Bessarabov. “Hydrogen Separation and Purification from Various Gas Mixtures by Means of Electrochemical Membrane Technology in the Temperature Range 100 – 160°C”. *Membranes*, vol. 11, no. 4. 2021. DOI: 10.3390/membranes11040282 (cit. on p. 61).

[Verm2021b] L. Vermaak, H. W. Neomagus, and D. G. Bessarabov. “Recent advances in membrane-based electrochemical hydrogen separation: A review”. *Membranes*, vol. 11, no. 2. 2021. DOI: 10.3390/membranes11020127 (cit. on pp. 20, 59, 62, 91).

[Vivi2021] V. Vivier and M. E. Orazem. “Impedance Analysis of Electrochemical Systems”. *Chemical Reviews*, vol. 122, no. 12. 2021. DOI: 10.1021/acs.chemrev.1c00876 (cit. on p. 27).

[Ward2011] T. Ward, X. Li, and A. Faghri. “Performance characteristics of a novel tubular-shaped passive direct methanol fuel cell”. *Journal of Power Sources*, vol. 196, no. 15. 2011. DOI: 10.1016/j.jpowsour.2011.04.012 (cit. on p. 92).

[Webe2023] N. Weber, J. Linkhorst, R. Keller, and M. Wessling. “Tailoring Pore Networks – Gas Diffusion Electrodes via Additive Manufacturing”. *Advanced Materials Technologies*, vol. 8, no. 21. 2023. DOI: 10.1002/admt.202300720 (cit. on p. 92).

[Wijm1995] J. Wijmans and R. Baker. “The solution-diffusion model: A review”. *Journal of Membrane Science*, vol. 107, no. 1-2. 1995. DOI: 10.1016/0376-7388(95)00102-I (cit. on p. 16).

[Wu2012] X. Wu, J. Benziger, and G. He. “Comparison of Pt and Pd catalysts for hydrogen pump separation from reformate”. *Journal of Power Sources*, vol. 218. 2012. DOI: 10.1016/j.jpowsour.2012.07.002 (cit. on pp. 22, 29, 92).

[Xiao2005] L. Xiao, H. Zhang, E. Scanlon, L. S. Ramanathan, E.-W. Choe, D. Rogers, T. Apple, and B. C. Benicewicz. “High-Temperature Polybenzimidazole Fuel Cell Membranes via a Sol-Gel Process”. *Chemistry of Materials*, vol. 17, no. 21. 2005. DOI: 10.1021/cm050831+ (cit. on p. 25).

[Xu2024] Z. Xu, N. Chen, S. Huang, S. Wang, D. Han, M. Xiao, and Y. Meng. “Strategies for Mitigating Phosphoric Acid Leaching in High-Temperature Proton Exchange Membrane Fuel Cells”. *Molecules*, vol. 29, no. 18. 2024. DOI: 10.3390/molecules29184480 (cit. on p. 34).

[Yanx2019] Z. Yanxing, G. Maoqiong, Z. Yuan, D. Xueqiang, and S. Jun. “Thermodynamics analysis of hydrogen storage based on compressed gaseous hydrogen, liquid hydrogen and cryo-compressed hydrogen”. *International Journal of Hydrogen Energy*, vol. 44, no. 31. 2019. DOI: 10.1016/j.ijhydene.2019.04.207 (cit. on p. 91).

[Yuan2010] X.-Z. Yuan, C. Song, H. Wang, and J. Zhang. *Electrochemical impedance spectroscopy in PEM fuel cells - Fundamentals and Applications*. London: Springer-Verlag, 2010. ISBN: 978-85-7811-079-6.DOI: 10.1007/978-1-84882-846-9 (cit. on p. 27).

[Yuan2014] J. Yuan and B. Sundén. “On mechanisms and models of multi-component gas diffusion in porous structures of fuel cell electrodes”. *International Journal of Heat and Mass Transfer*, vol. 69. 2014. DOI: 10.1016/j.ijheatmasstransfer.2013.10.032 (cit. on p. 103).

[Zach2021] L. Zachert, M. Suermann, B. Bensmann, and R. Hanke-Rauschenbach. “Energetic Evaluation and Optimization of Hydrogen Generation and Compression Pathways Considering PEM Water Electrolyzers and Electrochemical Hydrogen Compressors”. *Journal of The Electrochemical Society*, vol. 168, no. 1. 2021. DOI: 10.1149/1945-7111/abcf1a (cit. on p. 91).

[Zolf1999] A. Zolfaghari, M. Chayer, and G. Jerkiewicz. “Energetics of the Underpotential Deposition of Hydrogen on Platinum Electrodes: I. Absence of Coadsorbed Species”. *Journal of The Electrochemical Society*, vol. 146, no. 11. 1999. DOI: 10.1149/1.1837955 (cit. on p. 78).

[Zosk2007] C. G. Zoski. *Handbook of Electrochemistry*. C. G. Zoski, Ed. Amsterdam: Elsevier, 2007. ISBN: 978-0-444-51958-0.DOI: 10.1016/B978-044451958-0.50001-X (cit. on p. 16).

[Zou2020] J. Zou, N. Han, J. Yan, Q. Feng, Y. Wang, Z. Zhao, J. Fan, L. Zeng, H. Li, and H. Wang. “Electrochemical Compression Technologies for High-Pressure Hydrogen: Current Status, Challenges and Perspective”. *Electrochemical Energy Reviews*, vol. 3, no. 4. 2020. DOI: 10.1007/s41918-020-00077-0 (cit. on pp. 2, 9, 16, 19, 58, 91, 92).

[Zou2021] J. Zou, Y. Jin, Z. Wen, S. Xing, N. Han, K. Yao, Z. Zhao, M. Chen, J. Fan, H. Li, and H. Wang. “Insights into electrochemical hydrogen compressor operating parameters and membrane electrode assembly degradation mechanisms”. *Journal of Power Sources*, vol. 484, no. 229249. 2021. DOI: 10.1016/j.jpowsour.2020.229249 (cit. on pp. 20, 28, 113).

[Zou2023] J. Zou, H. Huang, S. Zaman, K. Yao, S. Xing, M. Chen, H. Wang, and M. Wang. “Enhanced electrochemical hydrogen compression performance with a gradient water-retaining hybrid membrane”. *Chemical Engineering Journal*, vol. 457, no. 141113. 2023. DOI: 10.1016/j.cej.2022.141113 (cit. on p. 92).

List of Symbols

Basics

δ	Thickness	(m)
$\dot{n}$	Molar flow rate	($\mathrm{mol\,s^{-1}}$)
$\dot{V}$	Volumetric flow rate	($\mathrm{m^3\,s^{-1}}$)
ρ	Density	($\mathrm{k\,g\,m^{-3}}$)
A	Area	($\mathrm{m^2}$)
a	Activity	(-)
c	Concentration	($\mathrm{mol\,m^{-3}}$)
M	Molar mass	($\mathrm{g\,mol^{-1}}$)
p	Pressure	(Pa)
p_i	Partial pressure	(Pa)
T	Temperature	(K or °C)
t	Time	(s)
V	Volume	($\mathrm{m^3}$)
v	Velocity	($\mathrm{m\,s^{-1}}$)
x	Molar share	(-)

Constants, Coefficients, Dimensionless Quantities

λ	Stoichiometric excess factor	(-)
D	Diffusion coefficient	($m^2\,s^{-1}$)
F	Faraday constant	($C\,mol^{-1}$)
n	Polytropic index	(-)
P	Permeability	($mol\,s^{-1}\,m^{-1}\,Pa^{-1}$)
R	Ideal gas constant	($J\,mol^{-1}\,K^{-1}$)
S	Henry coefficient	($mol\,m^{-3}\,Pa^{-1}$)
z	Number of electrons transferred	(-)

Fundamentals

E_η	Activation overpotential	(V)
E_0	Thermodynamic equilibrium potential	(V)
E_{cell}	Cell potential	(V)
$E_{MassTransport}$	Mass transport overpotential	(V)
E_N	Nernst potential	(V)
E_{ohm}	Ohmic overpotential	(V)
h	Specific enthalpy	($J\,mol^{-1}$)
I	Current	(A)
s	Specific entropy	($J\,mol^{-1}\,K^{-1}$)
W	Work	(J)
w	Specific work	($J\,mol^{-1}$)

Chapter 3:

$\dot{Q}_{Heat}$	Heating power	($J\,s^{-1}$)
η	Efficiency	(-)
j	Current density	($A\,m^{-2}$)
P_{el}	Electrical power	($J\,s^{-1}$)

Chapter 4:

q_{Pt}	Specific oxidation charge	($C\,cm^{-2}$)

Chapter 5:

ϵ	Porosity	(-)
ψ	Water content	(-)
σ	Proton conductivity	($S\,m^{-1}$)
τ	Tortuosity	(-)
ζ	Electroosmotic drag coefficient	(-)
d	Diameter	(m)
H	Height of cell	(m)
r	Radius	(m)
R_{CL}	Transport resistance of the catalyst layer	($s\,m^{-1}$)
RH	Relative humidity	(-)

List of Abbreviations

CV cyclic voltammetry

ECSA electrochemically active surface area

EHC electrochemical hydrogen compressor

EIS electrochemical impedance spectroscopy

GHG green house gas

HER hydrogen evolution reaction

HOR hydrogen oxidation reaction

HRF hydrogen recovery factor

MEA membrane electrode assembly

PBI polybenzimidazole

PEM proton exchange membrane

PFSA perfluor sulfonic acid

PSA pressure swing adsorption

PTFE polytetrafluoroethylene

DOI: 10.18154/RWTH-2025-10510

Aachener
Verfahrenstechnik

RWTH AACHEN
UNIVERSITY